

การระบุโครงสร้างของความบกพร่องจากสเปกตรัมการดูดกลืนแสงย่านใต้แดง
และรังสีเอกซ์: การคำนวณแบบเฟสตัดพรินซิเพิล

นายจิรโรจน์ ต.เทียนประเสริฐ

วิทยานิพนธ์นี้เป็นส่วนหนึ่งของการศึกษาตามหลักสูตรปริญญาวิทยาศาสตรดุษฎีบัณฑิต
สาขาวิชาฟิสิกส์
มหาวิทยาลัยเทคโนโลยีสุรนารี
ปีการศึกษา 2551

**IDENTIFICATION OF DEFECT STRUCTURES
THROUGH INFRARED AND X-RAY ABSORPTION
SPECTROSCOPIES: FIRST PRINCIPLES
CALCULATIONS**

Jiraroj T-Thienprasert

**A Thesis Submitted in Partial Fulfillment of the Requirements for the
Degree of Doctor of Philosophy in Physics
Suranaree University of Technology
Academic Year 2008**

**IDENTIFICATION OF DEFECT STRUCTURES THROUGH
INFRARED AND X-RAY ABSORPTION SPECTROSCOPIES:
FIRST PRINCIPLES CALCULATIONS**

Suranaree University of Technology has approved this thesis submitted in partial fulfillment of the requirements for the Degree of Doctor of Philosophy.

Thesis Examining Committee

(Asst. Prof. Dr. Chinorat Kobdaj)

Chairperson

(Prof. Dr. Sukit Limpijumnong)

Member (Thesis Advisor)

(Prof. Dr. Kritsana Sagarik)

Member

(Assoc. Prof. Dr. Jiti Nukeaw)

Member

(Dr. Saroj Rujirawat)

Member

(Prof. Dr. Pairote Sattayatham)

Vice Rector of Academic Affair

(Assoc. Prof. Dr. Prapun Manyum)

Dean of Institute of Science

จิรโรจน์ ต.เทียนประเสริฐ : การระบุโครงสร้างของความบกพร่องจากสเปกตรัมการ
ดูดกลืนแสงย่านใต้แดงและรังสีเอกซ์: การคำนวณแบบเฟิสต์พริ้นซิเพิล
(IDENTIFICATION OF DEFECT STRUCTURES THROUGH INFRARED AND
X-RAY ABSORPTION SPECTROSCOPIES: FIRST PRINCIPLES
CALCULATIONS) อาจารย์ที่ปรึกษา : ศาสตราจารย์ ดร.ชูกิจ ลิมปิจำนงค์, 164 หน้า.

ในวิทยานิพนธ์นี้ได้ใช้การคำนวณแบบเฟิสต์พริ้นซิเพิล คำนวณอัตรลักษณ์ของความ
บกพร่องหรือสารเจือและเปรียบเทียบกับผลการทดลองที่มี ในวิทยานิพนธ์นี้มุ่งเน้นการ
คำนวณหาอัตรลักษณ์ของสารเจืออยู่สองสิ่ง ที่มีความสัมพันธ์กับโครงสร้างโดยรอบของสารเจือเป็น
อย่างมาก นั่นคือ ความถี่การสั่นและการดูดกลืนรังสีเอกซ์ ซึ่งผลการศึกษาที่สำคัญสามารถสรุปได้
ดังต่อไปนี้ (1) จากผลการคำนวณความถี่การสั่นของสารเจือ ออกซิเจนและไฮโดรเจนในรูปแบบ
ต่าง ๆ ในผลึกแคลเซียมแมกนีเซียมไดออกไซด์ แสดงให้เห็นว่ากลุ่มนักทดลองได้อธิบายผลการทดลองผิดพลาด
จากผลการศึกษาในวิทยานิพนธ์ฉบับนี้ จึงได้มีการเขียนบทความเพื่อท้วงติง (2) จากการ
เปรียบเทียบผลการคำนวณกับผลการทดลองการดูดกลืนรังสีเอกซ์ ทำให้สามารถระบุสัดส่วน
โครงสร้างโดยรอบของอินเดียม นั่นคือ แบบ 4 ทบ และ 6 ทบ ในสารตัวอย่างอินเดียมออกซิไดรด์
ที่มีอัตราส่วนของออกซิเจนและไนโตรเจนแตกต่างกัน (3) สเปกตรัมการดูดกลืนรังสีเอกซ์
ของคลอรีนและแคลเซียม ได้ถูกนำมาใช้เพื่อตรวจสอบความถูกต้องของโครงสร้างการเคลื่อนที่
ของไอออนในน้ำที่จำลองได้จากการคำนวณแบบผสมระหว่างควอนตัมและโมเลกุล ซึ่งในที่นี้ได้มี
การพัฒนาวิธีการคำนวณค่าเฉลี่ยของสเปกตรัมการดูดกลืนที่คำนวณได้ โดยมีการวิเคราะห์เชิง
เปรียบเทียบระหว่างผลการคำนวณกับผลการทดลอง

JIRAROJ T-THIENPRASERT : IDENTIFICATION OF DEFECT
STRUCTURES THROUGH INFRARED AND X-RAY ABSORPTION
SPECTROSCOPIES: FIRST PRINCIPLES CALCULATIONS.
THESIS ADVISOR : PROF. SUKIT LIMPIJUMNONG, Ph.D. 164 PP.

FIRST PRINCIPLES/ INFRARED SPECTROSCOPY/ LOCAL VIBRATIONAL
MODE/ X-RAY ABSORPTION

In this thesis, signatures of many defects in different materials have been calculated using first-principles approaches. They are compared with available experimental results. The main focus is on two types of signatures that are strongly related to the local structures of defects; the vibrational frequencies and the x-ray absorption spectra. Important results can be briefly summarized as following. (1) The calculated vibrational frequencies of various O and H defects in CdTe indicate that experimental group has made a wrong interpretation in their manuscript. Based on this work, the comment is published. (2) The amounts of four-fold and six-fold indium atoms in each indium oxynitride alloy sample with varied O:N ratio, in each sample have been determined by directly comparing the simulations with the measurements. (3) The x-ray absorption spectra of ions (Cl^- and Ca^{2+}) in water have been used to determine the validity of the dynamical simulation based on QM/MM calculations. The regime to extract the average absorption spectra based on the dynamical simulation has been developed. The resulting spectra in comparison with experimental results are discussed.

School of Physics

Student's Signature _____

Academic Year 2008

Advisor's Signature _____

ACKNOWLEDGEMENTS

This research could not be completed without the support of many persons. I would like to express appreciation to my advisor Prof. Dr. Sukit Limpijumnong for selecting me for the Royal Golden Jubilee Ph.D. scholarship, his kind support, and guiding the way to be a researcher. I would like to thank Prof. Dr. Kritsana Sagarik, Assoc. Prof. Dr. Jiti Nukeaw, Asst. Prof. Dr. Chinorat Kobdaj, and Dr. Saroj Rujirawat for serving as the thesis-examining committees. I would like to thank Assoc. Prof. Dr. Anan Tongraar for his kind collaboration. I would like to thank the Thailand Research Fund (TRF) for financial support through the Royal Golden Jubilee Ph.D. program (PHD/0107/2548). I would like to acknowledge Kasetsart University, Synchrotron Light Research Institute, and NANOTEC for funding and resources. This work would not be completed without the contributions and helpful discussions from the faculties at the School of Physics, Suranaree University of Technology and the members of the condensed matters physics group – Sirichok Jungthawan, Pakpoom Reunchan, Kanoknan Sarasamak, and Sutassana Naphattalung. I would like to thank Miss. Varalak Saengsuwan for her help. Most of all, I would like to thank my parents for their encouragement and their kind financial support.

Jiraroj T-Thienprasert

CONTENTS

	Page
ABSTRACT IN THAI.....	IV
ABSTRACT IN ENGLISH.....	V
ACKNOWLEDGEMENTS.....	VI
CONTENTS.....	VII
LIST OF TABLES.....	XI
LIST OF FIGURES.....	XII
LIST OF ABBREVIATIONS.....	XIX
CHAPTER	
I INTRODUCTION.....	1
1.1 Overview of the Calculation Approaches.....	1
1.2 Research Objectives.....	4
1.3 Scope and Limitation of the Study.....	5
1.4 References.....	6
II THEORETICAL APPROACHES.....	8
2.1 Density Functional Theory.....	8
2.2 Earlier Approaches.....	9
2.3 The Kohn-Sham Equations.....	10
2.4 The Exchange Correlation Term: LDA and GGA.....	13
2.5 Bloch's Theorem and Plane Wave Basis Sets.....	14
2.6 Special k-point in the Brillouin Zone.....	16

CONTENTS (Continued)

	Page
2.7 Pseudo Potential.....	16
2.8 The Hellmann-Feynman Theorem.....	19
2.9 Electronic Ground State Calculations.....	19
2.10 Vibrational Modes Calculations.....	22
2.11 References.....	28
III BASIC THEORY OF X-RAY ABSORPTION SPECTROSCOPY.....	32
References.....	39
IV OXYGEN AND HYDROGEN DEFECTS IN CADMIUM	
TELLURIDE.....	42
4.1 Introduction.....	42
4.2 Structural Relaxation.....	44
4.3 Calculation of Defect Formation Energy.....	45
4.4 Local Vibrational Modes (LVM) calculations.....	47
4.5 Results and Discussion.....	49
4.5.1 Native defects in CdTe.....	49
4.5.2 Oxygen defects in CdTe.....	52
4.5.3 Hydrogen and oxygen defects in CdTe.....	59
4.6 Conclusion.....	62
4.7 References.....	62
V LOCAL STRUCTURE OF INDIUM OXYNITRIDE.....	65
5.1 Introduction.....	65
5.2 Experimental Method.....	66

CONTENTS (Continued)

	Page
5.3 Computational Details.....	68
5.4 Results and Discussion.....	70
5.4.1 Electronic structures of InN, In ₂ O ₃ , and InN _{1-x} O _x alloy.....	70
5.4.2 XANES spectra of InN, In ₂ O ₃ , and InN _{1-x} O _x alloy.....	76
5.5 Conclusion.....	80
5.6 References.....	81
VI HYDRATIONS STRUCTURES OF Ca²⁺ and Cl⁻ IONS BY X-RAY	
 ABSORPTION SPECTROSCOPY.....	85
6.1 Introduction.....	85
6.2 Experimental Details.....	89
6.3 Computational Details.....	90
6.3.1 QM/MM MD simulations.....	90
6.3.2 XAS data analysis.....	93
6.4 Results and Discussion.....	95
6.4.1 QM/MM MD results.....	95
6.4.2 EXAFS and QM/MM-EXAFS spectra.....	101
6.4.3 XANES and QM/MM-XANES spectra.....	108
6.5 Conclusion.....	113
6.6 References.....	114
VII CONCLUSION AND FUTURE WORK.....	123

CONTENTS (Continued)

	Page
APPENDICES	
APPENDIX A CODES FOR PREPARATION OF INPUT FILES AND EXTRACTING FORCES FOR DYNAMIC MATRIX CALCULATIONS	126
APPENDIX B UTILITY SCRIPTS FOR VASP AND FEFF CODES.....	137
APPENDIX C FEFF CODES.....	146
C.1 Parameters in FEFF Codes.....	146
C.2 Calculations of XANES and EXAFS Spectra.....	148
APPENDIX D PUBLICATIONS AND PRESENTATIONS	153
CURRICULUM VITAE.....	164

LIST OF TABLES

Table	Page
4.1 Formation energies in CdTe with Fermi level at the valence band maximum (VBM).....	57
4.2 The calculated and experimental frequencies of the oxygen and hydrogen defects in CdTe.....	58
5.1 The growth conditions and N:O ratios of each sample and the optical bandgap of the samples grown under the equivalent conditions (Sungthong <i>et al.</i> , 2008).....	70
6.1 Ion-oxygen distances, Debye-Waller factors, and coordination numbers, as obtained from fitting of the first peak of Ca ²⁺ -O and Cl-O RDFs.....	103
6.2 Ion-oxygen distances, Debye-Waller factors, and coordination numbers, as obtained from the analysis of the measured EXAFS spectra.....	105
A.1 The Fortran codes used for moving each atom from its equilibrium position.....	127
A.2 The Fortran codes used for constructing the dynamic matrix.....	129
A.3 The Fortran codes used for solving the dynamic matrix.....	132
B.1 The Python script used for constructing a supercell.....	137
B.2 The Python script and Fortran program used for constructing a cluster.....	139
C.1 An example input file for the <i>atoms code</i> used to generate the input file for the FEFF codes.....	147
C.2 An example of the input file for Cl <i>K</i> -edge XANES simulation.....	151
C.3 An example of the input file for Cl <i>K</i> -edge EXAFS calculation.....	152

LIST OF FIGURES

Figure	Page
2.1 A schematic representation of the pseudo potential and pseudo wave function plotted with respect to the distance, r , from the ionic nucleus. The dashed lines represent the corresponding pseudo wave function and pseudo potential inside the core radius.....	18
2.2 The self consistency scheme used in the VASP codes.....	21
2.3 Examples of the force constants describing the relationship between the axis of displacement and the axis of resulting force.....	24
2.4 An example of the potential energy-displacement curve fitted with the fourth-degree polynomial. The dots are the results from the calculations. The curve is the polynomial fit. This plot is the actual calculation of the frequency of O ₂ molecule substituting on the Te site in CdTe.....	27
3.1 The absorption K -edge of Cl ⁻ in water. The XANES and EXAFS regions are shown with the mark.....	33
3.2 The x-ray is absorbed and the core level electron is promoted out of the atom.....	34
3.3 The muffin-tin potential is set to zero in the interstitial region. The figure is a reproduction of Figure 9 in Ref. (Rehr and Albers, 2000).....	36
3.4 Examples of scattering paths. Red circle represents absorbing atom.....	37

LIST OF FIGURES (Continued)

Figure	Page
4.1 The infrared absorption spectrum of the oxygen doped CdTe. The inset shows the $O_{Te}-V_{Cd}$ defect model that Chen <i>et al.</i> claims to be responsible for the two observed LVMS. The figure is a reproduction of Figure. 1 in Ref. (Chen <i>et al.</i> , 2006).	43
4.2 Temperature dependence of ν_1 and ν_2 for the oxygen doped CdTe from 2 to 330 K (solid circles) and the weighted average of ν_1 and ν_2 , i.e., $\nu_0^* = (\nu_1 + 2\nu_2)/3$, calculated for each temperature (open circles). The figure is a reproduction of Figure 3 in Ref. (Chen <i>et al.</i> , 2006).	44
4.3 Total energy of zincblend CdTe as a function of the lattice constant. The solid circles and the line are the calculated and fit data, respectively.	45
4.4 Formation energies of native defects as a function of the Fermi level, under the Cd-rich (left panel) and Te-rich (right-panel) growth conditions. The slope of each line indicates the charge state.	50
4.5 The local structure of (a) Bulk, (b) Cd_{Te}^0 and (c) Te_{Cd}^{2+} in CdTe. The red and blue colors are used to label Cd and Te atoms, respectively. All bond distances are given as percentage differences from the bulk CdTe bond distance ($d = 2.783\text{\AA}$).	52

LIST OF FIGURES (Continued)

Figure	Page
4.6 Formation energies as a function of the Fermi level, under the Cd-rich (left panel) and Te-rich (right-panel) growth conditions. The dash lines with matching colors correspond to the sum of the individual defects. For example, the dashed blue line shows the sum of the energies of isolated O_{Te} and isolated V_{Cd} while the solid blue line shows the energy of $O_{Te}-V_{Cd}$ complex.	55
4.7 The local structure of (a) O_{Te}^0 , (b) $[O_{Te}-V_{Cd}]^{2+}$, (c) $[O_2]_{Te}^0$, (d) H^+ , (e) H^- , (f) $O_{Te}-H^+$ (BC), (g) $O_{Te}-H^-$ (AB), and $Te_{Cd}-H^+$ (BC). The red, blue, green, and light-blue colors are used to label Cd, Te, O, and H atoms, respectively. All bond distances are given as percentage differences from the bulk CdTe bond distance ($d = 2.783\text{\AA}$).	56
4.8 The local structure of complexes defects $2H-Te_{Cd}$ when H atoms are at BC and AB sites.	60
4.9 Defect formation energies of $2H-Te_{Cd}$ plotted as a function of the Fermi level, under the Cd-rich (left panel) and Te-rich (right-panel) growth conditions, respectively. The dash lines correspond to the sum of the individual defects (i.e., $Te_{Cd} + H$ and $Te_{Cd} + H + H$).	61

LIST OF FIGURES (Continued)

Figure	Page
5.1 The local structure around In atoms used in the simulations of the In L_3 -edge XANES of (a) In_2O_3 , (b) InN, (c) replacing four nitrogen nearest neighbor (NN) of In with four oxygen in wurtzite-InN, and (d) replacing one nitrogen NN of In with oxygen and one oxygen NN of In with nitrogen for InN and In_2O_3 , respectively. All bond distances are given as a percentage difference from an average In_2O_3 bond distance ($d_{\text{calc}} = 2.170$ Å).	71
5.2 (a) Band structures of 72-atom supercell InN. The energy is referenced to the top of the valence band. (b) The calculated total density of state of InN and projected PDOS (s , p , and d states) of In and N atoms.	72
5.3 (a) Band structures of 72-atom supercell $\text{InN}_{0.6}\text{O}_{0.4}$ alloy. The energy is referenced to the top of the valence band. (b) The calculated total density of state of $\text{InN}_{0.6}\text{O}_{0.4}$ alloy and projected PDOS (s , p , and d) of In, N, and O atoms.	73
5.4 (a) Band structures of 40-atom unit cell In_2O_3 . The energy is referenced to the top of the valence band. (b) The calculated total density of state of In_2O_3 and projected PDOS (s , p , and d) of In and O atoms.	74
5.5 The site-projected PDOS ($s+d$) of In in InN and $\text{InN}_{0.6}\text{O}_{0.4}$ alloy in wurtzite structure. The broken lines show the PDOS as calculated. The full lines show the smeared CB ($s+d$) states. All lines are color coded (red: InN; blue: $\text{InN}_{0.6}\text{O}_{0.4}$).	75

LIST OF FIGURES (Continued)

Figure	Page
5.6 (a) Normalized In <i>L3</i> -edge XANES spectra of indium oxynitride samples prepared under different gas-timing with increased O ₂ timing from bottom curve to top curve. Circles show recorded data points and the curves are the (noise removed) fit to the data. Inset: The plots from the main panel without offset at the energy range near the s ₁ shoulders to highlight the changes in the shoulder height. (b) The calculated In <i>L3</i> -edge XANES spectra of wurtzite InN, bixbyite In ₂ O ₃ , wurtzite InN _{0.6} O _{0.4} , and the simulated separated phase alloys with 38% and 49% four-fold In atoms (see text for detail).	77
5.7 (a) The calculated spectra of pure InN and replacing 1 nitrogen NN and 4 nitrogen NN of In with oxygen (as shown in Figure 6.1), and (b) The calculated spectra of In _{avg} , In1, In2, and replacing one oxygen NN with nitrogen.	78
6.1 The x-ray absorption instrument at beamline 8 (BL-8) of Siam Photon Source (electron energy of 1.2 GeV, beam current 120-80 mA), Synchrotron Light Research Institute, Thailand.	89
6.2 Ca ²⁺ -O and Cl ⁻ -O RDFs and their corresponding integration numbers.	95
6.3 Distributions of the coordination numbers of Ca ²⁺ and Cl ⁻ , calculated within the first minimum of the Ca ²⁺ -O and Cl ⁻ -O RDFs.	97
6.4 Distributions of the coordination numbers of Ca ²⁺ and Cl ⁻ , calculated within the first minimum of the Ca ²⁺ -O and Cl ⁻ -O RDFs.	97

LIST OF FIGURES (Continued)

Figure	Page
6.5	Distribution of the Cl ⁻ ---H-O angle, calculated within the first minimum of the Cl ⁻ -O RDF. 99
6.6	Time dependences of (a) Ca ²⁺ ---O distance and (b) number of first-shell waters, as obtained from the 50 ps of the QM/MM MD simulation. In Figure 6.6a, the dash line parallel to the x-axis positions the first minimum of the Ca ²⁺ -O RDF. 100
6.7	Time dependences of (a) Cl ⁻ ---O distance and (b) number of first-shell waters, selecting only for the first 12 ps of the QM/MM MD simulation. In Figure 6.7a, the dash line parallel to the x-axis positions the first minimum of the Cl ⁻ -O RDF. 100
6.8	Comparison between the first Ca ²⁺ -O and Cl ⁻ -O RDFs and their fits with respect to Gaussian function. 103
6.9	Structural factors for Ca ²⁺ in water, comparing between the results obtained from the QM/MM MD simulation and the corresponding experimental measurements. 104
6.10	Structural factors for Cl ⁻ in water, comparing between the results obtained from the QM/MM MD simulation and the corresponding experimental measurements. 105
6.11	Fourier transformations of the structural factors for Ca ²⁺ in water, comparing between the results obtained from the QM/MM MD simulation and the corresponding experimental measurements. 106

LIST OF FIGURES (Continued)

Figure	Page
6.12 Fourier transformations of the structural factors for Cl ⁻ in water, comparing between the results obtained from the QM/MM MD simulation and the corresponding experimental measurements.....	107
6.13 Simulated XANES spectra for Ca ²⁺ in water, as obtained from each of QM/MM MD snapshots.....	109
6.14 Comparison between the experimental Ca <i>K</i> -edge XANES spectrum and the spectra obtained from the QM/MM MD simulation. The simulation results are displayed in terms of an average XANES spectrum, together with the standard deviations taken from the overall QM/MM MD snapshots.....	111
6.15 Simulated XANES spectra for Cl ⁻ in water, as obtained from each of QM/MM MD snapshots.....	112
6.16 Comparison between the experimental Cl <i>K</i> -edge XANES spectrum and the spectra obtained from the QM/MM MD simulation. The simulation results are displayed in terms of an average XANES spectrum, together with the standard deviations taken from the overall QM/MM MD snapshots.....	113
C.1 The calculated XANES spectra of Cl ⁻ in aqueous solution with different SCF (top) and FMS (bottom) radius.....	150

LIST OF ABBREVIATIONS

BZ	=	Brillouin Zone
CBM	=	Conduction Band Minimum
DFT	=	Density Functional Theory
EXAFS	=	Extended X-ray Absorption Fine Structure
FMS	=	Full-Multiple Scattering
GGA	=	Generalized Gradient Approximation
IR	=	Infrared
KS	=	Kohn-Sham
LDA	=	Local Density Approximation
LVM	=	Local Vibrational Mode
MS	=	Multiple Scattering
NN	=	Nearest Neighbor
RF	=	Radio Frequency
SCF	=	Self-Consistent Field
USPP	=	Ultra Soft Pseudo Potential
VASP	=	Vienna Ab-initio Simulation Package
VBM	=	Valence Band Maximum
XANES	=	X-ray Absorption Near Edge Structure
XAS	=	X-ray Absorption Spectroscopy
XC	=	Exchange-Correlation

CHAPTER I

INTRODUCTION

1.1 Overview of the Calculation Approaches

In principle, once the quantum mechanics theory is established, most of material physical properties, which are rooted from electron behavior, are explained by directly solving electron wave functions in each system. However, directly solving a full set of Schrödinger equations for even a simple many-electron system are proven to be too complicated. As a result, there are many approximation invented to reduce the complicated many-body problems down to a solvable ones (Martin, 2004). Density functional theory (DFT) is a key theory to reduce many-electron problems to a single particle problem. This has been done by simplifying the complicated electron-electron interactions in the many-body problems into the interactions between each electron and the electron density of the system. This involves the introduction of the exchange and correlation function (XC). The simplified Schrödinger equation, which is now a set of single particle equations, is called Kohn-Sham (KS) equations (Hohenberg and Kohn, 1964; Kohn and Sham, 1965). There are several details regarding the form of XC function and the ways to solve the KS equations (Ceperley and Alder, 1980; Perdew and Zunger, 1981). For instant, the two widely used XC functions are based on the local density approximations (LDA) and on the generalized gradient approximations (GGA). Each type of XC function has its own advantages. Regarding the approaches to solve the equations, approximations

can be further applied to reduce the computation demand. For example, if the pseudo potentials is used instead of the actual atomic potential, the resulting electron wave functions can be greatly smoothed (making it much easier to be expanded in a much reduced plane wave basis set) without losing too much accuracy in physical bonding properties. Although there are many details on the approximations that can be chosen for each calculation, the approaches of solving KS equations based on quantum mechanics to obtain the approximate solutions of material under study are often referred to as first principles (or *ab initio*) approach and are believed to be highly reliable.

To solve for the electron wave functions of the systems under study, the Vienna *Ab-initio* Simulation Package (VASP) codes (Kresse and Hafner, 1994; Kresse and Furthmuller, 1996), which are based on the DFT, were used. The potentials of atoms are replaced by ultrasoft-pseudo potentials (Vanderbilt, 1990) so that the electron wave function can be expanded in a planewave basis set with very low cutoff energy (typically around 300 eV) compared to those required by traditional pseudo potentials (typically around 1000 eV). In the VASP codes, there are different types of XC functions that they can be chosen to suit the nature of the system under study. Once the solutions, i.e. electron wave functions, of the system under studied are obtained, several physical properties can be directly obtained from the program. These include the total ground state energy, the electron wave functions, the electron densities, band structures, and electron density of states. With slightly more efforts, other physical properties can also be studied using the first principles calculations at several deformed crystal structures. For the simplest example, with repetitive calculations of a crystal with varied volume, the energy-vs-volume plot can be used to calculate the

bulk modulus of the crystal that can be directly compared with experiments. In this thesis, this widely accepted first principles approach was used to study some defect structures and local structures by simulating their infrared (IR) and/or x-ray absorption properties. Although both infrared and x-ray are considered as electromagnetic waves, the underlying physics for their absorption by condensed matters are very different. Nevertheless, both of the absorption types can be studied first-principally.

First, for the IR absorption, the main driven mechanism that leads to the absorption of the infrared light is the vibration of the atoms in a crystal. This is because the vibration frequencies of atoms in crystals are in the region of the frequency of IR light. Each crystal has their natural vibration modes that lead to the greater absorption of the IR light at their resonance frequencies, showing up as peaks in the IR absorption spectrum. To identify a certain defect structure in a crystal, one can calculate the local vibrational mode (LVM) of the defect and look for such absorption peaks in an actual experiment. The LVM of a defect are directly calculated by determining a full dynamic matrix of a supercell containing the defect. The so-called frozen-phonon approach (Teweldeberhan and Fahy, 2005) was used. Each atom in the supercell is displaced one-at-a-time and the force responses on other atoms are used to construct the force response matrix. The force response matrix leads to the dynamic matrix and eventually diagonalized to get the LVM. A brief description on how the LVM are determined by full dynamic matrix will be described in a next chapter. For certain defects that have distinct LVM from the lattice phonon, their LVM can be rather accurately approximated by calculating a reduced dynamic matrix

containing only the defect atom (and sometimes also one or a few nearest neighbors) (Limpijumnong *et al.*, 2005).

Second, for the x-ray absorption, the main mechanism that leads to the absorption features in the spectrum is the excitation of core electrons to the empty levels above Fermi energy. The x-ray absorption spectroscopy (XAS) technique turns out to be a very powerful technique. Part of the reasons is because it is very selective due to the fact that the core level of each element is different, making it possible to selectively probe each element (and not any other) by using just certain x-ray energy (Koningsberger and Prins, 1988). The core electrons are excited by x-ray to the empty levels above the Fermi level. The partial density of those electronic states (that the transition from the core level is allowed) depends strongly on the neighboring arrangements surrounding that absorbing atom. XAS measurements combining with first principles modeling of the XAS spectrum, especially the near edge region (X-ray absorption near-edge spectroscopy; XANES), are shown to be a very powerful way to identify defects in crystals (Limpijumnong *et al.*, 2006). In addition, through our collaborations with quantum chemistry (QM-MM simulation by Tongraar) and experimentalists (XANES measurement by Rujirawat and Onkaw), we can study complicated disordered systems such as arrangements of water molecules around ions.

1.2 Research Objectives

Based on first-principles calculations, two types of signatures of several important defects structures that can lead to their identifications in actual experiments were simulated. Depending on defect, either the IR absorption or the x-ray absorption spectrum was studied. The IR absorption signatures of the defects were calculated

from the LVM whereas the x-ray absorption signatures were calculated from either (1) the partial density of states (PDOS) that found to describe very well the near edge region; or (2) the *ab initio* multiple scattering approach as implemented in the FEFF codes (Ankudinov *et al.*, 1998)

1.3 Scope and Limitation of the Study

Using first-principles supercell approach (Kresse and Furthmuller, 1996), the electronic solutions of impurities or defects in many crystal systems (for e.g., III-V and II-VI semiconductors and ceramic oxides) as well as disordered system (e.g. ion in water) were calculated. The VASP codes (Kresse and Hafner, 1994) are the main tool for first principally determination of electronic wave functions and the local atomic structures. Based on the VASP codes, the LVM and the PDOS that can be used to compare with IR experiments and XANES, respectively, are calculated. In addition, for certain systems, VASP codes are used to determine accurate local geometry for further XAS calculations by FEFF codes.

The defects that are suitable for LVM calculations are the defects that have distinct LVM from the crystal phonon. This is necessary because in actual experiment the defect signatures would not be over shadowed by the crystal phonon absorptions.

The impurity type defects are suitable for identification using XAS. This is because one can directly probe the absorption of the impurity element which occurs at different x-ray photon energy comparing to host elements. Generally native defects such as self interstitials or vacancies are not suitable for identification using XAS.

Systems included in this thesis:

- Oxygen defects in CdTe (IR absorption)

- Dopants in wide band gap semiconductors (IR absorption and XAS)
- Ions (for e.g., K^+ , Cl^- , Ca^{2+}) in aqueous solution (XAS)

1.4 References

- Ankudinov, A. L., Ravel, B., Rehr, J. J., and Conradson, S. D. (1998). Real-space multiple-scattering calculation and interpretation of x-ray-absorption near-edge structure. **Phys. Rev. B** 58: 7565.
- Ceperley, D. M. and Alder, B. J. (1980). Ground state of the electron gas by a stochastic method. **Phys. Rev. Lett.** 45: 566.
- Hohenberg, P. and Kohn, W. (1964). Inhomogeneous Electron Gas. **Phys. Rev.** 136: B864.
- Kohn, W. and Sham, L. J. (1965). Self-Consistent Equations Including Exchange and Correlation Effects. **Phys. Rev.** 140: A1133.
- Koningsberger, D. C. and Prins, R. (1988). **X-ray Absorption: Principles applications, techniques of EXAFS, SEXAFS, and XANES.** New York:Wiley.
- Kresse, G. and Furthmuller, J. (1996). Efficient iterative schemes for ab initio total-energy calculations using a plane-wave basis set. **Phys. Rev. B** 54: 11169.
- Kresse, G. and Hafner, J. (1994). Norm-conserving and ultrasoft pseudopotentials for first-row and transition-elements. **J. Phys.:Cond. Matt.** 6: 8245.
- Limpijumnong, S., Li, X., Wei, S.-H., and Zhang, S. B. (2005). Substitutional diatomic molecules NO, NC, CO, N_2 , and O_2 : Their vibrational frequencies and effects on p doping of ZnO. **Appl. Phys. Lett.** 86: 211910.

- Limpijumng, S., Smith, M. F., and Zhang, S. B. (2006). Characterization of As-doped, *p*-type ZnO by x-ray absorption near-edge structure spectroscopy: Theory. **Appl. Phys. Lett.** 89: 222113.
- Martin, R. M. (2004). **Electronic structure: basic theory and practical methods.** United Kingdom: Cambridge university press.
- Perdew, J. P. and Zunger, A. (1981). Self-interaction correction to density-functional approximations for many-electron systems. **Phys. Rev. B** 23: 5048.
- Teweldeberhan, A. M. and Fahy, S. (2005). Calculated pressure dependence of the localized vibrational mode of nitrogen in GaN_xAs_{1-x}. **Phys. Rev. B** 72: 195203.
- Vanderbilt, D. (1990). Soft self-consistent pseudopotentials in a generalized eigenvalue formalism. **Phys. Rev. B** 41: 7892.

CHAPTER II

THEORETICAL APPROACHES

2.1 Density Functional Theory

In quantum mechanics, various information of material system could be extracted from the electron wave functions. In principle, these wave functions can be obtained by directly solving the Schrödinger equation of the complete many-electron system. However, explicitly solving many-electron system is too complicated. In this chapter, a brief review of approximations that are used to simplify the many-electron problems will be given. Density functional theory (DFT) provides a crucial mean to reduce the Schrödinger equation of a many-electron system into a solvable problem. DFT assumes that the Hamiltonian can be written as a functional of the electron density instead of electron wave functions. While the complete many-electron wave functions have $3N$ variables (three spatial variables for each of the N electron) the density is only a function of three variables. DFT can be viewed as a ground state theory with the electron charge density serving as the variational parameter. The N -electron problem could be treated as N one-electron equations where the many-electron interactions between an electron with other electrons beyond simple coulombic interactions are corrected through the effective exchange-correlation (XC) potential term. This leads to the set of Kohn-Sham (KS) one-electron equations. There are various techniques to further reduce the computational demand in solving the KS

equations. The plane wave basis sets with pseudo potentials techniques are one of the popular techniques used to solve KS equations.

2.2 Earlier Approaches

Many material properties can be obtained from the wave function of electrons. In principles, the wave functions can be solved from the N-electron Schrödinger equation $\Psi(\mathbf{r}_1, \mathbf{r}_2, \mathbf{r}_3, \dots, \mathbf{r}_N)$:

$$H\Psi = E\Psi, \quad (2.1)$$

where E is the electronic energy, $\Psi = \Psi(\mathbf{r}_1, \mathbf{r}_2, \mathbf{r}_3, \dots, \mathbf{r}_N)$ is the wave function, and H is the Hamiltonian operator,

$$H = \sum_{i=1}^N \left(-\frac{\hbar^2}{2m} \nabla_i^2 - Z e^2 \sum_R \frac{1}{|\mathbf{r}_i - \mathbf{R}|} \right) + \frac{1}{2} \sum_{i \neq j} \frac{e^2}{|\mathbf{r}_i - \mathbf{r}_j|}. \quad (2.2)$$

The first term in Eq. (2.2) is the kinetic energy operator of the N-electron system, the second term represents the interaction of electrons with nuclei at positions \mathbf{R} , and the third term is the coulomb energy which is caused by the interaction of electrons with each other. In the Hartree approximation, the wave function is assumed to be a product of N one-electron wave function:

$$\Psi(\mathbf{r}_1, \mathbf{r}_2, \mathbf{r}_3, \dots, \mathbf{r}_N) = \psi_1(\mathbf{r}_1) \psi_2(\mathbf{r}_2) \dots \psi_N(\mathbf{r}_N). \quad (2.3)$$

From Eq. (2.3), it implies that the one-electron wave function is a solution to the one-electron Schrödinger equation:

$$-\frac{\hbar^2}{2m} \nabla_i^2 \psi_i(\mathbf{r}) + V(\mathbf{r}) \psi_i(\mathbf{r}) = \varepsilon_i(\mathbf{r}), \quad (2.4)$$

in which

$$V(\mathbf{r}) = -Z e^2 \sum_R \frac{1}{|\mathbf{r} - \mathbf{R}|} - e \int d\mathbf{r}' n(\mathbf{r}') \frac{1}{|\mathbf{r} - \mathbf{r}'|},$$

where the first term of Eq. (2.4) is the one-electron kinetic energy. $V(\mathbf{r})$ is the potential of electron that includes the potential from ions and the potential induced by the electron charge density $n(\mathbf{r})$.

However, strictly speaking Hartree wave function is invalid because it does not satisfy the Pauli exclusion principle which states that the wave function must be anti-symmetric with respect to electron interchanging. Replacing the Hartree wave function by an anti-symmetric Slater determinant of one-electron wave functions, we get the following equation for orthogonal one-electron functions ψ_i :

$$\begin{aligned} & -\frac{\hbar^2}{2m} \nabla_i^2 \psi_i(\mathbf{r}) + V_{ion}(\mathbf{r}) \psi_i(\mathbf{r}) + V_{elec}(\mathbf{r}) \psi_i(\mathbf{r}) - \\ & \sum_j \int \frac{d\mathbf{r}'}{|\mathbf{r} - \mathbf{r}'|} \psi_j^*(\mathbf{r}') \psi_i(\mathbf{r}') \psi_j(\mathbf{r}) \psi_i^*(\mathbf{r}) = \varepsilon_i(\mathbf{r}). \end{aligned} \quad (2.5)$$

Eq. (2.5) is called Hartree-Fock equation. The last term on the left side is the exchange term. This non-linear integral operator, though only first order approximation, is very complicated to calculate. Next, the electron-electron exchange-correlations function within the framework of DFT will be discussed.

2.3 The Kohn-Sham Equations

In their work, Hohenberg and Kohn have shown two theorems that lay the ground for density functional theory (Hohenberg and Kohn, 1964):

- I) The total energy of a many-electron system in an external potential is a unique functional of electron density $n(\mathbf{r})$.
- II) From the trial density $n(\mathbf{r})$, we get that $n(\mathbf{r}) \geq 0$ and $\int n(\mathbf{r}) d\mathbf{r} = N$,

$$E_0 \leq E_v[n], \quad (2.6)$$

where E_0 is the ground state energy and the energy functional $E_v[n]$ is defined by

$$E_v[n] = T[n] + V_{ee}[n] + \int n(\mathbf{r}) V_{ion}(\mathbf{r}) d\mathbf{r}. \quad (2.7)$$

From Eq. (2.7), one can minimize the functional $E_v[n]$ with respect to the electron density. This will give the ground state electronic energy and corresponding electron density of the system. Kohn and Sham (Kohn and Sham, 1965) showed that the total energy functional $E[n(\mathbf{r})]$ can be written as

$$E[n(\mathbf{r})] = \int V_{ion}(\mathbf{r}) n(\mathbf{r}) d\mathbf{r} + \frac{1}{2} \iint \frac{n(\mathbf{r}) n(\mathbf{r}')}{|\mathbf{r} - \mathbf{r}'|} d\mathbf{r} d\mathbf{r}' + G[n(\mathbf{r})]. \quad (2.8)$$

The first term in Eq. (2.8) is the classical Coulomb interactions between the electrons and ions, the second term represents the coulomb interaction of electrons with other electrons, both of which are function of the electron charge density $n(\mathbf{r})$, and the last term $G[n(\mathbf{r})]$ includes the kinetic energy of non-interacting electrons and the effects of exchange-correlation which can be written as

$$G[n(\mathbf{r})] = T[n(\mathbf{r})] + E_{xc}[n(\mathbf{r})], \quad (2.9)$$

where $T[n(\mathbf{r})]$ is the kinetic energy and $E_{xc}[n(\mathbf{r})]$ is the exchange and correlation energy for many-electron system of interacting particles, both of which are also functions of electron charge density $n(\mathbf{r})$.

According to the Hohenberg-Kohn theorem, the total energy function given by Eq. (2.8) is stationary with respect to the variations in the ground state charge density, that is

$$\int \delta n(\mathbf{r}) \left\{ \frac{\delta T[n(\mathbf{r})]}{\delta n(\mathbf{r})} + V_{ion}(\mathbf{r}) + \int \frac{n(\mathbf{r}')}{|\mathbf{r} - \mathbf{r}'|} d\mathbf{r}' + \mu_{xc}(\mathbf{r}) \right\} = 0, \quad (2.10)$$

in which

$$\mu_{XC} = \frac{\delta E_{XC}[n(\mathbf{r})]}{\delta n(\mathbf{r})}. \quad (2.11)$$

The requirement, that the variation in charge density leaves the number of atoms fixed or unchanged, gives

$$\int \delta n(\mathbf{r}) d\mathbf{r} = 0. \quad (2.12)$$

Applying the condition (2.12) to Eq. (2.10), we get

$$\frac{\delta E(\mathbf{r})}{\delta n(\mathbf{r})} = \frac{\delta T[n(\mathbf{r})]}{\delta n(\mathbf{r})} + V_{ion}(\mathbf{r}) + \int \frac{n(\mathbf{r}')}{|\mathbf{r} - \mathbf{r}'|} d\mathbf{r}' + \mu_{XC}(\mathbf{r}) = \nu, \quad (2.13)$$

where ν is the Lagrange multiplier that is associated with the constraint of constant particle number. We can rewrite the equation using an effective potential $V_{eff}(\mathbf{r})$ as

$$\frac{\delta E(\mathbf{r})}{\delta n(\mathbf{r})} = \frac{\delta T[n(\mathbf{r})]}{\delta n(\mathbf{r})} + V_{eff}(\mathbf{r}) = \nu. \quad (2.14)$$

Comparing Eq. (2.14) to Eq. (2.13), the effective potential is

$$V_{eff}(\mathbf{r}) = V_{ion}(\mathbf{r}) + \int \frac{n(\mathbf{r}')}{|\mathbf{r} - \mathbf{r}'|} d\mathbf{r}' + \mu_{XC}(\mathbf{r}). \quad (2.15)$$

The kinetic energy operator can be expressed as the sum of the kinetic energies of single particles

$$T = \sum_{i=1}^N \frac{\hbar^2}{2m} \int \psi_i^*(\mathbf{r}) (-\nabla^2) \psi_i(\mathbf{r}) d\mathbf{r}. \quad (2.16)$$

Finally, the solution of the ground state problem can be obtained by solving the Schrödinger equation for non-interacting particles in the effective potential $V_{eff}(\mathbf{r})$,

$$\left\{ -\frac{\hbar^2}{2m} \nabla^2 + V_{eff}(\mathbf{r}) \right\} \psi_i(\mathbf{r}) = \varepsilon_i \psi_i(\mathbf{r}). \quad (2.17)$$

From the Eq. (2.17), we can see that the complex problem for a system of interacting electrons is mapped onto a system of non-interacting electrons in effective potential that include the exchange-correlation part.

2.4 The Exchange Correlation Term: LDA and GGA

The local density approximation (LDA) as the exchange-correlation has been one of the most successful approximations which were introduced by Kohn and Sham in 1965 (Kohn and Sham, 1965). In the LDA, it is assumed that the density can be locally treated as a uniform gas. Then the exchange-correlation energy $\varepsilon_{XC}(\mathbf{r})$ per electron at any point \mathbf{r} is equal to the exchange-correlation energy per electron in a homogeneous electron gas with the same electron density as that at point \mathbf{r} . This can be written as

$$\varepsilon_{XC}[n(\mathbf{r})] = \varepsilon_{XC}^{\text{hom}}[n(\mathbf{r})], \quad (2.18)$$

and

$$E_{XC}[n(\mathbf{r})] = \int \varepsilon_{XC}[n(\mathbf{r})]n(\mathbf{r}) d\mathbf{r} = \int n(\mathbf{r})(\varepsilon_X[n(\mathbf{r})] + \varepsilon_C[n(\mathbf{r})]) d\mathbf{r}, \quad (2.19)$$

where $\varepsilon_X[n(\mathbf{r})]$ and $\varepsilon_C[n(\mathbf{r})]$ are the exchange and correlation energies density of a homogeneous electron gas of density $n(\mathbf{r})$. Eq. (2.18) is based on an assumption that the exchange-correlation energy is purely local. Although, there are several parameterizations for $\varepsilon_{XC}^{\text{hom}}[n(\mathbf{r})]$, the widely used one is that of Perdew and Zunger (Perdew and Zunger, 1981). The exchange energy of the homogeneous electron gas with density $n(\mathbf{r})$ is derived by Dirac (Dirac, 1930):

$$\varepsilon_X[n(\mathbf{r})] = -\frac{3}{4} \left(\frac{3}{\pi} \right)^{1/3} \int n(\mathbf{r})^{4/3} d\mathbf{r}. \quad (2.20)$$

The correlation energy is based on quantum Monte Carlo calculations of Ceperley and Alder (Ceperley and Alder, 1980) on homogeneous electron gases at various densities. The LDA method is successful for the calculation of equilibrium structures and harmonic frequencies but it usually fails in obtaining the accurate binding energies.

An improvement in the approximation of the exchange and correlation energy of the inhomogeneous system is achieved with the inclusion of density-gradient corrections in E_{XC} (this is called the generalized gradient approximation; GGA).

In the GGA method, the exchange and correlation energies depend not only on the local electron density but also on its gradient:

$$E_{XC}^{GGA}[n(\mathbf{r})] = \int n(\mathbf{r}) \varepsilon_{XC}^{\text{hom}}[n(\mathbf{r})] f[n(\mathbf{r}), \nabla n(\mathbf{r})] d\mathbf{r}, \quad (2.21)$$

where f contains an analytic function fit to a particular system

The benefit of using GGA with respect to LDA is not clear in the calculation of solids. In many cases, GGA overcorrects the LDA results; leading to the results that are in worse agreement with experiments. However, GGA clearly provides better binding energy values, especially for the systems that the electron density is greatly fluctuated.

2.5 Bloch's Theorem and Plane Wave Basis Sets

Until now, it is still impossible to calculate infinite number of interacting electrons in the electric field of an infinite number of ions. There are two main problems: the wave function has to be calculated for each of the infinite number of electrons which will extend over the entire space of the solid and the basis set in which the wave

function will be expressed is, in principle, infinitely large. The ions in a perfect crystal at 0 K are arranged in a periodic structure. Hence the external potential produced by the electrons will also be periodic. This is the requirement in the Bloch's theorem. Using this theorem, it is possible to express the wave functions of the infinite crystal in terms of wave functions at reciprocal space vectors of a Bravais lattice.

Bloch's theorem uses the periodicity of a crystal to reduce the infinite number of one-electron wave functions to be calculated down to the number of electrons in the unit cell. The Bloch's wave functions can be written as

$$\Psi_{n,\mathbf{k}}(\mathbf{r}) = u_{n,\mathbf{k}}(\mathbf{r})e^{i\mathbf{k}\cdot\mathbf{r}}. \quad (2.22)$$

Since $u_{n,\mathbf{k}}(\mathbf{r})$ has the periodicity of the unit cell, it can be expressed by the expansion into a finite number of plane waves whose wave vectors are reciprocal lattice vectors of the crystal,

$$u_{n,\mathbf{k}}(\mathbf{r}) = \sum_{\mathbf{G}} c_{\mathbf{G}_{nk}} e^{i\mathbf{G}\cdot\mathbf{r}}, \quad (2.23)$$

where \mathbf{G} are the reciprocal lattice vectors. The electronic wave functions can be written as a sum of the plane waves,

$$\Psi_{n,\mathbf{k}}(\mathbf{r}) = \sum_{\mathbf{G}} c_{\mathbf{G}_{nk}} e^{i(\mathbf{G}+\mathbf{k})\cdot\mathbf{r}}. \quad (2.24)$$

Using Bloch's theorem, the problem of the infinite number of electrons can be mapped onto the problem of expressing the wave function in term of an infinite number of reciprocal space vectors within the first Brillouin zone. Though Fourier series contain infinite number of terms, the energy cutoff can be introduced. Therefore, only the plane waves with wave vectors smaller than $|\mathbf{G} + \mathbf{k}|$ are included, i.e.,

$$\frac{\hbar^2}{2m_e} |\mathbf{G} + \mathbf{k}|^2 < E_{\text{cutoff}}. \quad (2.25)$$

The value of required energy cutoff depends on elements in the crystal under study.

2.6 Special k -point in the Brillouin Zone

A first Brillouin zone is the Wigner-Seitz cell of the reciprocal lattice (k -space), which is defined by the planes that are the perpendicular bisectors of the vectors from the origin to the reciprocal lattice points. A first Brillouin zone is the smallest unit cell in the reciprocal space that corresponds to the crystal unit cell in real space (see text book (Martin, 2004) for details). There are infinite number of k -points in the Brillouin zone at which, in principle, the wave functions must be calculated. In reality, electronic states are only calculated at a set of representative k -points. These k -points are determined by the shape of the Brillouin zone. The electronic states at nearby k -points can be obtained by interpolations between the sampling k -points. This approximation allows us to calculate the electronic states at a finite number of k -points, and the total energy of the crystal could be determined. We used the sampling method proposed by Monkhorst and Pack (Monkhorst and Pack, 1976).

2.7 Pseudo Potential

The band structures of crystalline materials can be related to the band structure of a free electron (Heine *et al.*, 1970) modified by the crystal potentials. The solutions of the Schrödinger equation for the homogeneous non-interacting electron gas may be expressed as a plane waves,

$$\Psi_{\mathbf{k}}(\mathbf{r}) = A e^{i\mathbf{k}\cdot\mathbf{r}}, \quad (2.26)$$

where \mathbf{k} is the wave vector which can be considered to be the parameter for plane wave. A large number of plane waves will be required to accurately describe the rapidly oscillating wave functions of electrons in the core region. However the physical properties of solids depend mainly on the valence electrons. Therefore, pseudo potential method was introduced. In the pseudo potential method, only the valence electrons are explicitly considered. The valence wave functions do not need to be orthogonal to the core states. This removes the rapid oscillation near the core region. Consequently, fewer plane waves are required. The schematic representation of (pseudo and true) potentials and wave functions are shown in Figure 2.1 (Pickard, 1997). It is usual to ensure that the charge within the core radius is the same for the pseudo and true wave functions, this is known as norm-conservation (Hamann *et al.*, 1979). A pseudo potential must reproduce the proper phase shifts for the scattering at the core. These phase shifts are different for different angular momentum states. As a result, a pseudo potential must be non-local with projectors for different angular momentum components. The pseudo potential is often represented using the form (Kleinman and Bylander, 1982),

$$V = V_{loc} + \sum_{l,m} (V_l - V_{loc}) \hat{P}_{l,m}, \quad (2.27)$$

where $\hat{P}_{l,m}$ are the projectors which project the electronic wave functions onto the eigenfunctions of different angular momentum states. The choice of V_{loc} is arbitrary and if it is made equal to one of the V_l this avoids the need for the corresponding set of angular momentum projectors. Later, Lee (Lee, 1995) reduces the number of projectors needed in the calculation. The evaluation of the non-local potentials in the reciprocal space requires a computational time which is proportional to the cube of

the system size. However, the projections may be used instead. By carrying out the calculations in real-space, using the method of King-Smith (King-Smith *et al.*, 1991), the computational cost is reduced to the order of the system size squared.

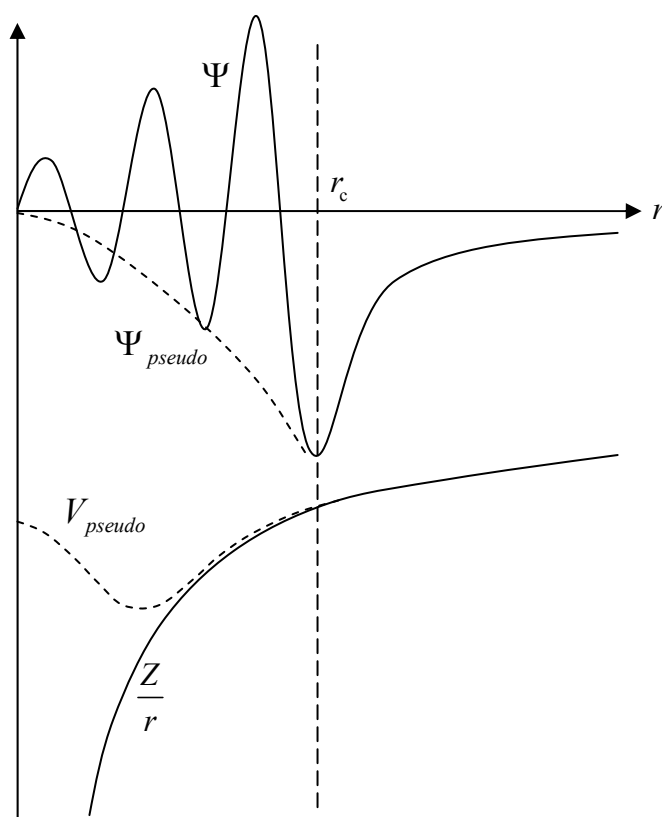


Figure 2.1 A schematic representation of the pseudo potential and pseudo wave function plotted with respect to the distance, r , from the ionic nucleus. The dashed lines represent the corresponding pseudo wave function and pseudo potential inside the core radius.

2.8 The Hellmann-Feynman Theorem

First, we introduce λ being a parameter in the Hamiltonian and $\psi(\lambda)$ is an eigenfunction of \hat{H} . We can write the derivative of energy with respect to λ as

$$\begin{aligned}
 \frac{\partial E}{\partial \lambda} &= \frac{\partial}{\partial \lambda} \langle \psi | \hat{H} | \psi \rangle = \left\langle \frac{\partial \psi}{\partial \lambda} | \hat{H} | \psi \right\rangle + \left\langle \psi | \frac{\partial \hat{H}}{\partial \lambda} | \psi \right\rangle + \left\langle \psi | \hat{H} | \frac{\partial \psi}{\partial \lambda} \right\rangle, \\
 &= E \left\langle \frac{\partial \psi}{\partial \lambda} | \psi \right\rangle + \left\langle \psi | \frac{\partial \hat{H}}{\partial \lambda} | \psi \right\rangle + E \left\langle \psi | \frac{\partial \psi}{\partial \lambda} \right\rangle, \\
 &= E \frac{\partial}{\partial \lambda} \langle \psi | \psi \rangle + \left\langle \psi | \frac{\partial \hat{H}}{\partial \lambda} | \psi \right\rangle, \\
 &= \left\langle \psi | \frac{\partial \hat{H}}{\partial \lambda} | \psi \right\rangle.
 \end{aligned} \tag{2.28}$$

This equation is known as Hellmann-Feynman theorem (Hellmann, 1937). It shows that a derivative of the total energy of a system with respect to a parameter λ can be calculated from derivative of the operator. When λ is \mathbf{R} , the forces are obtained. The Hellmann-Feynman force theorem can be written as,

$$\mathbf{F}_i = -\frac{\partial E}{\partial \mathbf{R}_i} = -\int d\mathbf{r} n(\mathbf{r}) \frac{\partial V_{\text{ext}}(\mathbf{r})}{\partial \mathbf{R}_i} - \frac{\partial E_{II}}{\partial \mathbf{R}_i} = -\left\langle \psi | \frac{\partial \hat{H}}{\partial \mathbf{R}_i} | \psi \right\rangle - \frac{\partial E_{II}}{\partial \mathbf{R}_i}, \tag{2.29}$$

where E_{II} is the electrostatic nucleus-nucleus (or ion-ion) interaction.

2.9 Electronic Ground State Calculations

There are several codes that can be used to solve the Kohn-Sham equation to determine the electronic ground state energy and electronic wave functions. These codes are, for examples, WEIN2k (Blaha *et al.*, 2002), GAUSSIAN (Frisch *et al.*,

2003), LMTO (Jarlborg and Arbman, 1976; Jarlborg and Arbman, 1977), VASP (Kresse and Hafner, 1994; Kresse and Furthmuller, 1996), etc. In this thesis VASP codes were used. Most of the algorithms implemented in VASP codes use efficient iterative matrix-diagonalization schemes such as the conjugate gradient scheme (Teter *et al.*, 1989; Bylander *et al.*, 1990), block Davidson scheme (Liu, 1978; Davidson, 1983), or a residual minimization scheme-direct inversion in the iterative subspace (RMM-DIIS) (Pulay, 1980; Wood and Zunger, 1985). The Broyden/Pulay mixing scheme (Pulay, 1980; Blügel, 1988; Johnson, 1988) is efficiency used for mixing the original and new electronic charge density during self consistency calculation. VASP codes use the Vanderbilt's ultra-soft pseudo potentials (US-PP) or projector-augmented wave (PAW) method. This allows a very small basis-set size even for the transition metals and the first row elements. The computational scheme used by VASP codes is illustrated in Figure 2.2. More details can be found in the manual of VASP (Kresse and Furthmüller, 2007) and an article by the developers (Kresse and Hafner, 1994; Kresse and Furthmuller, 1996).

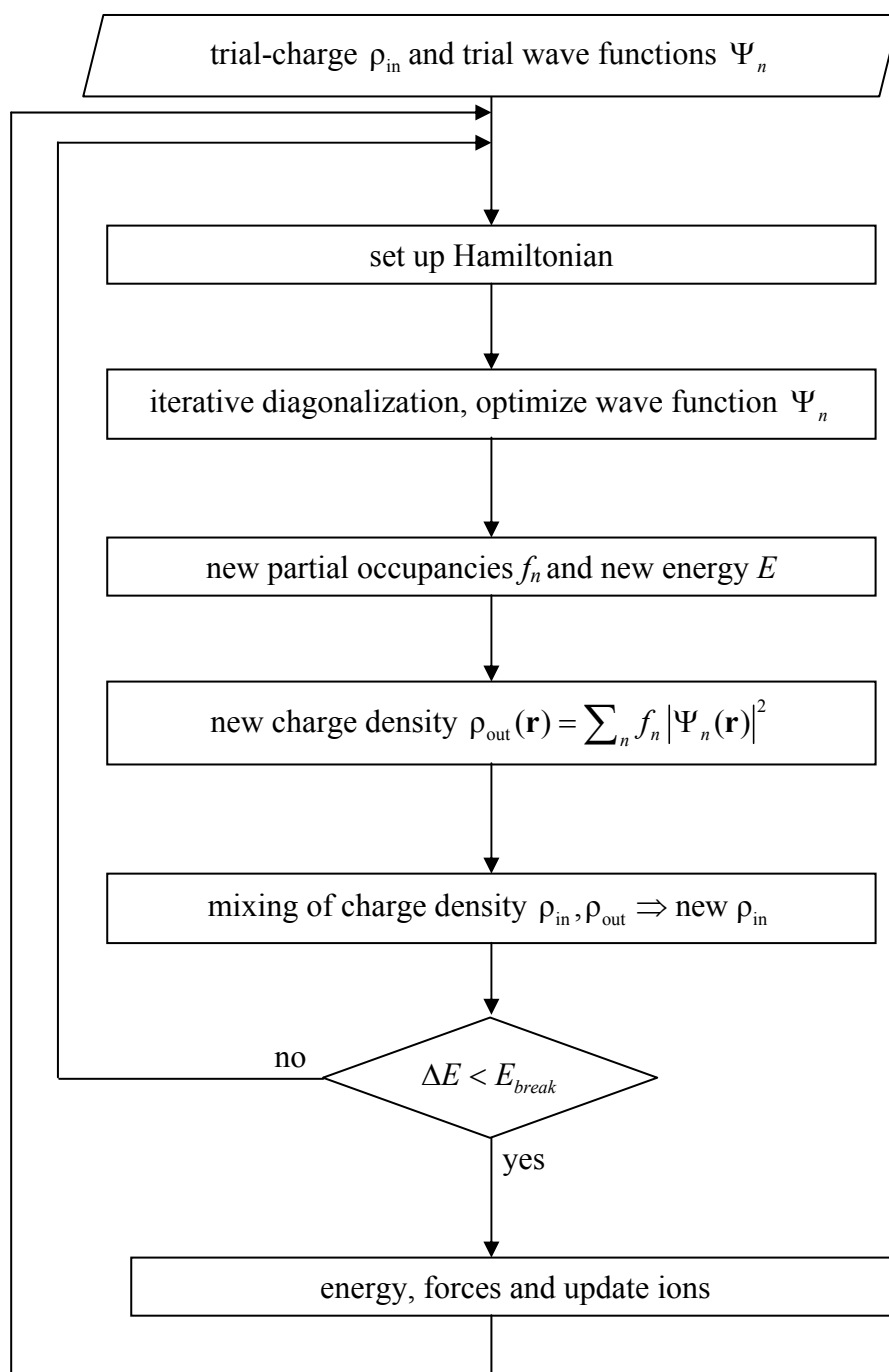


Figure 2.2 The self consistency scheme used in the VASP codes.

2.10 Vibrational Modes Calculations

A brief explanation on the calculation of the vibrational modes was given. Consider a mass m connected with a spring with force constant k . If the spring is stretched by a distance x , the restoring force F can be written as $F = -kx$ according to the Hooke's Law. The negative sign indicates that the force always pulls the mass toward its equilibrium position. The potential energy V can be obtained by integrating the force ($F = -\frac{dV}{dx} = -kx$). This gives $V = \frac{1}{2}kx^2$.

In our calculations, the force constant can be obtained from the second derivative of the potential energy ($\frac{d^2V}{dx^2} = k$). From the Newton's and Hooke's Law, we can write an equation of motion as

$$m \frac{d^2x}{dt^2} = -kx. \quad (2.30)$$

This equation can be solved and the oscillatory solution can be written as

$$x(t) = A \sin(2\pi\nu t), \quad (2.31)$$

where $\omega = 2\pi\nu$ is the vibrational frequency and A is the amplitude of the vibration.

Substituting Eq. (2.31) into Eq. (2.30) gives

$$-4\pi^2\nu^2 mx = -kx \text{ or } \omega = \sqrt{\frac{k}{m}} \quad (2.32)$$

which is the basis for the calculations of the normal modes of a molecule.

Now, if the system is composed of several atoms connected with each other. The coordinates of the atoms are

$$\text{Atom 1 : } X_1, Y_1, Z_1, \quad \text{Atom 2: } X_2, Y_2, Z_2, \quad \dots, \quad \text{Atom } i: X_i, Y_i, Z_i$$

The displacements from their respective equilibrium positions along each axis can be written as

$$\begin{aligned}
 \text{Atoms 1: } x_1 &= X_1 - X_{1,\text{eq}} & y_1 &= Y_1 - Y_{1,\text{eq}} & z_1 &= Z_1 - Z_{1,\text{eq}} \\
 \text{Atoms 2: } x_2 &= X_2 - X_{2,\text{eq}} & y_2 &= Y_2 - Y_{2,\text{eq}} & z_2 &= Z_2 - Z_{2,\text{eq}} \\
 \text{Atoms } i: x_i &= X_i - X_{i,\text{eq}} & y_i &= Y_i - Y_{i,\text{eq}} & z_i &= Z_i - Z_{i,\text{eq}}
 \end{aligned} \tag{2.33}$$

where $X_{i,\text{eq}}$, $Y_{i,\text{eq}}$, and $Z_{i,\text{eq}}$ are the equilibrium position for atom i . To calculate the vibrational frequency, each atom is slightly displaced from its equilibrium position one at a time. For example, if atom 1 is at its equilibrium position, then x_1 , y_1 , and z_1 are zero. Based on the small oscillation approximations, the potential energy which is a complicated function of displacements can be approximated by a second-degree polynomial. Using first-principles calculation, we can calculate the potential energy (near equilibrium) as a function of the displacements, $V(x_1, y_1, z_1, x_2, y_2, z_2, x_3, y_3, z_3, \dots, x_N, y_N, z_N)$. Then, the force constants can be obtained from the second derivatives of the potential energy. This gives $3N \times 3N$ dimension of force constant matrix (second rank tensor). For example, $\frac{\partial^2 V}{\partial x_1^2} = k_{xx}^{11}$ is the change of the force on atom 1 in the x-direction when we move atom 1 in the x-direction. Similarly, $\frac{\partial^2 V}{\partial x_1 \partial y_2} = k_{xy}^{12}$ is the change of the force on atom 1 in the x-direction when we move atom 2 in the y-direction. Several types of force are illustrated in Figure 2.3.

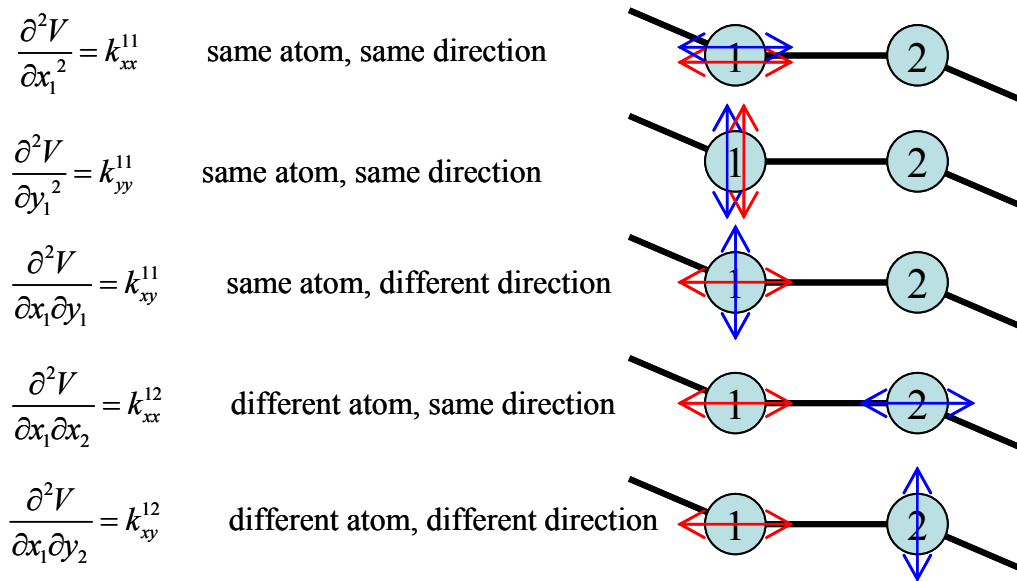


Figure 2.3 Examples of the force constants describing the relationship between the axis of displacement and the axis of resulting force.

Unlike a simple harmonic oscillator, these force constants are not for a single spring, but these force constants describe complicated interactions of all atoms in the system. The complete list of these $3N \times 3N$ force constants can be described by the set equations,

$$\begin{aligned}
 -4\pi^2\nu^2 m_1 x_1 &= -k_{xx}^{11} x_1 - k_{xy}^{11} y_1 - k_{xz}^{11} z_1 - k_{xx}^{12} x_2 - k_{xy}^{12} y_2 - \dots - k_{xz}^{1N} z_N \\
 -4\pi^2\nu^2 m_1 y_1 &= -k_{yx}^{11} x_1 - k_{yy}^{11} y_1 - k_{yz}^{11} z_1 - k_{yx}^{12} x_2 - k_{yy}^{12} y_2 - \dots - k_{yz}^{1N} z_N \\
 -4\pi^2\nu^2 m_1 z_1 &= -k_{zx}^{11} x_1 - k_{zy}^{11} y_1 - k_{zz}^{11} z_1 - k_{zx}^{12} x_2 - k_{zy}^{12} y_2 - \dots - k_{zz}^{1N} z_N \\
 &\vdots \\
 -4\pi^2\nu^2 m_2 x_2 &= -k_{xx}^{21} x_1 - k_{xy}^{21} y_1 - k_{xz}^{21} z_1 - k_{xx}^{22} x_2 - k_{xy}^{22} y_2 - \dots - k_{xz}^{2N} z_N \\
 &\vdots \\
 -4\pi^2\nu^2 m_N z_N &= -k_{zx}^{N1} x_1 - k_{zy}^{N1} y_1 - k_{zz}^{N1} z_1 - k_{zx}^{N2} x_2 - k_{zy}^{N2} y_2 - \dots - k_{zz}^{NN} z_N.
 \end{aligned} \tag{2.34}$$

The above set of equations describe the motion of all atoms in the crystal. We can rearrange the above equations by using mass weighted coordinates,

$$\tilde{x}_1 = \sqrt{m_1}x_1, \quad \tilde{x}_2 = \sqrt{m_2}x_2, \quad \dots, \quad \tilde{x}_N = \sqrt{m_N}x_N \quad (2.35)$$

and mass weighted force constants

$$\tilde{k}_{xx}^{11} = \frac{k_{xx}^{11}}{\sqrt{m_1}\sqrt{m_1}}, \quad \tilde{k}_{xx}^{12} = \frac{k_{xx}^{12}}{\sqrt{m_1}\sqrt{m_2}}, \quad \dots, \quad \tilde{k}_{xx}^{1N} = \frac{k_{xx}^{1N}}{\sqrt{m_1}\sqrt{m_N}}, \quad \text{and etc.} \quad (2.36)$$

From Eq. (2.35), (2.36), and (2.34), we can write the set of equations of motion in the matrix form as

$$\begin{pmatrix} \frac{k_{xx}^{11}}{\sqrt{m_1}\sqrt{m_1}} & \frac{k_{xy}^{11}}{\sqrt{m_1}\sqrt{m_1}} & \frac{k_{xz}^{11}}{\sqrt{m_1}\sqrt{m_1}} & \frac{k_{xx}^{12}}{\sqrt{m_1}\sqrt{m_2}} & \frac{k_{xy}^{12}}{\sqrt{m_1}\sqrt{m_2}} & \dots & \frac{k_{xz}^{1N}}{\sqrt{m_1}\sqrt{m_N}} \\ \frac{k_{yx}^{11}}{\sqrt{m_1}\sqrt{m_1}} & \frac{k_{yy}^{11}}{\sqrt{m_1}\sqrt{m_1}} & \frac{k_{yz}^{11}}{\sqrt{m_1}\sqrt{m_1}} & \frac{k_{yx}^{12}}{\sqrt{m_1}\sqrt{m_2}} & \frac{k_{yy}^{12}}{\sqrt{m_1}\sqrt{m_2}} & \dots & \frac{k_{yz}^{1N}}{\sqrt{m_1}\sqrt{m_N}} \\ \frac{k_{zx}^{11}}{\sqrt{m_1}\sqrt{m_1}} & \frac{k_{zy}^{11}}{\sqrt{m_1}\sqrt{m_1}} & \frac{k_{zz}^{11}}{\sqrt{m_1}\sqrt{m_1}} & \frac{k_{zx}^{12}}{\sqrt{m_1}\sqrt{m_2}} & \frac{k_{zy}^{12}}{\sqrt{m_1}\sqrt{m_2}} & \dots & \frac{k_{zz}^{1N}}{\sqrt{m_1}\sqrt{m_N}} \\ \frac{k_{xx}^{21}}{\sqrt{m_2}\sqrt{m_1}} & \frac{k_{xy}^{21}}{\sqrt{m_2}\sqrt{m_1}} & \frac{k_{xz}^{21}}{\sqrt{m_2}\sqrt{m_1}} & \frac{k_{xx}^{22}}{\sqrt{m_2}\sqrt{m_2}} & \frac{k_{xy}^{22}}{\sqrt{m_2}\sqrt{m_2}} & \dots & \frac{k_{xz}^{2N}}{\sqrt{m_2}\sqrt{m_N}} \\ \vdots & & & & & & \vdots \\ \frac{k_{xx}^{N1}}{\sqrt{m_N}\sqrt{m_1}} & \frac{k_{xy}^{N1}}{\sqrt{m_N}\sqrt{m_1}} & \frac{k_{xz}^{N1}}{\sqrt{m_N}\sqrt{m_1}} & \frac{k_{xx}^{N2}}{\sqrt{m_N}\sqrt{m_2}} & \frac{k_{xy}^{N2}}{\sqrt{m_N}\sqrt{m_2}} & \dots & \frac{k_{xz}^{NN}}{\sqrt{m_N}\sqrt{m_N}} \end{pmatrix} \begin{pmatrix} \tilde{x}_1 \\ \tilde{y}_1 \\ \tilde{z}_1 \\ \tilde{x}_2 \\ \tilde{y}_2 \\ \tilde{z}_2 \\ \vdots \\ \tilde{z}_N \end{pmatrix} = -4\pi^2\nu^2 \begin{pmatrix} \tilde{x}_1 \\ \tilde{y}_1 \\ \tilde{z}_1 \\ \tilde{x}_2 \\ \tilde{y}_2 \\ \tilde{z}_2 \\ \vdots \\ \tilde{z}_N \end{pmatrix}. \quad (2.37)$$

The left most term is called the dynamic matrix. To obtain the eigenvectors $|u_i\rangle$ and eigenvalues λ_i , the dynamic matrix is diagonalized. After that, the vibrational modes can be determined from the eigenvectors and the vibrational frequencies ν_i corresponding to each mode can be obtained.

In the experiment, the vibrational modes of the crystal can be measured by using infrared spectrometry (IR) or Raman scattering techniques. Using first-principles

calculation, we can calculate the absorption intensities of infrared-active modes that are given by the corresponding oscillator strength (Giannozzi and Baroni, 1994)

$$f(\nu) = \sum_{\alpha} \left| \sum_{i\beta} Z_{\alpha\beta}^*(i) e_{\beta}(i|\nu) \right|^2, \quad (2.38)$$

where $e_{\beta}(i|\nu)$ is the normalized vibrational eigenvector of the ν th mode, α and β indicate Cartesian polarizations, and $Z_{\alpha\beta}^*(i)$ is the *effective-charge* tensor of the i th atom. The *effective charges* $Z_{\alpha\beta}^*(i)$ is the polarization induced by an atomic displacement and it is a second order derivative of the energy that can be calculated using the Berry's phase approach, which is implemented in the VASP codes. The high oscillator strength modes are the modes that are IR active and would show up in the IR absorption spectroscopy.

In the case of localized vibrational mode (LVM) calculations, the LVM can occur when the mass of the defect atom(s) is largely different from those of the host atoms. For such case, it is not necessary to calculate a full dynamic matrix of the system. Often, the LVM can be obtained rather accurately by consider only the motion of the defect atom alone. The approach used by Limpijumnong *et al.* (2003) was closely followed to calculate the LVM frequencies of defect in the crystal. For example, the vibration of O₂ molecule substituting on Te site in CdTe is very localized. Only the motions of O atoms are needed to be calculated. In the calculations, the host atoms are fixed and the defect atoms (two oxygen atoms) are displaced from their equilibrium sites in both compressive and extensive directions. We typically include about 10-20 displacements, with the magnitude up to $\pm 30\%$ of the bond length. In this approximation, the reduced mass μ is used to calculate the vibrational frequency and

the anharmonic effect is included by fitting the calculated potential energy-displacement curve with a fourth-degree polynomial (see Figure 2.4),

$$V(s) = \frac{k}{2}s^2 + \alpha s^3 + \beta s^4. \quad (2.39)$$

After that, the harmonic ω^0 and anharmonic $\Delta\omega$ parts of the frequency are calculated by using the perturbation theory (Landau and Lifshitz, 1977),

$$\omega = \omega^0 + \Delta\omega = \sqrt{\frac{k}{\mu}} - 3\frac{\hbar}{\mu} \left[\frac{5}{2} \left(\frac{\alpha}{k} \right)^2 - \frac{\beta}{k} \right]. \quad (2.40)$$

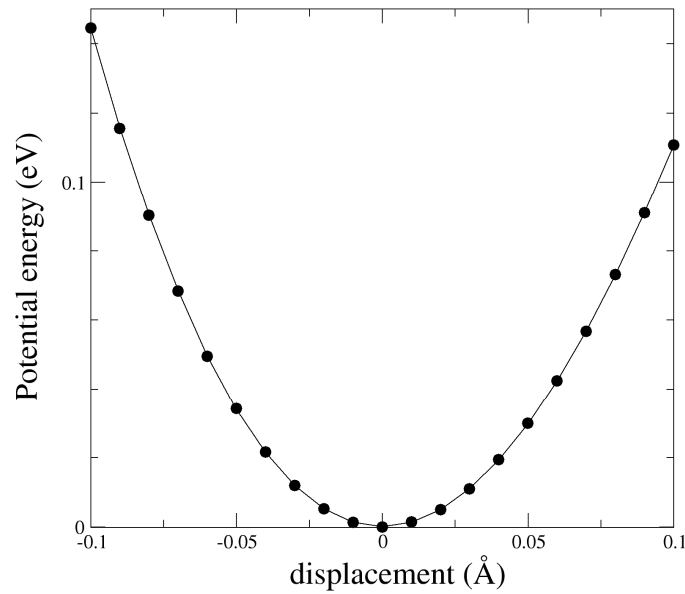


Figure 2.4 An example of the potential energy-displacement curve fitted with the fourth-degree polynomial. The dots are the results from the calculations. The curve is the polynomial fit. This plot is the actual calculation of the frequency of O₂ molecule substituting on Te site in CdTe.

2.11 References

- Blaha, P., Schwarz, K., Madsen, G. K. H., Kvasnicka, D., and Luitz, J. (2002). **an Augmented Plane Wave + Local Orbitals Program for Calculating Crystal Properties**. Wien: Institut für Materialphysik, Universität Wien.
- Blügel, S. (1988). **Treatment of Electronic Correlations in Magnetic Materials within the Fluctuation-Exchange Method**. Ph.D. Dissertation, University of RWTH Aachen, Germany.
- Bylander, D. M., Kleinman, L., and Lee, S. (1990). Self-consistent calculations of the energy bands and bonding properties of B12C3. **Phys. Rev. B** 42: 1394.
- Ceperley, D. M. and Alder, B. J. (1980). Ground state of the electron gas by a stochastic method. **Phys. Rev. Lett.** 45: 566.
- Davidson, E. R. (1983). **Methods in Computational Molecular Physics edited by Dierksen, G. H. F. and Wilson**. New York: Plenum.
- Dirac, P. A. M. (1930). Note on exchange phenomena in the Thomas-Fermi atom. **Proc. Cambridge Phi. Roy. Soc.** 26: 376.
- Frisch, M. J., Trucks, G. W., Schlegel, H. B., Scuseria, G. E., Robb, M. A., Cheeseman, J. R., Montgomery, J. A., Vreven, T., Kudin, K. N., Burant, J. C., Millam, J. M., Iyengar, S. S., Tomasi, J., Barone, V., Mennucci, B., Cossi, M., Scalmani, G., Rega, N., Petersson, G. A., Nakatsuji, H., Hada, M., Ehara, M., Toyota, K., Fukuda, R., Hasegawa, J., Ishida, M., Nakajima, T., Honda, Y., Kitao, O., Nakai, H., Klene, M., Li, X., Knox, J. E., Hratchian, H. P., Cross, J. B., Bakken, V., Adamo, C., Jaramillo, J., Gomperts, R., Stratmann, R. E., Yazyev, O., Austin, A. J., Cammi, R., Pomelli, C., Ochterski, J. W., Ayala, P. Y., Morokuma, K., Voth, G. A., Salvador, P., Dannenberg, J. J., Zakrzewski,

V. G., Dapprich, S., Daniels, A. D., Strain, M. C., Farkas, O., Malick, D. K., Rabuck, A. D., Raghavachari, K., Foresman, J. B., Ortiz, J. V., Cui, Q., Baboul, A. G., Clifford, S., Cioslowski, J., Stefanov, B. B., Liu, G., Liashenko, A., Piskorz, P., Komaromi, I., Martin, R. L., Fox, D. J., Keith, T., Laham, A., Peng, C. Y., Nanayakkara, A., Challacombe, M., Gill, P. M. W., Johnson, B., Chen, W., Wong, M. W., Gonzalez, C., and Pople, J. A. (2003). **GAUSSIAN 03, Revision C.02**. Wallingford CT, United state.

Giannozzi, P. and Baroni, S. (1994). Vibrational and dielectric properties of C60 from density-functional perturbation theory. **J. Chem. Phys.** 100: 8537.

Hamann, D. R., Schlüter, M., and Chiang, C. (1979). Norm-Conserving Pseudopotentials. **Phys. Rev. Lett.** 43: 1494.

Heine, V., Cohen, M. L., and Weaire, D. (1970). **Solid State Physics. edited by Ehrenreich, H. E., Seitz, F., and Turnbull, D.** New York: Academic press.

Hellmann, H. (1937). **Einführung in die Quantumchemie**. Leipzig: Deutsche.

Hohenberg, P. and Kohn, W. (1964). Inhomogeneous Electron Gas. **Phys. Rev.** 136: B864.

Jarlborg, T. and Arman, G. (1976). The LMTO band method applied to V3Ga. **Journal of Physics F: Metal Physics** 6: 189.

Jarlborg, T. and Arman, G. (1977). The electronic structure of some A15 compounds by semiself-consistent band calculations. **Journal of Physics F: Metal Physics** 7: 1635.

Johnson, D. D. (1988). Modified Broyden's method for accelerating convergence in self-consistent calculations. **Phys. Rev. B** 38: 12807.

- King-Smith, R. D., Payne, M. C., and Lin, J. S. (1991). Real-space implementation of nonlocal pseudopotentials for first-principles total-energy calculations. **Phys. Rev. B** 44: 13063.
- Kleinman, L. and Bylander, D. M. (1982). Efficacious Form for Model Pseudopotentials. **Phys. Rev. Lett.** 48: 1425.
- Kohn, W. and Sham, L. J. (1965). Self-Consistent Equations Including Exchange and Correlation Effects. **Phys. Rev.** 140: A1133.
- Kresse, G. and Furthmuller, J. (1996). Efficient iterative schemes for ab initio total-energy calculations using a plane-wave basis set. **Phys. Rev. B** 54: 11169.
- Kresse, G. and Furthmüller, J. (2007). **Vienna ab-initio simulation package: VASP the GUIDE**. Wien: Institut für Materialphysik, Universität Wien.
- Kresse, G. and Hafner, J. (1994). Norm-conserving and ultrasoft pseudopotentials for first-row and transition-elements. **J. Phys.:Cond. Matt.** 6: 8245.
- Landau, L. D. and Lifshitz, E. M. (1977). **Quantum Mechanics 3rd ed.** Oxford: Pergamon.
- Lee, M.-H. (1995). **Improved optimised pseudopotentials and application to disorder in γ -Al₂O₃.** Ph.D. Dissertation, University of Cambridge, England.
- Liu, B. (1978). **In Report on Workshop Numerical Algorithms in Chemistry: Algebraic Methods edited by Moler, C. and Shavitt I.** Lawrence Berkley Lab. Univ. of California.
- Martin, R. M. (2004). **Electronic structure: basic theory and practical methods.** United Kingdom: Cambridge university press.
- Monkhorst, H. J. and Pack, J. D. (1976). Special points for Brillouin-zone integrations. **Phys. Rev. B** 13: 5188.

- Perdew, J. P. and Zunger, A. (1981). Self-interaction correction to density-functional approximations for many-electron systems. **Phys. Rev. B** 23: 5048.
- Pickard, C. J. (1997). **Electron energy loss spectroscopy**. Ph.D. Dissertation, University of Cambridge, England.
- Pulay, P. (1980). Convergence acceleration in iterative sequences: the case of SCF iteration. **Chem. Phys. Lett.** 73: 393.
- Teter, M. P., Payne, M. C., and Allan, D. C. (1989). Solution of Schrodinger's equation for large systems. **Phys. Rev. B** 40: 12255.
- Wood, D. M. and Zunger, A. (1985). A new method for diagonalising large matrices. **J. Phys. A: Math. Gen.** 18: 1343.

CHAPTER III

BASIC THEORY OF X-RAY

ABSORPTION SPECTROSCOPY

The x-ray absorption spectroscopy (XAS) is a powerful technique that can be used to identify the local structures (atomic arrangement) around the absorbing atom. In principle, XAS is the absorption of the sample for different x-ray photon energy. This requires the x-ray source that provides continuous x-ray photon energy and a high resolution x-ray monochromator which can select (and scan) the x-ray energy passing to the sample. Therefore, the technique is generally offered at synchrotron facilities around the world. The XAS spectrum can be divided into two regions, as shown in Figure 3.1. (1) The near edge region called x-ray absorption near-edge spectroscopy (XANES), or sometimes called near-edge x-ray absorption fine structure (NEXAFS), which is defined to be within 50 eV of the absorption edge. (2) The high energy region called extended x-ray absorption fine-structure spectroscopy (EXAFS) which covers the high energy region above the XANES. XANES is known to be sensitive to both oxidation state and coordination environment of the absorbing atom, while EXAFS is mostly used to determined the distances, coordination number, and the species of the neighbors of the absorbing atom.

X-ray absorption by electrons originally bound to an atom is occurred through the *photo-electric effect*. In the process, an x-ray photon is absorbed by an electron in a tightly bound quantum core level (such as the $1s$ or $2p$ level) of an atom, as illustrated

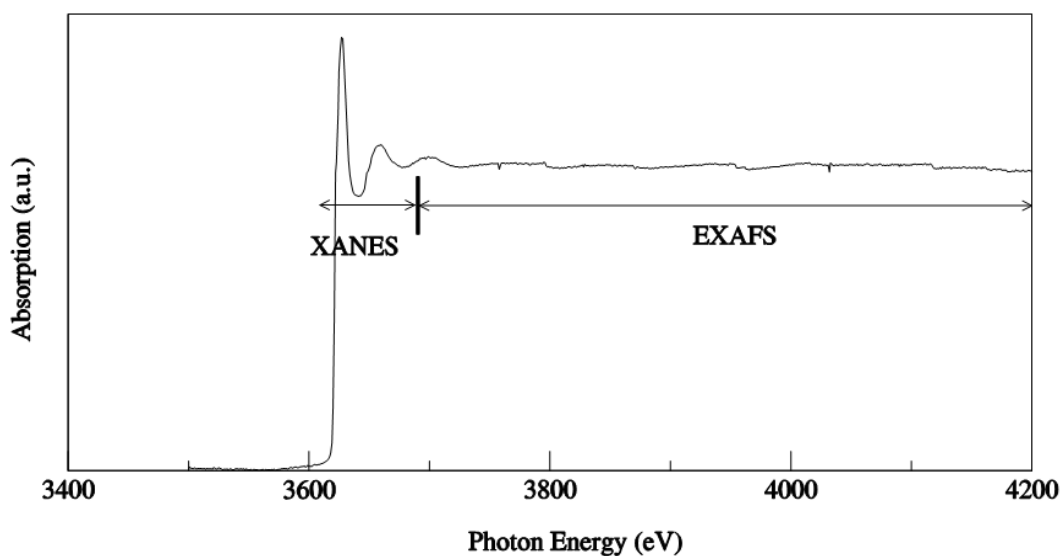


Figure 3.1 The absorption K -edge of Cl^- in water. The XANES and EXAFS regions are shown with the mark.

in Figure 3.2. After that the photo-electron or fluorescent will be created as described below.

In order for absorption process to take place, the energy of the incident x-ray must be greater than the binding energy of the core level electron. If the energy of the incident x-ray photon is less than the binding energy, the electron will not absorb the x-ray. If the energy of the incident x-ray is greater than or equal to the binding energy, the electron will be excited from the initial state. In this case, the x-ray is absorbed and the excess energy is given to a photo-electron ejected from the atom.

The x-ray absorption process is basically concerned with the *absorption coefficient*, μ which is the probability that x-ray will be absorbed according to Beer's Law

$$I = I_0 e^{-\mu t}, \quad (3.1)$$

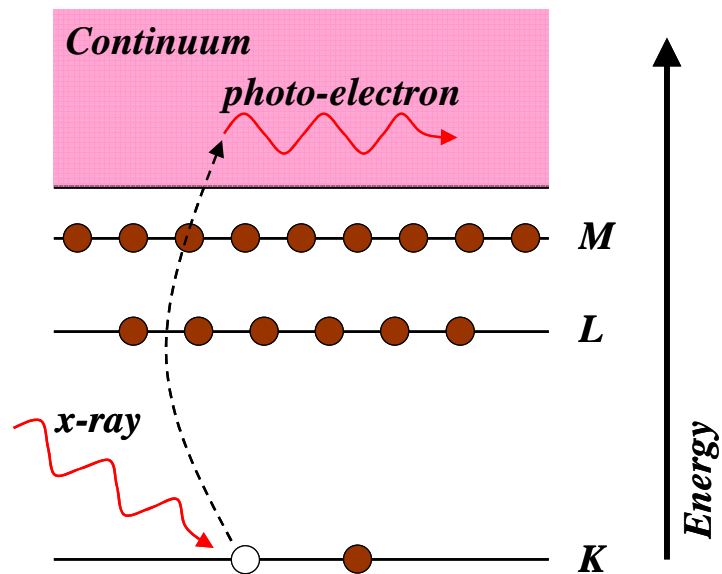


Figure 3.2 The x-ray is absorbed and the core level electron is promoted out of the atom.

where I_0 is the intensity of an incident x-ray on a sample, t is the sample thickness, and I is the intensity transmitted through the sample.

As the x-ray photon energy scanned passed the binding energy, there is a sharp rise (see Figure 3.1) which is called *absorption edge* corresponding to the promotion of core electron to the unoccupied states. Since each element has specific core level, each element in the material can be selectively probe by choosing the energy range of the incident x-ray. The x-ray absorption is related to the transition between the initial state and final state. Although the initial state (core state) is very sharp, the final states are broad. When the probing atom is in material, its bonding (and anti-bonding) lead to the structure of the final state density. The x-ray absorbance $\mu(\omega)$ is given by the Fermi's golden rule (Sakurai, 1994; Ankudinov *et al.*, 1998)

$$\mu \propto \sum_f |\langle f | D | i \rangle|^2 \delta(E_i - E_f + \omega), \quad (3.2)$$

where $|i\rangle$, $|f\rangle$, E_i , and E_f are the initial and final states and their energies, respectively; ω and D are the photon frequency and the dipole operator. This Fermi's golden rule limits the transition of the core electron to only the symmetry-allowed states. For example, if the initial state of the photo-electron is the core $1s$, the dipole-allowed final states will have the symmetry of atomic p .

There are two approaches to find μ in Eq. (3.2). (Ravel, 2002)

(1) By solving the system's Schrodinger's Equations and obtain all $|i\rangle$ and $|f\rangle$:

The integral in Eq. (3.2) can be calculated directly if $|i\rangle$ and $|f\rangle$ are known. For molecules or clusters, this can be done by quantum chemistry approaches that employed in various codes, for example, GAUSSIAN (Frisch *et al.*, 2003). For crystalline materials (or bulk materials), the system is virtually extended to infinity in all directions. Therefore, the system's Schrodinger equations can be solved more efficiently in the reciprocal space. In such cases, the quantum computational solid states physics codes such as LMTO (Jarlborg and Arbman, 1976; Jarlborg and Arbman, 1977), Wein2k (Blaha *et al.*, 2002), VASP (Kresse and Hafner, 1994; Kresse and Furthmuller, 1996), and Siesta (Soler *et al.*, 2002) codes can be used. Strictly speaking, pseudo potential codes such as VASP and Siesta codes do not have the core electrons in the calculations, rendering $|i\rangle$ unavailable. However, core states of an atom in a material distort very little (if any) from the corresponding states of an isolated atom. As a result, the core state if an isolate atom can be used as $|i\rangle$. The only disadvantage of doing so is that the absolute absorption energy can not be determined because the core state energy of an atom in material is shifted from that of the free

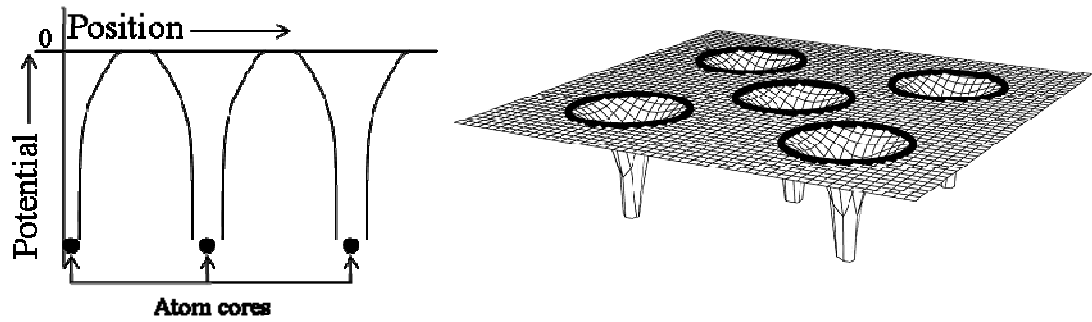


Figure 3.3 The muffin-tin potential is set to zero in the interstitial region. The figure is a reproduction of Figure 9 in Ref. (Rehr and Albers, 2000).

atom. However, the absolute energies of the absorption obtained from the codes containing core states are not very accurately any how.

By using an atomic core state as $|i\rangle$, the final states $|f\rangle$ that are allowed are those of different odd/even symmetries. For example, if the core state is $1s$ (even) then the allowed $|f\rangle$ are those of p (odd) symmetry. As a result, the site-projected partial density of states on the absorbing atom can be used to describe μ . The uses of VASP codes to perform such calculations are illustrated in Ref. (Limpijumnong *et al.*, 2006; Limpijumnong *et al.*, 2007).

(2) By using the multiple scattering approach:

In the multiple scattering approach, the muffin-tin approximation is used to describe the atomic potentials. Figure 3.3 illustrates the potential on a plane cutting through atom centers in a material. By going through the derivations using Green functions (Ankudinov *et al.*, 1998), the Fermi's Golden can be written as (Ravel, 2002)

$$\mu(E) \propto -\frac{1}{\pi} \text{Im} \langle i | \hat{\epsilon}^* \cdot \mathbf{r} \mathbf{G}(r, r'; E) \hat{\epsilon} \cdot \mathbf{r} | i \rangle \Theta(E - E_F), \quad (3.3)$$

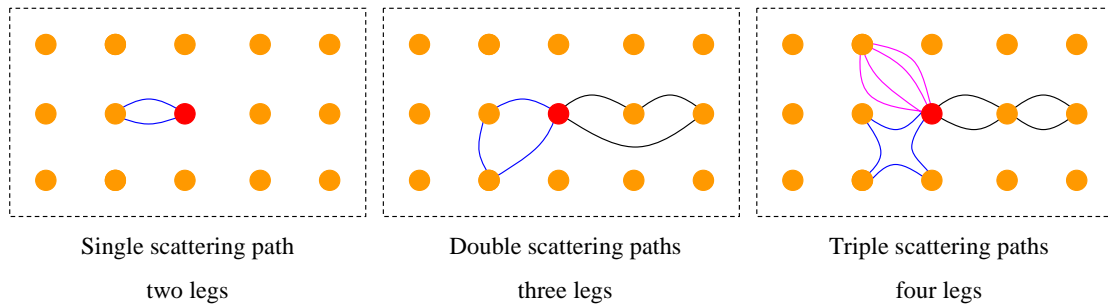


Figure 3.4 Examples of scattering paths. Red circle represents absorbing atom.

where

$$\begin{aligned} \mathbf{G} &= (1 - \mathbf{G}^0 \mathbf{t})^{-1} \mathbf{G}^0, \\ \mathbf{G} &= \mathbf{G}^0 + \mathbf{G}^0 \mathbf{t} \mathbf{G}^0 + \mathbf{G}^0 \mathbf{t} \mathbf{G}^0 \mathbf{t} \mathbf{G}^0 + \mathbf{G}^0 \mathbf{t} \mathbf{G}^0 \mathbf{t} \mathbf{G}^0 \mathbf{t} \mathbf{G}^0 + \dots, \end{aligned} \quad (3.4)$$

where \mathbf{G} is the function that describes all possible ways for a photoelectron to interact with the surrounding atoms, \mathbf{G}^0 is the function that describes how an electron propagates between two points in space, and \mathbf{t} is the function that describes how a photo-electron scatters from a neighboring atom.

This means the XAS can be calculated by summing up contributions from all scattering paths. Examples of some scattering paths are shown in Figure 3.4. More details of how the sum of paths show up in the Green functions term can be found in Ref. (Ankudinov *et al.*, 1998). In practice, only first few scattering paths from the close by neighboring atoms are important. The approach is adopted by the FEFF codes. The codes are popular for XAS calculation.

The two approaches work out better for different region of XAS. By directly calculating the $|i\rangle$ and $|f\rangle$ states, the available regimes used are based on the ground state theory where the aim is set to obtain the occupied states as accurate as possible and the empty states, where $|f\rangle$ states are part of, are just the by-products. In practice,

the empty states (conduction band states for semiconductors) can be calculated up to about 50 eV above the Fermi level. As a result, the first approach can be used for only XANES calculations. On the other hand, the multiple scattering approach works better for high kinetic energy states. Even with an inaccurate potential shape it can produce reasonable EXAFS where the kinetic energy of the photoelectron is high. In the past, the multiple scattering approach works out poorly for the XANES calculations. Recently, big improvement on the FEFF codes using more accurate *ab initio* scattering potentials calculated using LMTO method allow the codes to calculate XANES spectra rather accurately. However, the atomic coordinates of the local structure surrounding the absorbing atom (if not experimentally known) has to be accurately determined. This can be done by first-principles relaxations. In Chapter V, we show the XANES simulations of InON alloys at various O:N ratios in comparison with the XANES measurements. The calculations were performed by using VASP codes for crystal relaxations and FEFF codes for XANES spectra generations. In Chapter VI, we employed FEFF codes (second approach) to simulate both EXAFS and XANES spectra of Ca^{2+} and Cl^- ions in water based on the dynamic coordinates obtained from QM/MM MD calculations. (Tongraar *et al.*, 2002; Tongraar and Rode, 2003) The results are discussed in comparison with experimental spectra.

3. References

- Ankudinov, A. L., Ravel, B., Rehr, J. J., and Conradson, S. D. (1998). Real-space multiple-scattering calculation and interpretation of x-ray-absorption near-edge structure. **Phys. Rev. B** 58: 7565.
- Blaho, P., Schwarz, K., Madsen, G. K. H., Kvasnicka, D., and Luitz, J. (2002). **an Augmented Plane Wave + Local Orbitals Program for Calculating Crystal Properties**. Wien: Institut für Materialphysik, Universität Wien.
- Frisch, M. J., Trucks, G. W., Schlegel, H. B., Scuseria, G. E., Robb, M. A., Cheeseman, J. R., Montgomery, J. A., Vreven, T., Kudin, K. N., Burant, J. C., Millam, J. M., Iyengar, S. S., Tomasi, J., Barone, V., Mennucci, B., Cossi, M., Scalmani, G., Rega, N., Petersson, G. A., Nakatsuji, H., Hada, M., Ehara, M., Toyota, K., Fukuda, R., Hasegawa, J., Ishida, M., Nakajima, T., Honda, Y., Kitao, O., Nakai, H., Klene, M., Li, X., Knox, J. E., Hratchian, H. P., Cross, J. B., Bakken, V., Adamo, C., Jaramillo, J., Gomperts, R., Stratmann, R. E., Yazyev, O., Austin, A. J., Cammi, R., Pomelli, C., Ochterski, J. W., Ayala, P. Y., Morokuma, K., Voth, G. A., Salvador, P., Dannenberg, J. J., Zakrzewski, V. G., Dapprich, S., Daniels, A. D., Strain, M. C., Farkas, O., Malick, D. K., Rabuck, A. D., Raghavachari, K., Foresman, J. B., Ortiz, J. V., Cui, Q., Baboul, A. G., Clifford, S., Cioslowski, J., Stefanov, B. B., Liu, G., Liashenko, A., Piskorz, P., Komaromi, I., Martin, R. L., Fox, D. J., Keith, T., Laham, A., Peng, C. Y., Nanayakkara, A., Challacombe, M., Gill, P. M. W., Johnson, B., Chen, W., Wong, M. W., Gonzalez, C., and Pople, J. A. (2003). **GAUSSIAN 03, Revision C.02**. Wallingford CT, United state.

- Jarlborg, T. and Arbman, G. (1976). The LMTO band method applied to V3Ga. **J. Phys. F** 6: 189.
- Jarlborg, T. and Arbman, G. (1977). The electronic structure of some A15 compounds by semiself-consistent band calculations. **J. Phys. F** 7: 1635.
- Kresse, G. and Furthmuller, J. (1996). Efficient iterative schemes for ab initio total-energy calculations using a plane-wave basis set. **Phys. Rev. B** 54: 11169.
- Kresse, G. and Hafner, J. (1994). Norm-conserving and ultrasoft pseudopotentials for first-row and transition-elements. **J. Phys.:Cond. Matt.** 6: 8245.
- Limpijumnong, S., Rujirawat, S., Boonchun, A., Smith, M. F., and Cherdhirunkorn, B. (2007). Identification of Mn site in Pb(Zr,Ti)O₃ by synchrotron x-ray absorption near-edge structure: Theory and experiment. **Appl. Phys. Lett.** 90: 103113.
- Limpijumnong, S., Smith, M. F., and Zhang, S. B. (2006). Characterization of As-doped, *p*-type ZnO by x-ray absorption near-edge structure spectroscopy: Theory. **Appl. Phys. Lett.** 89: 222113.
- Ravel, B. (2002). **Introduction to XAS Theory** [On-line]. Available: http://cars9.uchicago.edu/xafs/NSLS_2002/Ravel.pdf.
- Rehr, J. J. and Albers, R. C. (2000). Theoretical approaches to x-ray absorption fine structure. **Rev. Mod. Phys.** 72: 621.
- Sakurai, J. J. (1994). **Modern Quantum Mechanics (Rev. Ed.)**. New York: Addison-Wesley.
- Soler, J. M., Artacho, E., Gale, J. D., Garcia, A., Junquera, J., Ordejon, P., and Sanchez-Portal, D. (2002). The SIESTA method for ab initio order-N materials simulation. **J. Phys.:Cond. Matt.** 14: 2745.

- Tongraar, A. and Rode, B. M. (2003). The hydration structures of F^- and Cl^- investigated by ab initio QM/MM molecular dynamics simulation. **Phys. Chem. Chem. Phys.** 5: 357.
- Tongraar, A., Sagarik, K., and Rode, B. M. (2002). Preferential solvation of Ca^{2+} in aqueous ammonia solution: Classical and combined ab initio quantum mechanical/molecular mechanical molecular dynamics simulations. **Phys. Chem. Chem. Phys.** 4: 628.

CHAPTER IV

OXYGEN AND HYDROGEN DEFECTS

IN CADMIUM TELLURIDE

4.1 Introduction

Semiconductors are of limited use if they can not be doped into both *n*- and *p*-type. CdTe is recognized as one of the promising materials because it has been known for a long time that it can be doped into both *n*-type and *p*-type. The theoretical study of doping limits of CdTe has been performed by Wei and Zhang (Wei and Zhang, 2002).

Recently, the local vibrational modes (LVM) related to oxygen impurities in CdTe have been experimentally observed using an ultrahigh resolution Fourier transform infrared (FTIR) spectrometer. (Chen *et al.*, 2006; Chen *et al.*, 2007) Depending on the doping conditions, at low temperature, they found a low LVM frequency at 350 cm⁻¹ accompanied with two high LVMs frequencies at $\nu_1 = 1097$ and $\nu_2 = 1108$ cm⁻¹ (see Figure 4.1), that merge into one frequency at room temperature, as shown in Figure 4.2. The low frequency mode was assigned to an oxygen substitution on Te site (O_{Te}) and two high frequencies modes were assigned by Chen *et al.* to complex of oxygen substitution on Te site and Cd vacancy (O_{Te}-V_{Cd}).

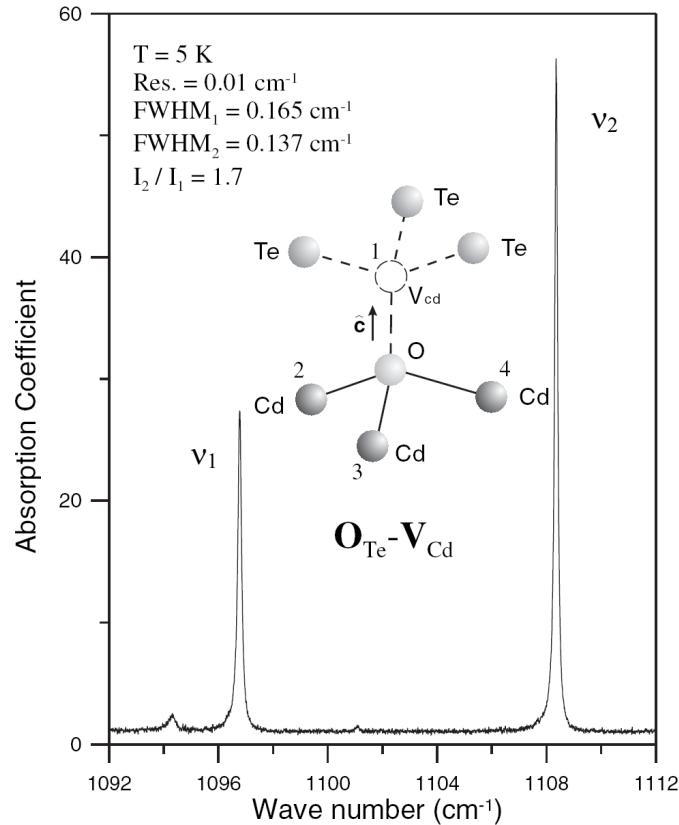


Figure 4.1 The infrared absorption spectrum of the oxygen doped CdTe. The inset shows the $\text{O}_{\text{Te}}-\text{V}_{\text{Cd}}$ defect model that Chen *et al.* claims to be responsible for the two observed LVMS. The figure is a reproduction of Figure. 1 in Ref. (Chen *et al.*, 2006).

The O and H defects in CdTe have been studied using first-principles density functional theory. The LVMS of O and H defects in CdTe were calculated and used to compare with the corresponding experimental results. The LVMS of O_{Te} and $\text{O}_{\text{Te}}-\text{V}_{\text{Cd}}$ defects were calculated. The calculated LVMS of O_{Te} is 338 cm^{-1} that is in good agreement with the experimental value. However, the LVMS of $\text{O}_{\text{Te}}-\text{V}_{\text{Cd}}$ are 112 and 472 cm^{-1} that are totally inconsistent with the ν_1 and ν_2 modes observed by Chen *et al.* (2006). Therefore, it is clear that Chen *et al.* made a fault interpretation of their

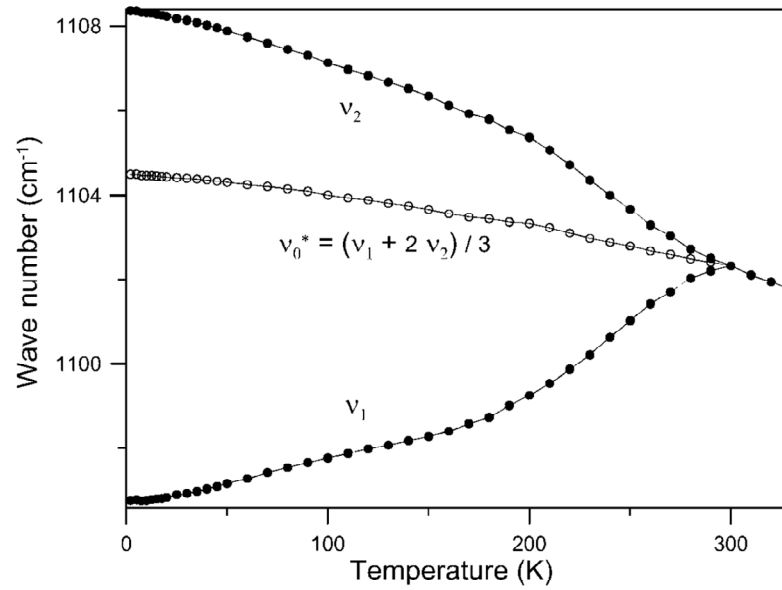


Figure 4.2 Temperature dependence of ν_1 and ν_2 for the oxygen doped CdTe from 2 to 330 K (solid circles) and the weighted average of ν_1 and ν_2 , i.e., $\nu_0^* = (\nu_1 + 2\nu_2)/3$, calculated for each temperature (open circles). The figure is a reproduction of Figure 3 in Ref. (Chen *et al.*, 2006).

measurement. In collaboration with the computational team at Oak Ridge National Laboratory (USA), a comment on their paper has been published. (Zhang *et al.*, 2009)

4.2 Structural Relaxation

In these calculations, the density functional theory within the local density approximations was used. The atomic potentials used in these calculations are the Vanderbilt-type ultrasoft pseudo potentials (Vanderbilt, 1990), as implemented in the VASP codes (Kresse and Furthmüller, 1996). This allows the usage of a plane wave basis set with a low cutoff energy of 400 eV. Our calculated crystal parameters of bulk CdTe is $a = 6.428 \text{ \AA}$, which is in a good agreement with the experimental values

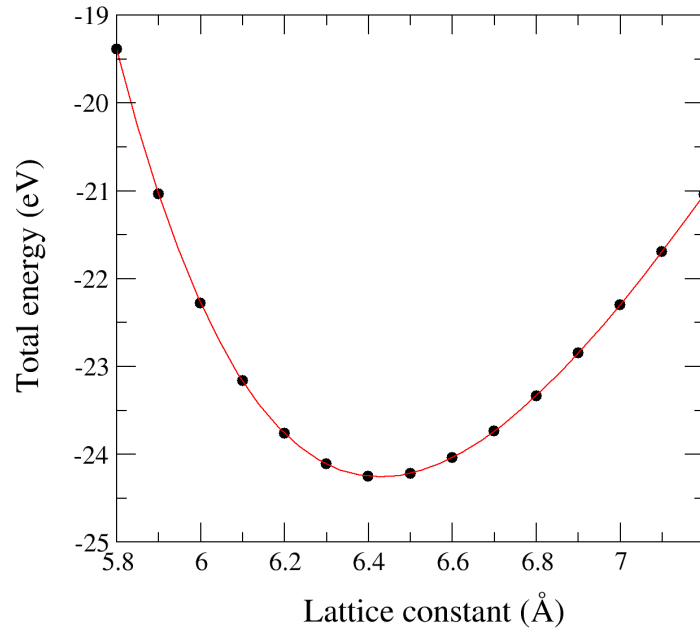


Figure 4.3 Total energy of zincblende CdTe as a function of the lattice constant. The solid circles and the line are the calculated and fit data, respectively.

($a = 6.482 \text{ \AA}$). This lattice constant has been determined by performing the calculations with various values of lattice constant. The equilibrium lattice constant is the one that gives the lowest energy (Figure 4.3). The calculated bandgap of CdTe is 0.7 eV which is smaller than the experimental value of 1.7 eV.

4.3 Calculation of Defect Formation Energy

To calculate the formation energies and vibrational frequencies of defects, a supercell approach is used (Zhang and Northrup, 1991; Northrup and Zhang, 1994; Zhang *et al.*, 2001). All atoms in the supercell are allowed to relax until the Hellmann-Feynman forces (Feynman, 1939) on all atoms are less than 10^{-3} eV/\AA . A 64-atom supercell, which is a $2 \times 2 \times 2$ repetition of CdTe primitive unit cell, is used. The Monkhorst-Pack (Monkhorst and Pack, 1976) scheme is used for k-point

sampling. The defect formation energy is defined as (Zhang and Northrup, 1991; Northrup and Zhang, 1994)

$$\Delta H_f = E_{tot}(D^q) - E_{tot}(0) + \sum \Delta n_x \mu_x + q(E_f + E_v), \quad (4.1)$$

where $E_{tot}(D^q)$ is the calculated total energy of a supercell with a defect D in charge state q , $E_{tot}(0)$ is the calculated total energy of a supercell without the defect. Δn_x is the number of atoms from species X ($=\text{Cd, Te, O and H}$) being added to (or removed from, negative sign) a supercell to form the defect cell. They are presumed to be taken from their respective reservoir with chemical potential μ_x . E_f is energy of the reservoir with which these charges are exchanged, i.e., the electron chemical potential or Fermi level. E_v is the valence band maximum. The equilibrium concentration c of the defect at a given temperature T depends on the formation energy of the defect E_f and on the number of sites N in which the defect can be incorporated into the lattice.

$$c = N \exp\left(-\frac{\Delta H_f}{kT}\right), \quad (4.2)$$

where k is the Boltzman's constant.

During the growth, if the chemical potential of any element increases above its natural phase value (i.e., that of metal Cd or metal Te), then the natural phase will form instead of the CdTe. We must consider the limitations on the chemical potentials that may be required by the formation of different phase containing Cd, Te, H and O as will be discussed below.

To grow the homogeneous CdTe crystal, it is required that

$$\mu_{\text{CdTe}} = \mu_{\text{Cd}} + \mu_{\text{Te}}, \quad (4.3)$$

where μ_{CdTe} is the chemical potential of CdTe crystal. The chemical potential can be referenced to their respective natural phases. The calculated formation energy of CdTe per molecular formula is $\mu_{\text{CdTe}} = -0.76$ eV. If the sum on the right-hand side is large than μ_{CdTe} , then the crystal will grow rapidly and will not be homogeneous. On the other hand, if the sum is lower than μ_{CdTe} , then the crystal will disintegrate. The chemical potentials of hydrogen μ_{H} is referenced to H₂ molecule. However, oxygen prefers to bind with Cd or Te to form CdO or TeO₂. Therefore, the maximum chemical potential of oxygen is set by $\mu_{\text{O}} = \mu_{\text{CdO}} - \mu_{\text{Cd}}$ and $\mu_{\text{O}} = [\mu_{\text{TeO}_2} - \mu_{\text{Te}}]/2$ for Cd-rich and Te-rich condition, respectively.

4.4 Local Vibrational Modes (LVM) Calculations

The LVM frequencies of O and H defects in CdTe are calculated using the so-called frozen phonon approach (Teweldeberhan and Fahy, 2005). For each configuration, the structure is allowed to fully relax. Then each and every atom in the supercell is slightly shifted in all three axes, one at a time, and the dynamic matrix can be calculated based on the repulsive forces. Within the harmonic approximation, the total energy of a supercell with small displacements of atoms from their equilibrium positions can be written as

$$E = E_0 + \frac{1}{2} \sum_{i,j,\alpha,\beta} \Phi_{\alpha\beta}(i,j) d_{\alpha}(i) d_{\beta}(j), \quad (4.4)$$

where $d_{\alpha}(i)$ is the displacement of atom i from its equilibrium position in the direction α and $\Phi_{\alpha\beta}(i,j)$ is the real-space force constant matrix. The small

displacement $d_\beta(j)$ of atom j in the direction β induces a force on atom i in the direction α as

$$F_\alpha(i) = -\Phi_{\alpha\beta}(i, j) d_\beta(j). \quad (4.5)$$

From the Eq. (4.5), the real-space force constant matrix $\Phi_{\alpha\beta}(i, j)$ can be constructed by calculating the forces $F_\alpha(i)$ induced by creating a small displacement d_0 ($d_\beta(j) = d_0 = 0.01 \times a$ where a is a lattice constant) of each atom j in the supercell in three orthogonal directions, $\beta = 1, 2, 3$ one atom and one direction at a time. To reduce the anharmonic contribution, each component of the force constant matrix is obtained from two calculations. One with $+d_0$ displacement and another with $-d_0$ displacement. Once the force constant matrix is obtained, the dynamical matrix, $D_{\alpha\beta}(i, j) = (M_i M_j)^{-1/2} \Phi_{\alpha\beta}(i, j)$, where M_i is the mass of atom i , can be readily constructed. After the dynamical matrix is diagonalized, the eigenvalues, $e_k = \omega_k^2$, and the normalized eigenvectors, $|u_k\rangle$ give rise to the vibrational frequencies and the atomic movements for each particular mode. (More details are described in Appendix A.).

For localized modes, we can use another approach to determine the vibrational frequencies. We follow the approach used recently by Limpijumnong (Limpijumnong *et al.*, 2003) to calculate the LVM frequencies of O and H defect in CdTe. Because the coupling of oxygen and/or hydrogen to CdTe host is very weak (due to the large difference in masses), the vibration is very localized. As a result, the host atoms are assumed to be stationary in this calculation. Because host atoms are fixed, this approach can be performed much faster than the full dynamic calculations. The

benefit of the approach is that the anharmonic contributions can be calculated. The potential energy surface of O and H defects in CdTe were calculated and fit with the equation

$$V(x) = \frac{k}{2}x^2 + \alpha x^3 + \beta x^4, \quad (4.6)$$

where k , α , and β can be obtained from the curve fit. The harmonic ω^0 and anharmonic $\Delta\omega$ frequencies can be calculated by using the perturbation theory (Landau and Lifshits, 1977)

$$\omega = \omega^0 + \Delta\omega = \sqrt{\frac{k}{\mu}} - 3\frac{\hbar}{\mu} \left[\frac{5}{2} \left(\frac{\alpha}{k} \right)^2 - \frac{\beta}{k} \right], \quad (4.7)$$

where ω is the vibrational frequency included anharmonic part, \hbar is a plank constant, and μ is an effective mass of the oscillator.

4.5 Results and Discussion

4.5.1 Native defects in CdTe

Simple native point defects in CdTe, namely vacancy Cd (V_{Cd}), vacancy Te (V_{Te}), Cd interstitial (Cd_i), Te interstitial (Te_i), Cd antisite (Cd_{Te}), and Te antisite (Te_{Cd}) have been previously studied by Wei and Zhang (Wei and Zhang, 2002). Here, we repeated the calculations to ensure that our calculation details yield similar results and for further use in defect complexes study.

The formation energies of native defects were calculated according to Eq. (4.4). The defect formation energy depends on the Fermi level, so we can plot it as a function of Fermi energy. Although the calculated bandgap is much underestimated, the total energy is calculated based on the k-point sampling that does not include the Γ point. Away from the Γ point, the separation between the VB and CB is widened. The calculated band gap at the sampling k-points is ~ 1.7 eV. This allows the range of possible Fermi energy to extend upto 1.7 eV before occupying the CB in the calculations. In Figure 4.4, we can see that V_{Cd} is a double acceptor and has low

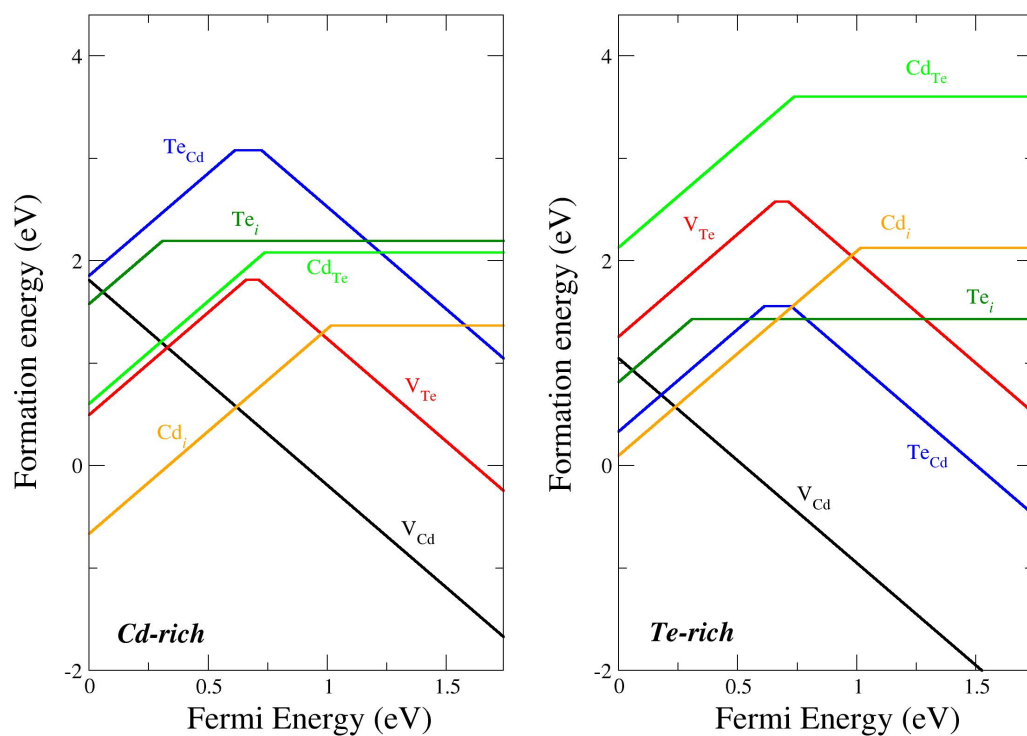


Figure 4.4 Formation energies of native defects as a function of the Fermi level, under the Cd-rich (left panel) and Te-rich (right-panel) growth conditions. The slope of each line indicates the charge state.

formation energy in both Cd and Te-rich condition. Therefore, this type of defect is likely formed during the growth process. Te vacancy is amphoteric which means it acts as a double donor in p -type conditions and a double acceptor in n -type conditions. There are two transition energies at $\epsilon(2+/0) = 0.66$ eV and $\epsilon(0/2-) = 0.71$ eV (measured from VBM). The formation energy of V_{Te} is reasonably low under Cd-rich condition. For interstitial defects, we found that Cd_i is a deep double donor with the transition energy at $\epsilon(2+/0) = 1.02$ eV. Its formation energy is low, especially in Cd-rich condition. Te_i is a deep double donor with the transition energy at $\epsilon(2+/0) = 0.31$ eV. For antisite defects, we found that Cd_{Te} is a deep double donor with transition energy at $\epsilon(2+/0) = 0.74$ eV and Te_{Cd} is amphoteric with the transition energies at $\epsilon(2+/0) = 0.61$ eV and $\epsilon(0/2-) = 0.72$ eV. We found that the defect formation energies of Cd_{Te} and Te_{Cd} are rather low in Cd-rich and Te-rich, respectively. The local structures of Cd_{Te} and Te_{Cd} are illustrated in Figure 4.5. All these native defect results are in a reasonable agreement with the computational study by Wei and Zhang (Wei and Zhang, 2002).

In a detailed comparison, their energy plots appear to shift to the right side (~ 0.2 eV) compared to ours. This is because we use slightly different reference energy points. While we set the zero point of E_f at the VBM, Wei and Zhang (Wei and Zhang, 2002) used the VBM at the special k -point which is lower than the actual VBM at Γ .

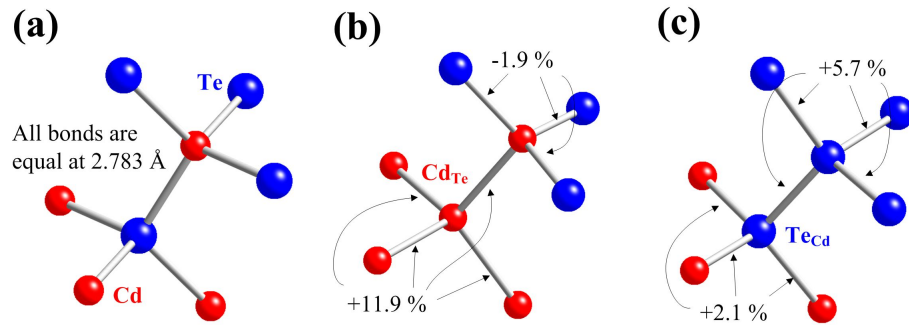


Figure 4.5 The local structure of (a) Bulk, (b) Cd_{Te}^0 and (c) $\text{Te}_{\text{Cd}}^{2+}$ in CdTe. The red and blue colors are used to label Cd and Te atoms, respectively. All bond distances are given as percentage differences from the bulk CdTe bond distance ($d = 2.783\text{\AA}$).

4.5.2 Oxygen defects in CdTe

In order to understand the role of O in CdTe, several forms of possible defect structures with O in CdTe are studied. One of the driving reasons for this study is to explain the LVM recently observed by the group of Ramdas (Chen *et al.*, 2006; Chen *et al.*, 2007). In that work, they observed the LVM at $\nu_1 = 1097$ and $\nu_2 = 1108\text{ cm}^{-1}$ in addition to the LVM of O_{Te} at 349.8 cm^{-1} in certain growth conditions. They assigned the ν_1 and ν_2 to the $\text{O}_{\text{Te}}-\text{V}_{\text{Cd}}$ complexes. It is hard to believe that the vibration frequency of O_{Te} of 349.8 cm^{-1} can increase by more than 3 times when there is a V_{Cd} nearby. We have co-authored a “Comment” on the work by Ramdas’s group (Chen *et al.*, 2006; Chen *et al.*, 2007) that has been published in Phys. Rev. Lett. (Zhang *et al.*, 2009). Here, we have studied same O defects, namely O_{Te} , $\text{O}_{\text{Te}}-\text{V}_{\text{Cd}}$, $(\text{O}_2)_{\text{Te}}$, and $(\text{O}_2)_{\text{Te}}-\text{V}_{\text{Cd}}$. The first two defects were studied to check/disprove the model of Chen *et al.* (Chen *et al.*, 2006; Chen *et al.*, 2007). While the $(\text{O}_2)_{\text{Te}}$ is studied because it is likely to give sufficiently high frequency observed by Chen *et al.* The $(\text{O}_2)_{\text{Te}}-\text{V}_{\text{Cd}}$ is

studied because it can potentially give out two frequencies due to symmetry-breaking in a similar way the $O_{Te}-V_{Cd}$ complex does.

The formation energies of O defects in CdTe are shown in Table 4.1 and Figure 4.6 for both Cd-rich and Te-rich growth conditions. The local structures of each defect are illustrated in Figure 4.7. We found that O_{Te} is a low energy defect in both growth conditions, making it likely to form. Although, $O_{Te}-V_{Cd}$ has rather low energy, its stability also depends on the binding between O_{Te} and V_{Cd} . To study the formations of the complexes, i.e. $O_{Te}-V_{Cd}$ and $(O_2)_{Te}-V_{Cd}$, the complex energies are compared with the sum of the individual defects (dashed lines in Figure 4.6). It is found that the $O_{Te}-V_{Cd}$ is bound but by a very small margin of 0.1 eV and $(O_2)_{Te}-V_{Cd}$ is not bound. This means that both complexes are unlikely to form under normal growth conditions. Moreover, in *p*-type region, the energies of $O_{Te}-V_{Cd}$ and $(O_2)_{Te}-V_{Cd}$ complexes are higher than those of O_{Te} and $(O_2)_{Te}$, respectively. These formation energy results suggest that the O_{Te} defect is likely to exist under normal doping conditions. The $O_{Te}-V_{Cd}$ as well as $(O_2)_{Te}-V_{Cd}$ are unlikely to form under high temperature-thermal equilibrium conditions. However, there still exists the possibility for them to form under inequilibrium treatments.

The LVM frequencies of O_{Te} , $O_{Te}-V_{Cd}$, $(O_2)_{Te}$, and $(O_2)_{Te}-V_{Cd}$ are calculated for identification purposes (Table 4.2). We found that the calculated frequency of O_{Te} is 338 cm^{-1} which is in a very good agreement with the observed value of 349.8 cm^{-1} . (Chen *et al.*, 2006; Chen *et al.*, 2007) For the $O_{Te}-V_{Cd}$ complex, the vibrational mode that localized on the O atom is splitted into two modes. The first mode involved the vibration of O toward (and away) from the V_{Cd} center. This mode has frequency lowered to 112 cm^{-1} (in comparison to O_{Te} frequency of 338 cm^{-1}). The other mode

involved the O motion in the direction perpendicular to the first mode. For this mode the frequency is increased but only slightly (i.e. to 472 cm^{-1}). These two modes are totally inconsistent with the frequencies ν_1 and ν_2 of $\sim 1100 \text{ cm}^{-1}$ observed by Chen *et al.* (Chen *et al.*, 2006; Chen *et al.*, 2007). This supports our initial prediction that Chen *et al.* (Chen *et al.*, 2006; Chen *et al.*, 2007) incorrectly assigned ν_1 and ν_2 to $\text{O}_{\text{Te}}\text{-}V_{\text{Cd}}$ complex. (Zhang *et al.*, 2009)

Next, we search for the O defects that can potentially give high frequencies. The natural candidates are the vibrations involving O-O bonds. This is because the free O_2 molecule has a stretch frequency of 1580 cm^{-1} . If the O_2 is incorporated in a crystal, the vibrational frequency is reduced due to charge screening. In the case of O_2 in ZnO, the calculated vibrational frequency of $(\text{O}_2)_{\text{O}}$ is 1051 cm^{-1} . (Limpijumnong *et al.*, 2005) We calculated the vibrational frequency of $(\text{O}_2)_{\text{Te}}$ in CdTe and found the frequency of 901 cm^{-1} . This is in a reasonable agreement with the observed ν_1 and ν_2 , especially when we take into account of the underestimation in the calculation of 95 cm^{-1} . (The calculation of free O_2 molecule underestimated the actual frequency by $1580 - 1485 = 95 \text{ cm}^{-1}$ as shown in Table 4.2) However, $(\text{O}_2)_{\text{Te}}$ has only one structure and would result in a single frequency. We speculate that if $(\text{O}_2)_{\text{Te}}$ bind with V_{Cd} , the resulting $(\text{O}_2)_{\text{Te}}\text{-}V_{\text{Cd}}$ complex could be the source of the second frequency. Indeed, the $(\text{O}_2)_{\text{Te}}\text{-}V_{\text{Cd}}$ has slightly higher frequency than an isolated $(\text{O}_2)_{\text{Te}}$ by about 10 cm^{-1} . This splitting is comparable to the splitting between ν_1 and ν_2 . However, there are many problems with this model. (1) The formation energy of $(\text{O}_2)_{\text{Te}}$ is high. (2) $(\text{O}_2)_{\text{Te}}\text{-}V_{\text{Cd}}$ complex is not bound. The complex can spontaneously separate and gain energy. (3) Even if the complexes $(\text{O}_2)_{\text{Te}}\text{-}V_{\text{Cd}}$ and $(\text{O}_2)_{\text{Te}}$ can form they are weakly IR active due

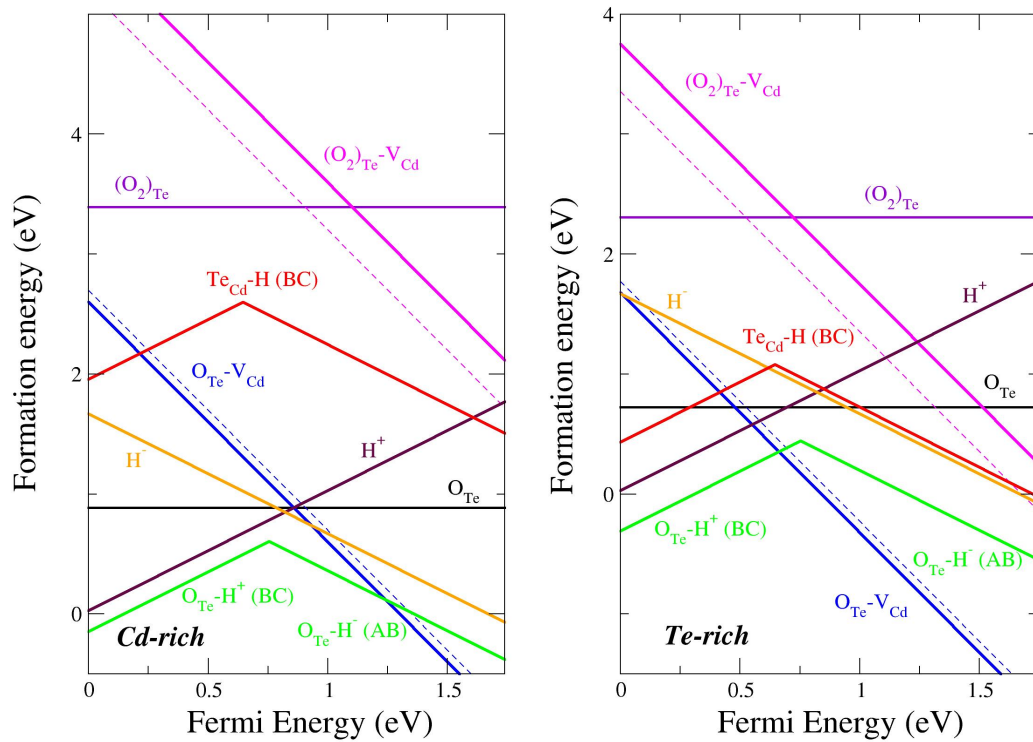


Figure 4.6 Formation energies as a function of the Fermi level, under the Cd-rich (left panel) and Te-rich (right-panel) growth conditions. The dash lines with matching colors correspond to the sum of the individual defects. For example, the dashed blue line shows the sum of the energies of isolated O_{Te} and isolated V_{Cd} while the solid blue line shows the energy of $O_{Te}-V_{Cd}$ complex.

to the symmetry of O_2 molecule. Therefore, $(O_2)_{Te}-V_{Cd}$ and $(O_2)_{Te}$ are very unlikely to be the cause of the observed v_1 and v_2 .

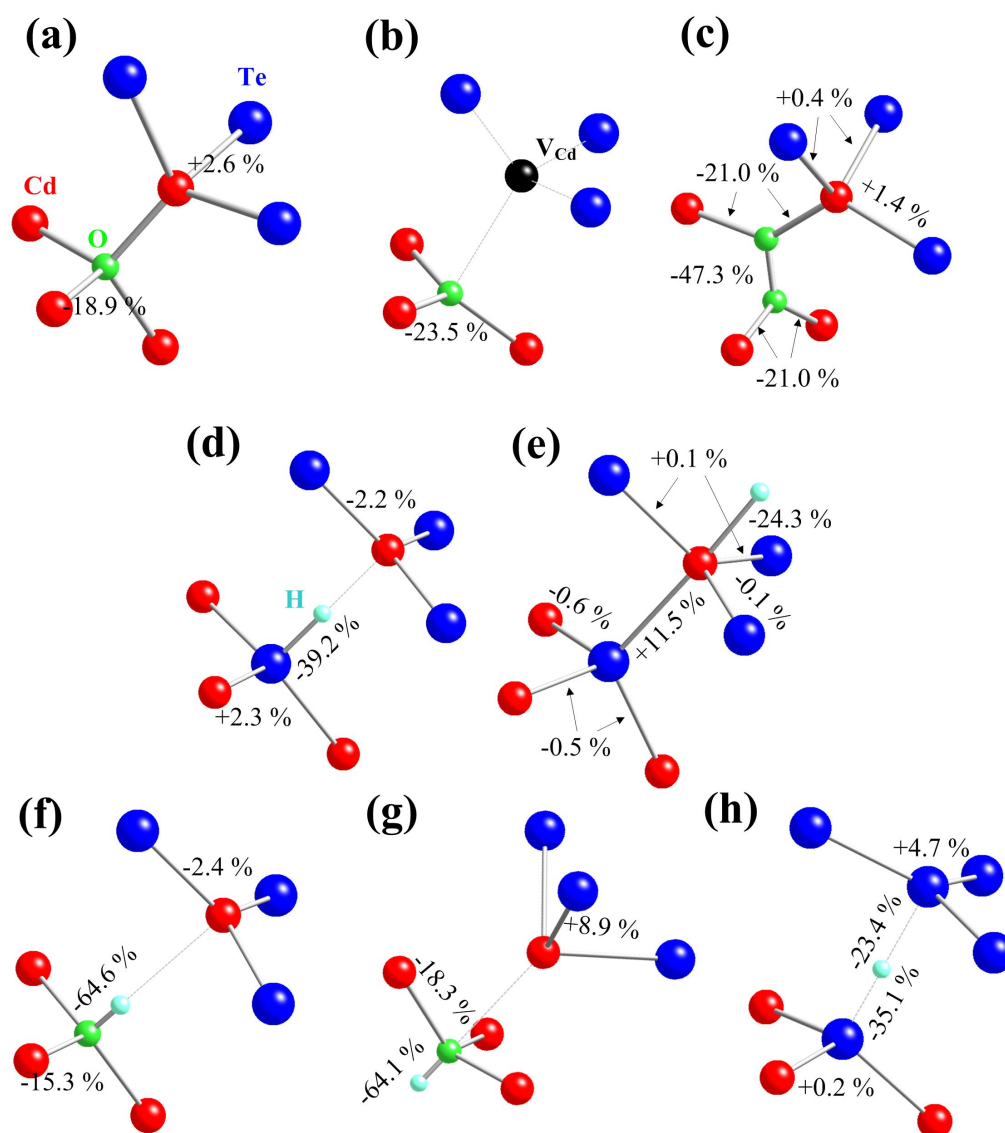


Figure 4.7 The local structure of (a) O_{Te}^0 , (b) $[O_{Te}-V_{Cd}]^{2+}$, (c) $[O_2]_{Te}^0$, (d) H^+ , (e) H^- , (f) $O_{Te}-H^+$ (BC), (g) $O_{Te}-H^-$ (AB), and $Te_{Cd}-H^+$ (BC). The red, blue, green, and light-blue colors are used to label Cd, Te, O, and H atoms, respectively. All bond distances are given as percentage differences from the bulk CdTe bond distance ($d = 2.783\text{\AA}$).

Table 4.1. Formation energies in CdTe with Fermi level at the valence band maximum (VBM).

Defect	Charge q	E_f (eV)		Bond length (Å)
		Cd-rich	Te-rich	
V_{Cd}	2-	1.81	1.05	
V_{Te}	2+	0.50	1.26	
Cd_{Te}	2+	0.61	2.13	
Te_{Cd}	2+	1.86	0.33	
Cd_i	2+	-0.66	0.10	
Te_i	2+	1.58	0.82	
O_{Te}	0	0.89	0.72	
$O_{Te}-V_{Cd}$	2-	2.60	1.68	
$[O_2]_{Te}$	0	3.39	2.31	
$[O_2]_{Te}-V_{Cd}$	2-	5.60	3.75	
H^+ (BC)	1+	0.03	0.03	1.69
H^- (AB)	1-	1.67	1.67	1.81
$O_{Te}-H^+$ (BC)	1+	-0.15	-0.31	0.99
$O_{Te}-H^-$ (AB)	1-	1.36	1.20	0.98
$Te_{Cd}-H^+$	1+	1.96	0.43	0.99
$2H-Te_{Cd}$ (BC)	0	2.60	1.08	1.82 1.82
$2H-Te_{Cd}$ (AB)	0	2.50	0.97	1.87 1.71

Table 4.2. The calculated and experimental frequencies of the oxygen and hydrogen defects in CdTe.

Defect (AB) _O	Charge q	d _{A-B} (Å)	ω (calculated) (cm ⁻¹)	ω (exp.) (cm ⁻¹)
O _{Te}	0	-	338	349.8 ^a
O _{Te} -V _{Cd}	2-	-	467 ⊥ \hat{c} 197 \hat{c}	
(O ₂) _{Te}	0	1.27	901 ^{stretch}	
(O ₂) _{Te} -V _{Cd}	0	1.26	917 ^{stretch}	
free O ₂	0	1.22	1485	1580.2 ^a
H ⁺ (AB)	1+	1.68	1934 ^{stretch} 291 ^{wag}	1108.4 ^b 1097.8 ^b
H ⁺ (BC)	1+	1.69	1852 ^{stretch} 304 ^{wag}	
H ⁻ (AB)	1-		810 ^{stretch} 646 ^{wag}	
O _{Te} -H ⁺ (AB)	1+	0.99	3466 ^{stretch} 721 ^{wag}	
O _{Te} -H ⁺ (BC)	1+	0.98	3574 ^{stretch} 638 ^{wag}	
Te _{Cd} -H ⁺ (BC)	1+	1.81	1099 ^{stretch} 641 ^{wag}	
2H-Te _{Cd} (BC)	0	1.82 1.82	996, 1273 ^{stretch} 653, 676, 422, 669 ^{wag}	
2H-Te _{Cd} (AB)	0	1.87 1.71	944, 1744 ^{stretch} 701, 395, 680 ^{wag}	

^a(Huber and Herzberg, 1979). ^b(Chen *et al.*, 2006).

4.5.3 Hydrogen and oxygen defects in CdTe

Because O defects do not explain the ν_1 and ν_2 modes observed by Chen *et al.* (Chen *et al.*, 2006; Chen *et al.*, 2007), we further explored others common impurities that can give LVM in the 1000 cm^{-1} region. The high frequency limits the possibility to light impurities and H is the top candidate, especially, the frequency of metal-H bonds are usually in the 1000 cm^{-1} region. H is also known to be the common unintentional defect in most semiconductors. It can be easily incorporated during crystal growth and play an important role in many semiconductors. Therefore, the hydrogen-oxygen defect complexes in CdTe are studied. Based on its behavior in other similar semiconductors, hydrogen should incorporate into CdTe at interstitial sites that are either at an anti-bonding center (AB) site or at a bonding center (BC) site (see Figure 4.7 d and e). The formation energies of interstitial H are shown in Table 4.1 with the plot of formation energies vs Fermi energy in Figure 4.6. We found that the formation energy of H^+ at the BC site is lower than the AB site by about 0.2 eV. Therefore, the H^+ should be at BC site as shown in Figure 4.7 d. On the other hand, H prefers to bind with Cd at the AB site than the BC site (see Figure 4.7 e). Hydrogen is amphoteric in CdTe with the donor/acceptor transition energy at 0.82 eV.

The H^+ and H^- have two LVM frequencies each; the wag mode and the stretch mode. Their values are shown in Table 4.2. For H^+ , the wag frequencies are $\sim 300\text{ cm}^{-1}$ and the stretch frequencies are $\sim 1900\text{ cm}^{-1}$. They are far away from the experimental ν_1 and ν_2 . For H^- , the wag frequency is at 646 cm^{-1} and the stretch frequency is at 810 cm^{-1} . Again, they are far away from ν_1 and ν_2 .

Since O_{Te} exists in CdTe doped with O (this is know because the LVM of O_{Te} is clearly observed), it is likely to trap H, forming a strong O-H bond. We, indeed, found

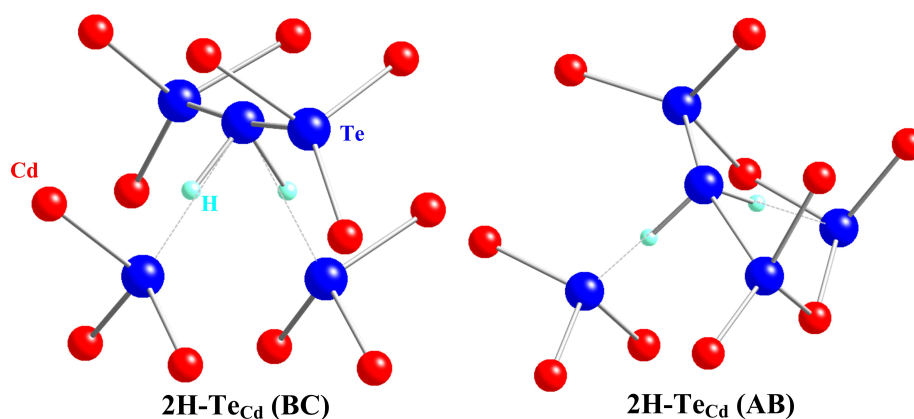


Figure 4.8 The local structure of complexes defects 2H-Te_{Cd} when H atoms are at BC and AB sites.

that the $\text{O}_{\text{Te}}\text{-H}^+$ complex is bound by ~ 1.4 eV. This means the reaction: $\text{O}_{\text{Te}} + \text{H}^+ \rightarrow (\text{O}_{\text{Te}}\text{-H}^+)$ is exothermic by 1.4 eV, i.e. O_{Te} strongly prefers to bind with H.

We found that the formation energy of $\text{O}_{\text{Te}}\text{-H}^+$ (BC) is almost equal to $\text{O}_{\text{Te}}\text{-H}^+$ (AB) within the computational error bar. The formation energy of $\text{O}_{\text{Te}}\text{-H}^-$ (BC) is slightly higher than $\text{O}_{\text{Te}}\text{-H}^-$ (AB) by about 0.1 eV. As a result, $\text{O}_{\text{Te}}\text{-H}$ is amphoteric with the donor/acceptor transition energy at 0.75 eV. The vibrational frequencies of these defects are shown in Table 4.2. Again, the wag modes of $\sim 600 - 700$ cm^{-1} are too low and the stretch modes of ~ 3500 cm^{-1} are too high to explain ν_1 and ν_2 .

We have also investigated the complexes defect of hydrogen with the antisite defect, i.e. H-Te_{Cd} . Because the energy of Te_{Cd} is quite low in Te-rich growth condition, the defect is likely to exist. The formation energy of complexes defect $\text{Te}_{\text{Cd}}\text{-H}^+$ is found to be reasonably low in Te-rich growth condition. The binding energy of this complexes defect with respect to the Fermi energy is shown in Figure 4.9. When the Fermi level is near midgap, the binding energy of $\text{Te}_{\text{Cd}}\text{-H}^+$ is quite high. Therefore, we expected that an additional hydrogen can bind with $\text{Te}_{\text{Cd}}\text{-H}^+$ to form

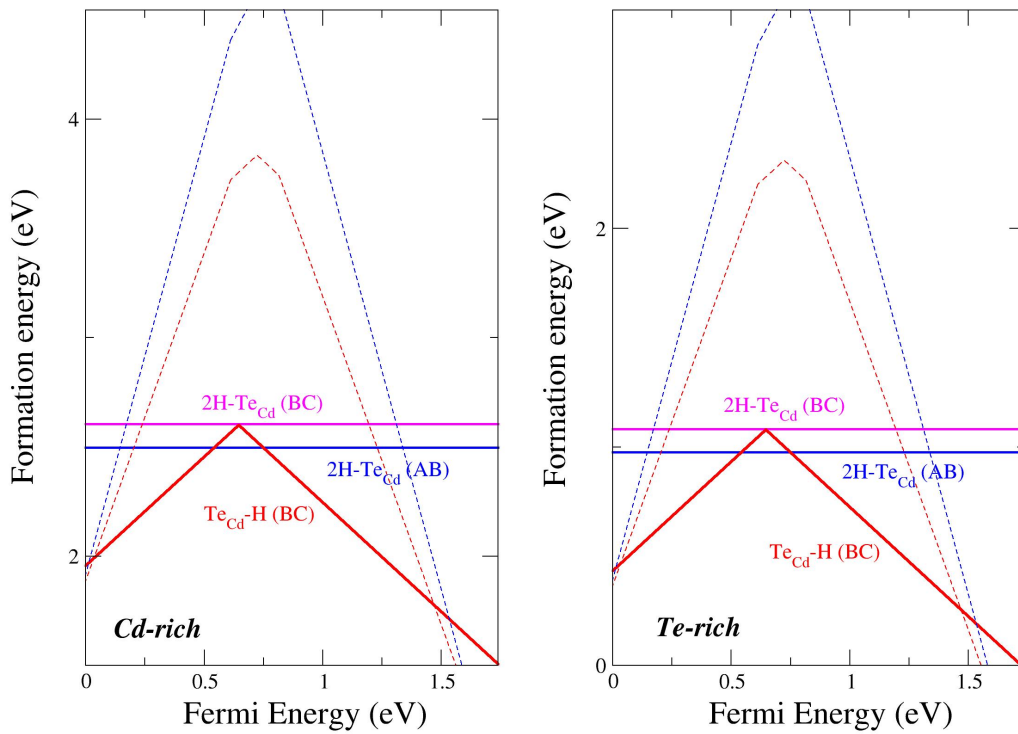


Figure 4.9 Defect formation energies of 2H-Te_{Cd} plotted as a function of the Fermi level, under the Cd-rich (left panel) and Te-rich (right-panel) growth conditions, respectively. The dash lines correspond to the sum of the individual defects (i.e., $\text{Te}_{\text{Cd}} + \text{H}$ and $\text{Te}_{\text{Cd}} + \text{H} + \text{H}$).

2H-Te_{Cd} . The 2H-Te_{Cd} complexes defect has been studied and the local structure of this defect is shown in Figure 4.8. The formation energy of 2H-Te_{Cd} at AB site is slightly lower than at BC site ~ 0.1 eV and the binding energies of these defects are still quite high at middle gap as illustrated in Figure 4.9. The calculated LVMS frequencies of $\text{Te}_{\text{Cd}}\text{-H}^+$ and 2H-Te_{Cd} are also shown in Table 4.2. We found that the frequencies in stretch modes are reasonably close to the observed ν_1 and ν_2 .

Our calculations suggested that the ν_1 and ν_2 observed by Chen *et al.* (Chen *et al.*, 2006; Chen *et al.*, 2007) may come from the hydrogen related defects with a strong H

bond. Possible candidates include $\text{Te}_{\text{Cd}}\text{-H}^+$, 2H-Te_{Cd} at AB and BC sites. These complexes defects give vibrational frequencies in a reasonable agreement with the observed values. In addition, their formation energies are reasonable.

4.6 Conclusion

The formation energies and LVM frequencies of several O and H point defects in CdTe are calculated. We found that the calculated LVM of O_{Te} is in full agreement with the experimental value. (Chen *et al.*, 2006; Chen *et al.*, 2007) However, the LVMs of $\text{O}_{\text{Te}}\text{-V}_{\text{Cd}}$ complexes are far from the high frequency modes ν_1 and ν_2 observed in certain samples. (Chen *et al.*, 2006; Chen *et al.*, 2007) This indicates that Chen *et al.* proposed a wrong model in their paper. We showed that $\text{Te}_{\text{Cd}}\text{-H}^+$, 2H-Te_{Cd} at AB and BC sites have frequencies close to the observed ν_1 and ν_2 . These H defects could be the sources of their observed ν_1 and ν_2 .

4.7 References

- Chen, G., Miotkowski, I., Rodriguez, S., and Ramdas, A. K. (2006). Stoichiometry Driven Impurity Configurations in Compound Semiconductors. **Phys. Rev. Lett.** 96: 035508.
- Chen, G., Miotkowski, I., Rodriguez, S., and Ramdas, A. K. (2007). Control of defect structure in compound semiconductors with stoichiometry: Oxygen in CdTe. **Phys. Rev. B** 75: 125204.
- Feynman, R. P. (1939). Forces in Molecules. **Phys. Rev.** 56: 340.
- Huber, K. P. and Herzberg, G. (1979). Molecular Spectra and Molecular Structure. IV. Constants of Diatomic Molecules. **Van Nostrand Reinhold Co.**

- Kresse, G. and Furthmüller, J. (1996). Efficiency of ab-initio total energy calculations for metals and semiconductors using a plane-wave basis set. **Comput. Mat. Sci.** 6: 15.
- Landau, L. D. and Lifshits, E. M. (1977). **Quantum Mechanics 3rd ed.** Oxford: Pergamon.
- Limpijumng, S., Li, X., Wei, S.-H., and Zhang, S. B. (2005). Substitutional diatomic molecules NO, NC, CO, N₂, and O₂: Their vibrational frequencies and effect on *p* doping of ZnO. **Appl. Phys. Lett.** 86: 211910.
- Limpijumng, S., Northrup, J. E., and Van de Walle, C. G. (2003). Identification of hydrogen configurations in *p*-type GaN through first-principles calculations of vibrational frequencies. **Phys. Rev. B** 68: 075206.
- Monkhorst, H. J. and Pack, J. D. (1976). Special points for Brillouin-zone integrations. **Phys. Rev. B** 13: 5188.
- Northrup, J. E. and Zhang, S. B. (1994). Energetics of the As vacancy in GaAs: The stability of the 3+ charge state. **Phys. Rev. B** 50: 4962.
- Teweldeberhan, A. M. and Fahy, S. (2005). Calculated pressure dependence of the localized vibrational mode of nitrogen in GaN_xAs_{1-x}. **Phys. Rev. B** 72: 195203.
- Vanderbilt, D. (1990). Soft self-consistent pseudopotentials in a generalized eigenvalue formalism. **Phys. Rev. B** 41: 7892.
- Wei, S.-H. and Zhang, S. B. (2002). Chemical trends of defect formation and doping limit in II-VI semiconductors: The case of CdTe. **Phys. Rev. B** 66: 155211.
- Zhang, L., T-Thienprasert, J., Du, M. H., Singh, D. J., and Limpijumng, S. (2009). Comment on "Spectroscopic Signatures of Novel Oxygen-Defect Complexes in Stoichiometrically Controlled CdSe". **Phys. Rev. Lett.** 102: 209601.

Zhang, S. B. and Northrup, J. E. (1991). Chemical potential dependence of defect formation energies in GaAs: Application to Ga self-diffusion. **Phys. Rev. Lett.** 67: 2339.

Zhang, S. B., Wei, S. H., and Zunger, A. (2001). Intrinsic *n*-type versus *p*-type doping asymmetry and the defect physics of ZnO. **Phys. Rev. B** 63: 075205.

CHAPTER V

LOCAL STRUCTURE OF INDIUM OXYNITRIDE

5.1 Introduction

Indium oxynitride can be considered as an alloy between indium nitride (InN) and indium oxide (In_2O_3). This is unlike most of traditional semiconductor alloys in the sense that the crystal structures as well as the anion valencies of the two parent compounds are different. InN is one of the highly studied III-nitride semiconductors (GaN, AlN, and InN) because III-nitride alloys are widely used for optoelectronic applications. Despite real applications and substantial research in III-nitride materials, InN bandgap has been mistaken to be ~ 1.9 eV for a long time (see the discussion in Refs. (Wei *et al.*, 2003; Wu *et al.*, 2004)). Only recently that a high quality InN can be obtained by molecular beam epitaxy (MBE) and the actual InN bandgap of ~ 0.7 eV has been realized (Davydov *et al.*, 2002; Wu *et al.*, 2002). The apparently large bandgap observed in the past is most likely due to the Moss-Burstein shift caused by substantial unintentional carriers that are typical for InN grown by traditional techniques (dc discharge or sputtering) (Davydov *et al.*, 2002; Wu *et al.*, 2002; Bhuiyan *et al.*, 2003; Wu *et al.*, 2004). Because InN has a (now-realized) small bandgap of ~ 0.7 eV and In_2O_3 has a large bandgap of ~ 3.6 eV (Klein, 2000), the band gap of indium oxynitride can potentially be engineered in a very wide range. This combining with the availability of low temperature growth techniques, such as rf

magnetron sputtering (Motlan *et al.*, 2002), makes indium oxynitride a strong candidate for optical coating applications despite its poor crystal quality.

In low O content alloys, it has been reported that O atoms substitute for N in the wurtzite InN crystal structure (Yoshimoto *et al.*, 2003). However, in higher O content alloys the crystal structure remains unclear. Previously, an attempt to study indium oxynitride structures by N *K*-edge XANES has been done (Yi *et al.*, 2005). However, probing local structure of anions in this alloy system is not the most direct way because anions in both InN and In₂O₃ are four-fold coordinated. Unlike anion, the coordination number of In in the two compounds are different, i.e. it is six-fold in In₂O₃ and four-fold in InN (see Figure 5.1). Therefore, probing the local structure of In atoms should give more direct information on the alloy structures. In this work, the In *L*₃-edge XANES is used to characterize indium oxynitride with varied compositions. XANES has been proven to be a powerful tool in resolving the local structures around the absorbing atoms (in this case In atoms) (Ciatto *et al.*, 2005; Fons *et al.*, 2006; Limpijumnong *et al.*, 2007).

5.2 Experimental Method

Indium oxynitride films were grown by rf magnetron sputtering at room temperature using a technique called reactive gas-timing by our collaborators at King Mongkut's Institute of Technology Ladkrabang (KMITL) (Kietipaisalsophon *et al.*, 2002; Sungthong *et al.*, 2008). The growth process started with the pre-evacuation of the chamber to the order of 10⁻⁵ Pa. Then N₂ and O₂ gas were flown interchangeably at the flow rate of 10 standard cm³ per minute (sccm) onto the 99.999% purity In target. The sputtering gas pressures were set at 0.34 Pa and 0.32 Pa for N₂ and O₂,

respectively. By controlling N₂ and O₂ gas timing, indium oxynitride samples with varied O contents were obtained. The interval of gas timing cycles used for each sample is shown in Table 5.1 and the samples are named according to the gas timing cycles. The rf plasma power was set at 100 W and all samples were grown on polyethylene terephthalate substrate to the thickness of ~ 1 μm (typical growth time is approximately 1 hour). To measure the actual O content in each sample, the [O]:[In] ratios were determined using Auger electron spectroscopy (AES) with capability of sputter depth profiling. The O contents were found to be homogeneous throughout the film thickness. The optical bandgaps measured by UV-visible spectroscopy were found to increase with O₂ gas timing ratio as shown in Table 5.1. This is consistent with the work of Yi *et al.* (Yi *et al.*, 2005) that reported the increasing of optical bandgap of indium oxynitride with O content. The AES and UV-visible measurements are also carried out by KMITL team. Although the optical bandgap of N30/O0 sample is larger than that of pure InN and the sample is expected to contain a few percent of unintentionally doped O, this gap widening in low O samples is most likely due to Moss-Burstein effects (Davydov *et al.*, 2002; Wu *et al.*, 2002; Bhuiyan *et al.*, 2003; Wu *et al.*, 2004) not the changes in the crystal structure. As will be discussed, L₃-edge XANES of In is sensitive to the changed in In coordination number but not to the interchanging between N and O. Therefore, XANES of InN with a few percent of N replaced by O are expected to be almost identical to pure InN because it is structurally the same as InN.

All samples were characterized by In L₃-edge XANES measurements in the fluorescent mode with a 13-component Ge detector (Canberra) at the x-ray absorption spectroscopy beamline (BL-8) of the Siam Photon Source (electron energy of 1.2

GeV, beam current 120-80 mA), Synchrotron Light Research Institute, Thailand. Double crystal monochromator Si (111) was used to scan the synchrotron x-ray with the photon energy step of 0.25 eV in the range 3700 to 3850 eV, covering the XANES region of In L_3 -edge.

5.3 Computational Details

In order to understand the local microscopic structure, we performed first principles In L_3 -edge XANES simulations of wurtzite InN, bixbyite In_2O_3 , and alloy of $(\text{InN})_x(\text{InO}_{0.5})_{1-x}$ crystals. The detailed crystal structures were optimized based on first principles pseudo potential calculations. The density functional theory with local density approximation and ultrasoft Vanderbilt pseudo potentials as implemented in the VASP codes (Kresse and Furthmüller, 1996) were used. The cutoff energy for the plane wave basis set was 400 eV. We used Monkhorst-Pack k -point mesh for Brillouin zone integration ($7 \times 7 \times 7$ for 4-atom unit cell wurtzite-InN, $2 \times 2 \times 2$ for 72-atom supercell alloy of wurtzite- $\text{InN}_x\text{O}_{1-x}$, and $3 \times 3 \times 3$ for 40-atom unit cell bixbyite- In_2O_3). All atoms were allowed to relax until the residue forces were less than 10^{-3} eV/Å. The fully relaxed local structures surrounding In atoms are shown in Figure 5.1 for InN, In_2O_3 , and $\text{InN}_x\text{O}_{1-x}$ alloy, respectively. All In atoms in wurtzite InN crystal are equivalent. However, there are two species of In atoms in In_2O_3 ; labeled In1 and In2, with the composition ratio of 1:3. For the alloys, a few different local structures surrounding In atom have been tested. First, in wurtzite InN, we replaced all four N atoms surrounding an In atom with O atoms. This is to see the effect of neighboring specie. Second, one anion is replaced (N by O or vice versa) for both InN and In_2O_3 structures. The structural relaxations by first principles calculations are a crucial step

to obtain the computationally unstrained structures to be further used in electronic structure and XANES calculations.

Since the electronic transition associated with the XANES measurement must follow the dipole selection rule, K and L_3 edges correspond to the p - and $(s+d)$ -partial density of state (PDOS), respectively. Therefore, PDOS has frequently been used to compare with the XANES measurement. An x-ray absorbance $\mu(\omega)$ is given by the Fermi's golden rule

$$\mu \propto \sum_f |\langle f | D | i \rangle|^2 \delta(E_i - E_f + \omega), \quad (5.1)$$

where $|i\rangle$, $|f\rangle$, E_i , and E_f are the initial and final states and their energies, respectively. ω and D are the photon frequency and dipole operator. This Fermi's golden rule limits the transition of the core electron to only the symmetry-allowed states.

To calculate *ab initio* XANES of InN, In₂O₃, and InN_xO_{1-x} alloy based on the relaxed crystal structures mentioned, we used the FEFF8.2 codes (Ankudinov *et al.*, 1998; Ankudinov *et al.*, 2002). The codes utilize a full multiple scattering approach based on *ab initio* overlapping muffin-tin potentials. The muffin-tin potentials were obtained using self-consistent calculations with Hedin-Lundqvist exchange-correlation function. The self-consistent calculations were performed in the sphere radius of 4 Å (~ 40 atoms) around the absorber In atom, which is more than sufficient to allow charge to fluctuate yielding realistic electron relaxations. The full multiple scattering calculations include all possible paths within a larger cluster radius of 7.4 Å (~ 140 atoms). Note that we used the default values for most of the parameters in the FEFF calculations.

Table 5.1. The growth conditions and N:O ratios of each sample and the optical bandgap of the samples grown under the equivalent conditions (Sungthong *et al.*, 2008).

Sample	Gas Timing (sec)		Optical Bandgap (eV)	[O]:[In] Composition
	N ₂	O ₂		
N30/O0	30	0	1.5	0.16
N30/O5	30	5	1.6	0.43
N30/O10	30	10	1.6	0.96
N30/O20	30	20	2.4	1.08
N0/O30	0	30	3.4	1.50

5.4 Results and Discussion

5.4.1 Electronic structures of InN, In₂O₃, and InN_{1-x}O_x alloy

At present, it is realized that wurtzite InN has a direct band gap of 0.7 eV. The unit cell of InN is composed of 4-atom with the calculated lattice constant a of 3.511 Å and $c/a \sim 1.60$ Å. The calculated bandgap of InN using first-principles calculations is slightly negative (see Figure 5.2). The lower part of the valence band (VB) (-11 to -7 eV) is mainly composed of N 2s, and the higher bands located at around -3 to 4 eV are derived from the hybridization of N 2p, In 5s, and In 5p. In the conduction band (CB), the bands located at 5 to 16 eV are derived from the mixing of N 2p, In 5s, and In 5p, and the higher bands are mainly In 4d.

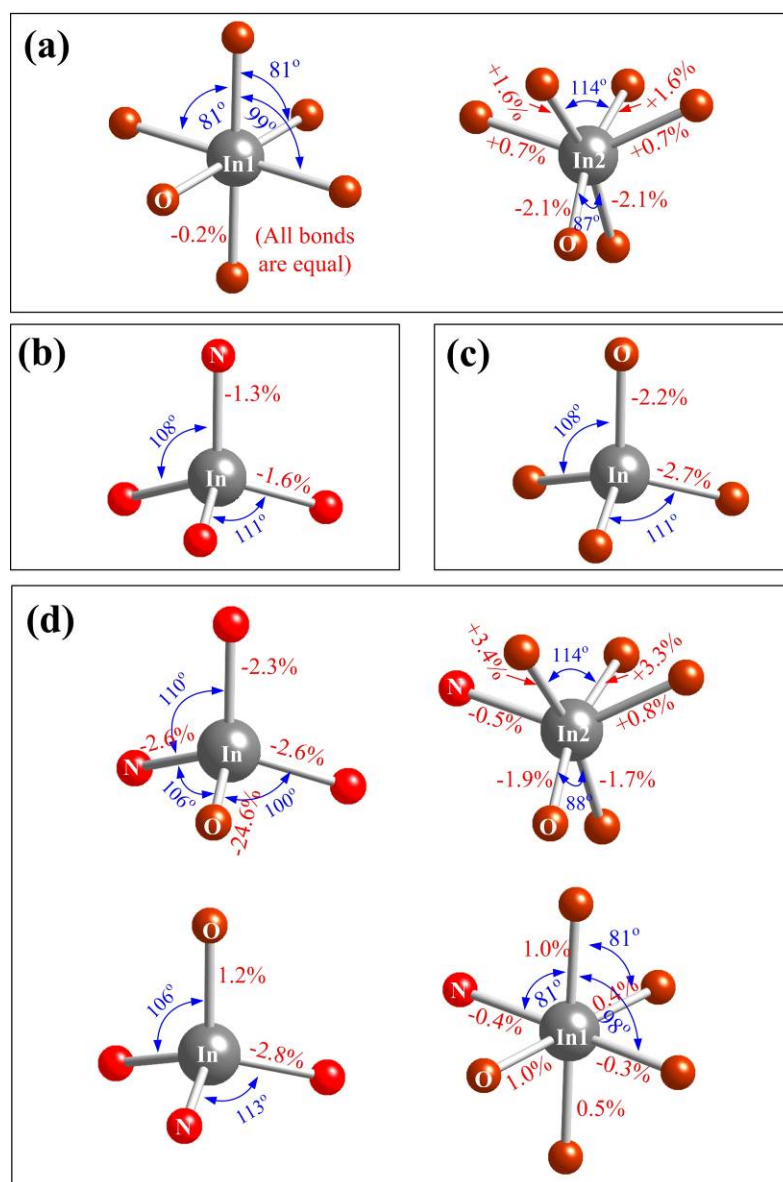


Figure 5.1 The local structure around In atoms used in the simulations of the In L_3 -edge XANES of (a) In_2O_3 , (b) InN , (c) replacing four nitrogen nearest neighbor (NN) of In with four oxygen in wurtzite- InN , and (d) replacing one nitrogen NN of In with oxygen and one oxygen NN of In with nitrogen for InN and In_2O_3 , respectively. All bond distances are given as a percentage difference from an average In_2O_3 bond distance ($d_{\text{calc}} = 2.170 \text{ \AA}$).

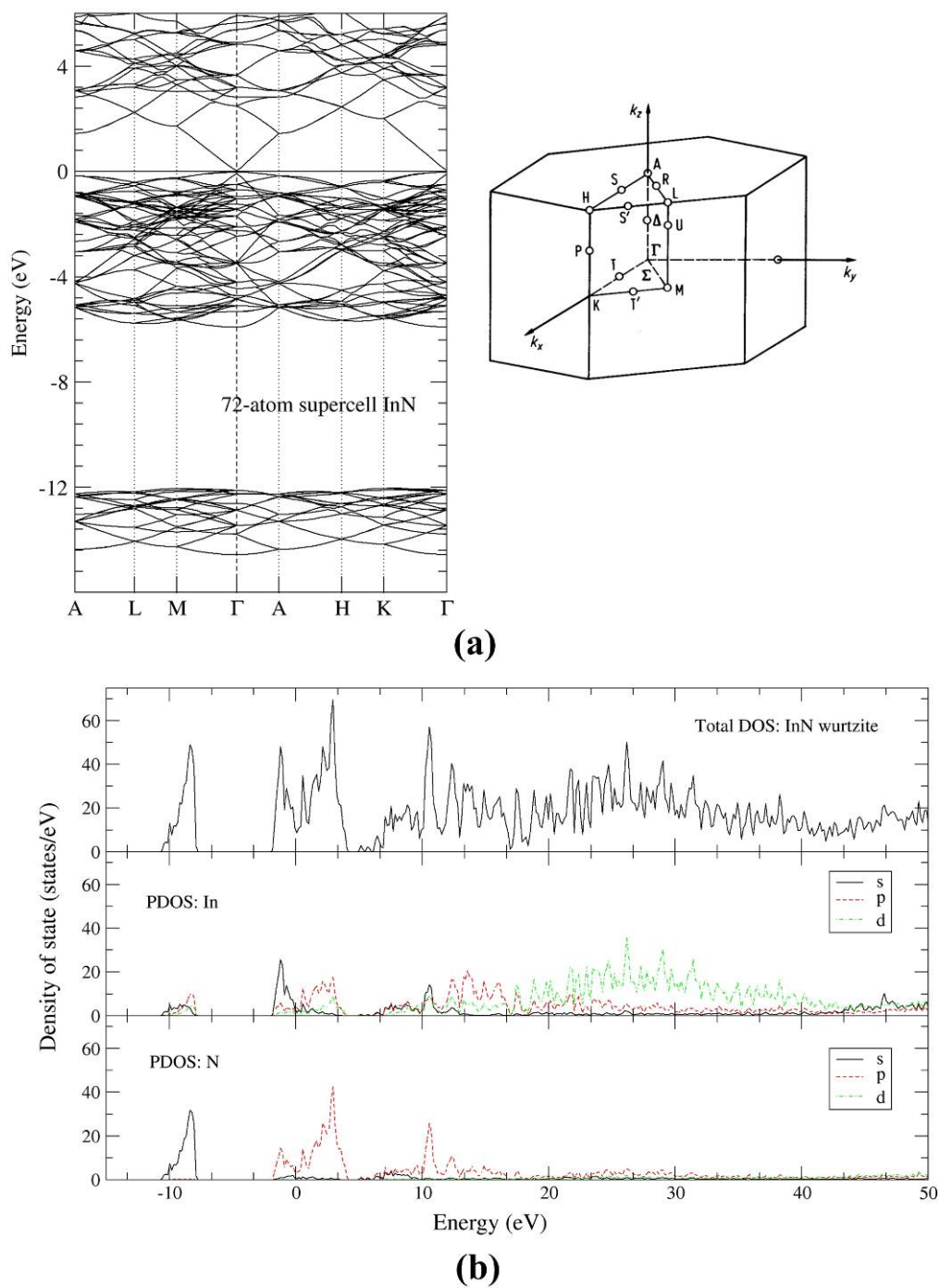


Figure 5.2 (a) Band structures of 72-atom supercell InN. The energy is referenced to the top of the valence band. (b) The calculated total density of state of InN and projected PDOS (s , p , and d states) of In and N atoms.

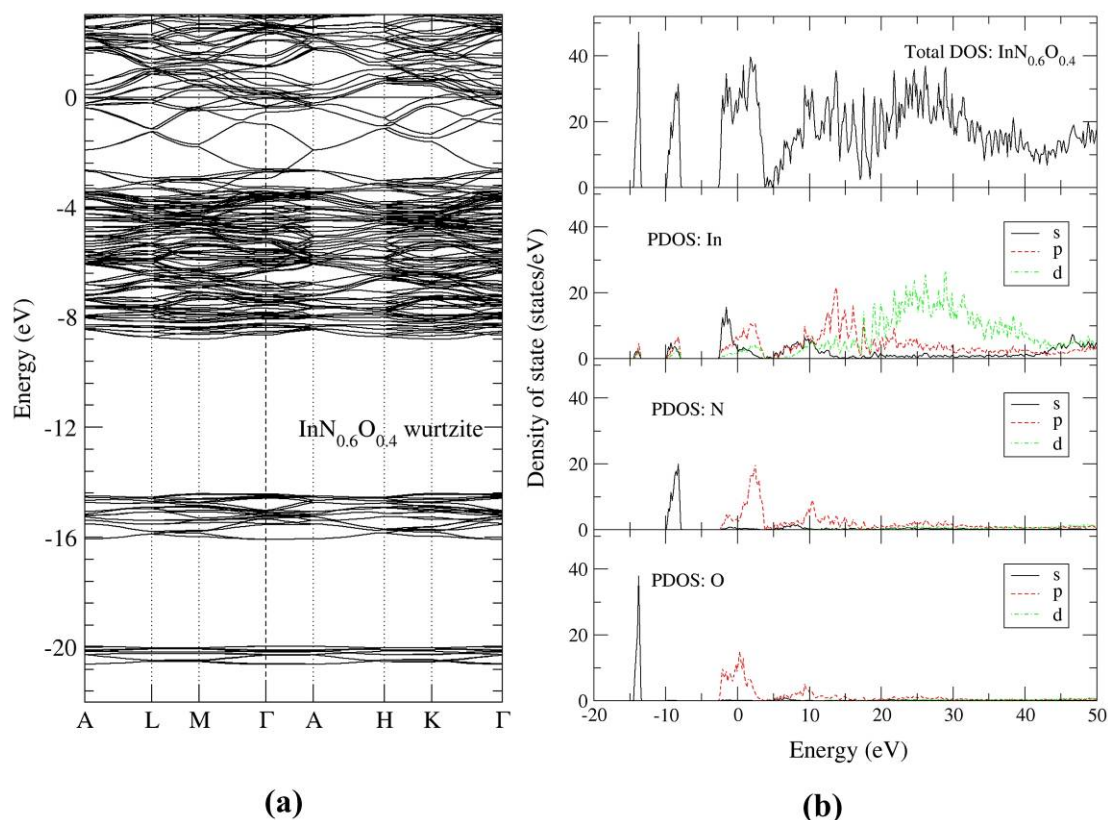


Figure 5.3 (a) Band structures of 72-atom supercell InN_{0.6}O_{0.4} alloy. The energy is referenced to the top of the valence band. (b) The calculated total density of state of InN_{0.6}O_{0.4} alloy and projected PDOS (*s*, *p*, and *d*) of In, N, and O atoms.

For In₂O₃, the natural form is a complicated bixbyite structure. The unit cell is composed of 40-atom with the calculated lattice constant of ~ 10.07 Å. The calculated bandgap of In₂O₃ is 1.26 eV as shown in Figure 5.4. The lower part of the VB (-16 to -10 eV) is mainly derived from O 2*s*. The bands located at around -4 to 4 eV are derived from the mixing of O 2*p* and In 5*s*. The CB are mainly composed of In 5*s*, In 5*p* and In 4*d*.

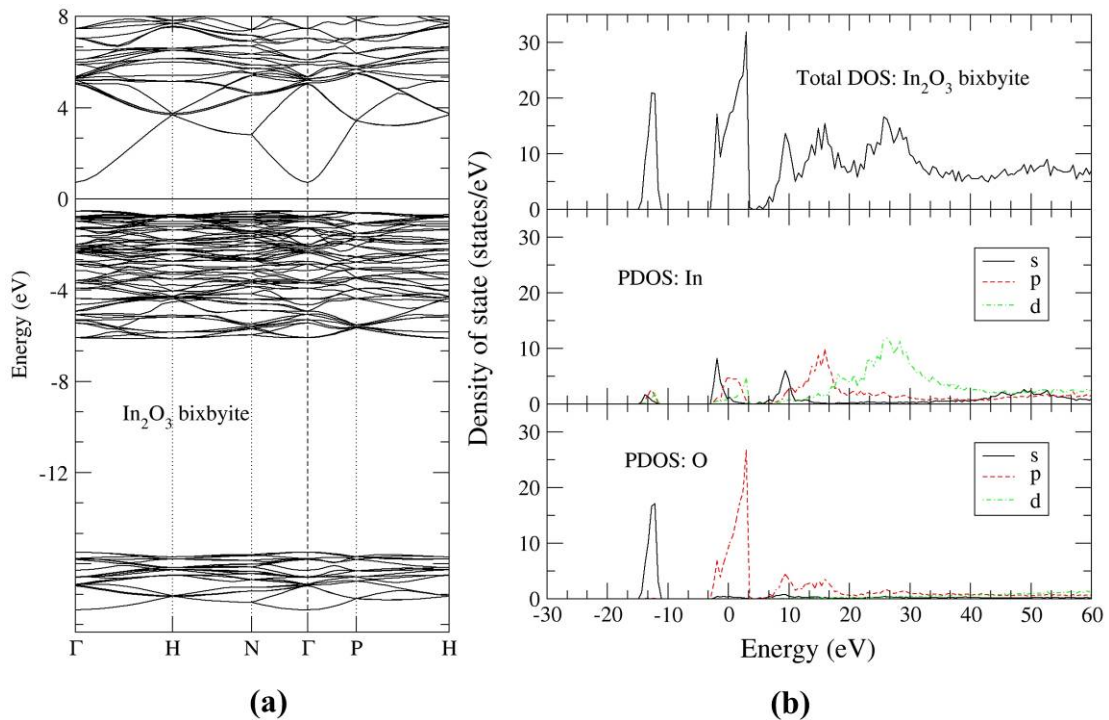


Figure 5.4 (a) Band structures of 40-atom unit cell In_2O_3 . The energy is referenced to the top of the valence band. (b) The calculated total density of state of In_2O_3 and projected PDOS (s , p , and d) of In and O atoms.

The calculated bandgaps of InN and In_2O_3 are lower than experimental values because of the well know DFT problems. However, the states in VB (occupied) and CB (unoccupied) are quite realistic despite incorrect gap values.

The electronic structures of wurtzite- $\text{InN}_{1-x}\text{O}_x$ alloy were calculated to determine the effects of O incorporation in wurtzite-InN. Experimental result suggested that upto 40% O are incorporated into wurtzite InN before the crystal structure of the alloy drastically changed. We used 72-atom supercell wurtzite-InN and randomly replaced 14 (out of 36) nitrogen atoms with oxygen atoms. This gives roughly 40% O contents and the alloy will be refered to as $\text{InN}_{0.6}\text{O}_{0.4}$. The supercell was optimized (relaxed) and used to calculate the band structures and density of states.

$\text{InN}_{0.6}\text{O}_{0.4}$ can be considered a heavy doped semiconductor where parts of the CB are occupied. For the purpose of XANES study; states below the Fermi level is defined as the VB and states above the Fermi level is defined as CB. In Figure 5.3, the lowest band (-15 to -13 eV) is mainly derived from O $2s$, and the next band (-10 to -8 eV) is mainly derived from N $2s$. The band located at around -3 to 4 eV is derived from the mixing of N $2p$, O $2p$, In $5p$, and In $5s$. In the CB, the band is mainly derived from In $5s$, In $5p$, and In $4d$. The shift of Fermi level of $\text{InN}_{0.6}\text{O}_{0.4}$ from the pure wurtzite-InN is about 2.3 eV. This is due to the excess electrons from O that occupy the CB. However, the sited-projected partial density of states of In calculated from InN and $\text{InN}_{0.6}\text{O}_{0.4}$ alloy are quite similar (Figure 5.5). To compare the electronic states obtained from DFT method with the measured or calculated XANES spectra from other methods, we calculated $s + d$ site-projected density of states of In with

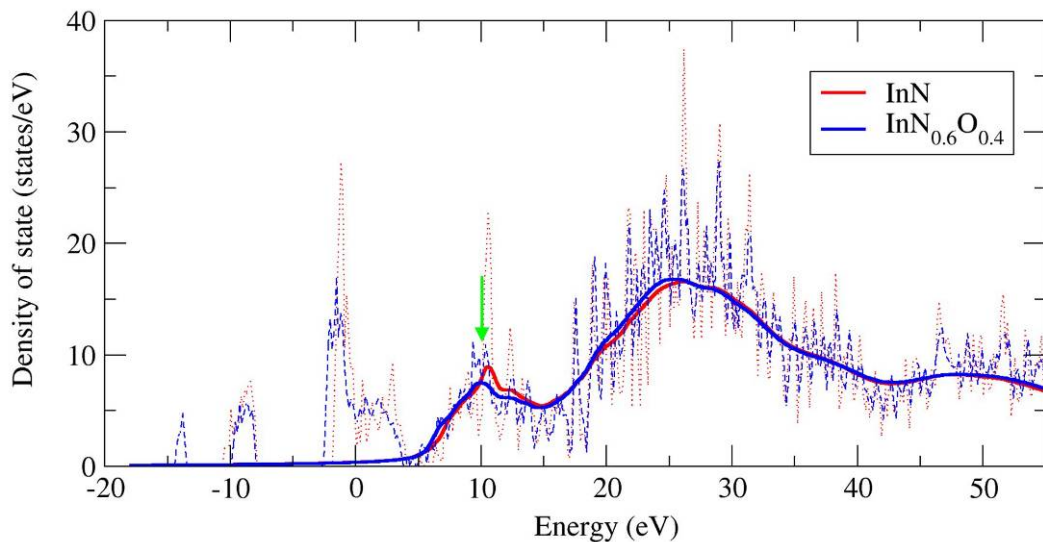


Figure 5.5 The site-projected PDOS ($s+d$) of In in InN and $\text{InN}_{0.6}\text{O}_{0.4}$ alloy in wurtzite structure. The broken lines show the PDOS as calculated. The full lines show the smeared CB ($s+d$) states. All lines are color coded (red: InN; blue: $\text{InN}_{0.6}\text{O}_{0.4}$).

some broadening. The spectra of InN and InN_{0.6}O_{0.4} are shown in Figure 5.5. The main difference between the two simulated spectra is the drop of peak located at around 10 eV (marked by an arrow). This is expected because for InN_{0.6}O_{0.4} alloy parts of the CB are already occupied. These states can not serve as the final state of the absorption. Therefore, we expected that the L_3 -edge spectrum of wurtzite-InN_{0.6}O_{0.4} is still similar to that of pure wurtzite-InN except the drop of peak in the low energy region.

5.4.2 XANES spectra of InN, In₂O₃, and In_{1-x}O_x alloy

The measured L_3 -edge XANES spectra of all five samples and calculated In L_3 -edge spectra using FEFF of InN and In₂O₃ are shown in Figure 5.6 (a) and (b) (bottom and top curves), respectively. For In₂O₃, since there are two species of nonequivalent In atoms, the obtained spectrum is from the weight-averaged between the spectra from two species. Note that the spectra obtained from the two species of In in In₂O₃ are quite similar, as shown in Figure 5.7 (b) (two middle curves). The spectra of four-fold In in InN and six-fold in In₂O₃ are, however, clearly different. Moreover, our calculations show that the XANES spectra of the four-fold (six-fold) In atom is not very sensitive to the substitution of a neighboring N by O (or O by N). In Figure 5.7 (a), the substitutional effects of N in InN by O are illustrated. The bottom curve is the simulated XANES spectrum of InN. The middle and top curves show the spectra when one and all four nitrogen neighbor atoms of the In atom are replaced by O atoms. It is clear that the XANES features are not very sensitive to these anion substitutions.

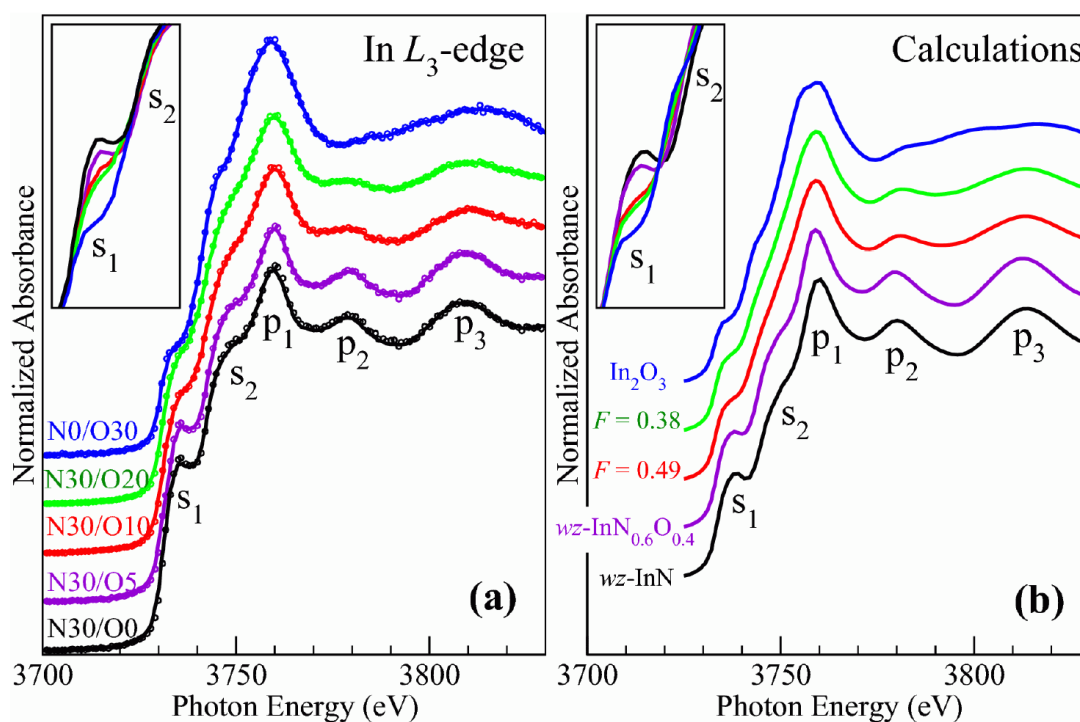


Figure 5.6 (a) Normalized In L_3 -edge XANES spectra of indium oxynitride samples prepared under different gas-timing with increased O₂ timing from bottom curve to top curve. Circles show recorded data points and the curves are the (noise removed) fit to the data. Inset: The plots from the main panel without offset at the energy range near the s₁ shoulders to highlight the changes in the shoulder height. (b) The calculated In L_3 -edge XANES spectra of wurtzite InN, bixbyite In₂O₃, wurtzite InN_{0.6}O_{0.4}, and the simulated separated phase alloys with 38% and 49% four-fold In atoms (see text for detail).

In Figure 5.7 (b), the substitutional effect of O in In₂O₃ by N is illustrated. It is clear that by replacing one oxygen neighbor by nitrogen (top curve) has almost no effect on the shape of the spectrum.

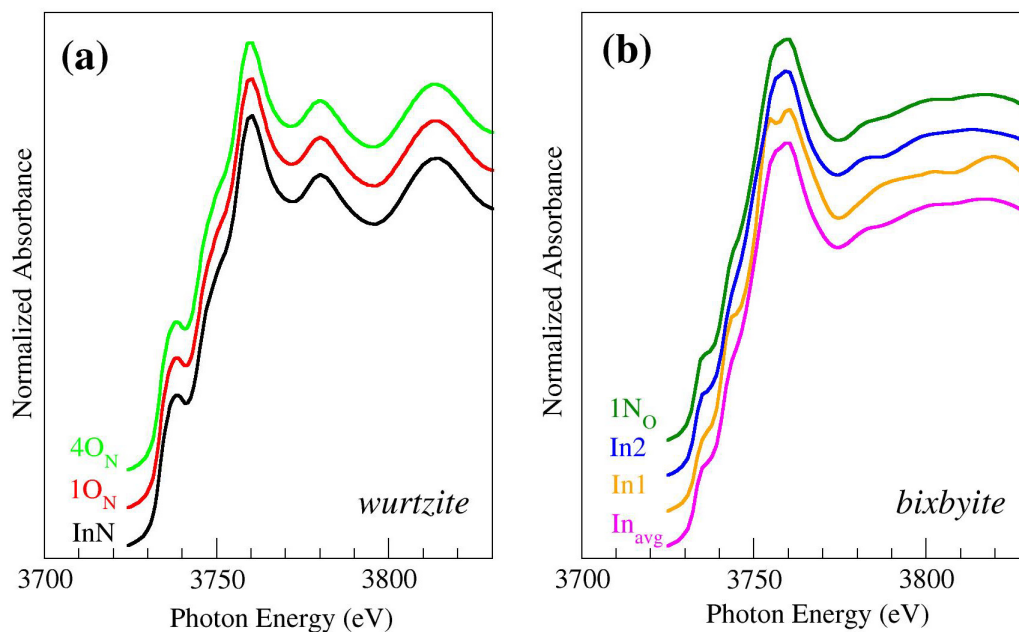


Figure 5.7 (a) The calculated spectra of pure InN and replacing 1 nitrogen NN and 4 nitrogen NN of In with oxygen (as shown in Figure 5.1), and (b) The calculated spectra of In_{avg} , In1, In2, and replacing one oxygen NN with nitrogen.

From Figure 5.6, the calculated spectra of InN and In_2O_3 are in full agreement with the measured spectra from N30/O0 and N0/O30 samples, respectively. The main features of InN XANES spectrum compose of two shoulders and three peaks labeled as s_1 , s_2 , p_1 , p_2 , and p_3 . All five features are in a very good agreement with the corresponding features in the N30/O0 samples in both positions and shapes. Similar agreement can be found between the spectrum of N0/O30 sample and the calculated In_2O_3 spectrum. This suggests that structurally In atoms in N30/O0 are mostly four-fold (as those in InN) and in N0/O30 are mostly six-fold (as those in In_2O_3). If we compare the measured spectra of different O content (from the bottom curve to the top curve of Figure 5.6 (a)), we can see that the five features are progressively evolved as

O content increased. The progressive changes include: (1) the reduction of s_1 peak (for clarity, the same set of spectra without offset is shown in the inset), (2) the broadening and increasing in magnitude of p_1 peak, (3) the reduction of p_2 peak, and (4) the significant broadening accompanied by a slight shift to higher energy of peak p_3 . Interestingly, the spectrum of N30/O5 (at 43% O content) is still almost perfectly overlapped with that of N30/O0 with an exception of s_1 shoulder, which is slightly reduced (see inset of Figure 5.6 (a)). This indicates that most of In atoms in N30/O5 remain four-fold and O atom are substituting on the N sites. We calculated the XANES spectra for $\text{InN}_{0.6}\text{O}_{0.4}$ alloy in wurtzite structure to test our assumption (the second curve from bottom in Figure 5.6 (b)). The calculated spectrum is almost overlapped with that of (calculated) pure InN for the photon energy beyond the s_1 shoulder. Moreover, a small reduction in s_1 shoulder of the N30/O5 spectrum in comparison with that of N30/O0 is nicely reproduced by the $\text{InN}_{0.6}\text{O}_{0.4}$ alloy simulation. The reduction in the s_1 shoulder is caused by the changes in the low conduction band states due to the replacement of N by O atoms as previously discussed. For samples with higher O contents (N30/O10 and N30/O20), the spectra show a mixed signature between that of InN (four-fold) and In_2O_3 (six-fold). The excess O atoms above the substitutional solubility limit (assumed to be ~40%) of InN can either form a phase separated In_2O_3 -like structure or an inclusion of local In_2O_3 -like structure both of which leads to a formation of six-fold In atoms. In this model, the composition in the sample can be written as $(\text{InN}_{0.6}\text{O}_{0.4})_F(\text{InO}_{1.5})_{1-F}$, where F is a fraction of four-fold In atoms out of all In atoms. The value of F can be calculated using a relationship $[\text{O}]:[\text{In}] = 0.4F + 1.5(1 - F)$, where the $[\text{O}]:[\text{In}]$ ratio of each sample was determined from AES and is shown in Table 5.1. This gives the F values

of 0.49 and 0.38 for N30/O20 and N30/O10, respectively. The corresponding spectra, which are calculated using weight averaged between $\text{InN}_{0.6}\text{O}_{0.4}$ and pure In_2O_3 , are shown in Figure 5.6 (b). The spectra show the mixed signature of InN and In_2O_3 that are consistent with the measured spectra of N30/O10 and N30/O20. s_1 shoulder also further decreased from pure InN as more O content is added (insets of Figure 5.6).

In a detailed investigation, the spectra of both N30/O10 and N30/O20 samples appear to be very similar to each other and the s_1 shoulder of N30/O20 is only slightly lower than N30/O10 (see inset of Figure 5.6 (a)). The simulations also show the same trend, i.e. the s_1 shoulder of the spectrum with $F = 0.38$ is just slightly lower than that of $F = 0.49$ (see the inset of Figure 5.6 (b)). However, when observing the decrease of s_1 shoulder in comparison to that of InN, we can see that the simulations ($F = 0.38$ and $F = 0.49$ spectra) give larger drop in the s_1 shoulder in comparison to those of samples N30/O10 and N30/O20. This suggests that N30/O10 and N30/O20 samples may contain more four-fold In atoms, i.e., higher F ratios than those used in the simulations. We found that a simulation with $F \sim 2/3$, i.e. $2/3$ of In atoms are four-fold and $1/3$ of In atoms are six-fold, can provide a better agreement in the s_1 feature with the experiment (not shown).

5.5 Conclusion

In summary, we have performed In L_3 -edge XANES study of indium oxynitride prepared by rf magnetron sputtering with different oxygen contents. The independent first principles XANES calculations of bulk InN and In_2O_3 give unambiguous agreement with the spectra from the samples prepared by using only N_2 and O_2 gas, respectively. Our results suggest that as much as 40% of oxygen can replace N in

four-fold InN structure. The spectra from the samples with higher O contents show that the alloy contains both four-fold and six-fold indium atoms. This implies that either the samples are phase separated or there exist a preferred intermediate crystal structure containing both four-fold and six-fold In atoms. Our calculations also show that the XANES features are not strongly affected by the substitution of N by O or *vice versa*.

5.6 References

- Ankudinov, A. L., Bouldin, C. E., Rehr, J. J., Sims, J., and Hung, H. (2002). Parallel calculation of electron multiple scattering using Lanczos algorithms. **Physical Review B** 65: 104107.
- Ankudinov, A. L., Ravel, B., Rehr, J. J., and Conradson, S. D. (1998). Real-space multiple-scattering calculation and interpretation of x-ray-absorption near-edge structure. **Physical Review B** 58: 7565.
- Bhuiyan, A. G., Sugita, K., Kasashima, K., Hashimoto, A., Yamamoto, A., and Davydov, V. Y. (2003). Single-crystalline InN films with an absorption edge between 0.7 and 2 eV grown using different techniques and evidence of the actual band gap energy. **Applied Physics Letters** 83: 4788.
- Ciatto, G., Boscherini, F., Bonapasta, A. A., Filippone, F., Polimeni, A., and Capizzi, M. (2005). Nitrogen-hydrogen complex in $\text{GaAs}_x\text{N}_{1-x}$ revealed by x-ray absorption spectroscopy. **Physical Review B (Condensed Matter and Materials Physics)** 71: 201301.
- Davydov, V. Y., Klochikhin, A. A., Emtsev, V. V., Ivanov, S. V., Vekshin, V. V., Bechstedt, F., Furthmüller, J., Harima, H., Mudryi, A. V., Hashimoto, A.,

- Yamamoto, A., Aderhold, J., Graul, J., and Haller, E. E. (2002). Band gap of InN and In-rich $\text{In}_x\text{Ga}_{1-x}\text{N}$ alloys ($0.36 < x < 1$). **Phys. Stat. Sol. (B)** 230: r4.
- Davydov, V. Y., Klochikhin, A. A., Seisyan, R. P., Emtsev, V. V., Ivanov, S. V., Bechstedt, F., Furthmüller, J., Harima, H., Mudryi, A. V., Aderhold, J., Semchinova, O., and Graul, J. (2002). Absorption and Emission of Hexagonal InN. Evidence of Narrow Fundamental Band Gap. **Phys. Stat. Sol. (B)** 229: r1.
- Fons, P., Tampo, H., Kolobov, A. V., Ohkubo, M., Niki, S., Tominaga, J., Carboni, R., Boscherini, F., and Friedrich, S. (2006). Direct Observation of Nitrogen Location in Molecular Beam Epitaxy Grown Nitrogen-Doped ZnO. **Physical Review Letters** 96: 045504.
- Kietipaisalsophon, N., Bunjongpru, W., and Nukeaw, J. (2002). Photoreflectance Study of AlN Thin Films Grown by Reactive Gas-Timing RF Magnetron Sputtering. **Int. J. Mod. Phys. B** 16: 4418.
- Klein, A. (2000). Electronic properties of In_2O_3 surfaces. **Applied Physics Letters** 77: 2009.
- Kresse, G. and Furthmüller, J. (1996). Efficiency of ab-initio total energy calculations for metals and semiconductors using a plane-wave basis set. **Comput. Mater. Sci.** 6: 15
- Limpijumnong, S., Rujirawat, S., Boonchun, A., Smith, M. F., and Cherdhirunkorn, B. (2007). Identification of Mn site in $\text{Pb}(\text{Zr,Ti})\text{O}_3$ by synchrotron x-ray absorption near-edge structure: Theory and experiment. **Applied Physics Letters** 90: 103113.

- Motlan, Goldys, E. M., and Tansley, T. L. (2002). Optical and electrical properties of InN grown by radio-frequency reactive sputtering. **J. Crystal Growth** 241: 165.
- Sungthong, A., Porntheeraphat, S., Poyai, A., and Nukeaw, J. (2008). An Extreme Change in Structural and Optical Properties of Indium Oxynitride Deposited by Reactive Gas-Timing RF Magnetron Sputtering. **Appl. Surf. Sci.** (in press, doi:10.1016/j.apsusc.2008.04.038).
- Wei, S.-H., Nie, X., Batyrev, I. G., and Zhang, S. B. (2003). Breakdown of the band-gap-common-cation rule: The origin of the small band gap of InN. **Physical Review B** 67: 165209.
- Wu, J., Walukiewicz, W., Li, S. X., Armitage, R., Ho, J. C., Weber, E. R., Haller, E. E., Lu, H., Schaff, W. J., Barcz, A., and Jakiela, R. (2004). Effects of electron concentration on the optical absorption edge of InN. **Applied Physics Letters** 84: 2805.
- Wu, J., Walukiewicz, W., Shan, W., Yu, K. M., Ager, J. W., Haller, E. E., Lu, H., and Schaff, W. J. (2002). Effects of the narrow band gap on the properties of InN. **Physical Review B** 66: 201403.
- Wu, J., Walukiewicz, W., Yu, K. M., Ager, J. W., Haller, E. E., Lu, H., Schaff, W. J., Saito, Y., and Nanishi, Y. (2002). Unusual properties of the fundamental band gap of InN. **Applied Physics Letters** 80: 3967.
- Yi, Y., Cho, S., Roh, Y., Noh, M., Whang, C.-N., Jeong, K., and Shin, H.-J. (2005). The Instability of Nitrogen Bonds in Oxygen Incorporated InN_{1-x}O_x Films. **Jpn. J. Appl. Phys.** 44: 17.

Yoshimoto, M., Yamamoto, H., Huang, W., Harima, H., Saraie, J., Chayahara, A., and Horino, Y. (2003). Widening of optical bandgap of polycrystalline InN with a few percent incorporation of oxygen. **Applied Physics Letters** 83: 3480.

CHAPTER VI

HYDRATIONS STRUCTURES OF Ca^{2+} AND Cl^- IONS

BY X-RAY ABSORPTION SPECTROSCOPY

6.1 Introduction

Hydration structures of the arrangement of water molecules around many ions are not very well understood. In this chapter, the XAS of two ions, Ca^{2+} and Cl^- , are studied. Since ion is an impurity in water, the local structures of water molecules arranging around ions is consider a type of defect structures. This work has been done in collaboration with a QM/MM chemist (Assoc. Prof. Anan Tongraar) and a team of experimentalists (lead by Dr. Saroj Rujirawat). For completeness of the presentation, all results are shown here. However, the readers should be aware that the contribution of the thesis' author in this work is on the XAS (both XANES and EXAFS) simulation part. The material in this chapter will be submitted for publication in the near future.

Behavior of ions solvated in polar solvents, in particular water, has long been a topic of scientific interest in order to understand the role of these ions in chemical and biological processes (Frank, 1956; Williams, 1971). Such detailed knowledge can be obtained from a variety of experimental and theoretical techniques. In experiments, powerful techniques from the structural viewpoint are neutron and X-ray diffraction because they offer a direct probe of ionic structure (Enderby and Neilson, 1981; Magini, 1988; Neilson, 1988; Skipper *et al.*, 1989; Neilson and Tromp, 1991; Ohtaki and Radnai, 1993; Howell and Neilson, 1996). However, especially for multi-

component systems, discrepancies in the established data exist, even for fundamental properties as the mean ion-oxygen nearest-neighbor distance and the average number of coordinating solvent molecules. The general reason could be attributed to the lack of direct information relating to static and dynamics properties of the solvent molecules surrounding the ions.

Besides the diffraction techniques, X-ray absorption spectroscopy (XAS) is a powerful tool for an accurate determination of ion hydration structure, due to its element-specific. In addition, since most of the diffraction techniques restrict their use only for relatively high concentrations, the XAS technique can be applied to a wider range of concentrated solutions. XAS spectra can be divided into the X-ray absorption near-edge structure (XANES) region and the X-ray absorption fine structure (EXAFS) region, as explained in Chapter III. In general, the EXAFS spectra can provide a good resolution in detecting near-neighbor solvent environment, especially for systems with a high degree of local order, while the XANES spectra correspond to the geometrical arrangement of the solvated ions. For relatively large disordered systems, like aqueous ionic solutions, however, the presence of multiple scattering (MS) effects (Crozier *et al.*, 1988; D'Angelo *et al.*, 1994) in the spectra as well as the errors from asymmetric distributions (Crozier, 1995; Crozier, 1997) are of major problems in the analysis of XAS data. To simplify the process of XAS data interpretation, the use of information derived from other sources, in particular molecular simulations, is of special interest.

Molecular simulations, in particular molecular dynamics (MD) technique, have been employed to generate partial pair distributions, $g(R)$'s, from which a model $\chi(k)$ is constructed and then used as starting model in the analysis of XAS data. In this

respect, the accuracy in the XAS data analysis depends crucially on the reliability of the simulation results. The combined XAS measurements, in particular EXAFS, and MD simulations technique has successfully been applied to several aqueous and non-aqueous ionic solutions, providing more comprehensive understanding on the structure of ions that solvated in solutions (D'Angelo *et al.*, 1995; Di Cicco, 1996; Di Cicco *et al.*, 1996; Crozier, 1997; Kuzmin *et al.*, 1997; Wallen *et al.*, 1998; D'Angelo and Pavel, 1999; Rossano *et al.*, 1999; Di Cicco *et al.*, 2000; Fulton *et al.*, 2000; D'Angelo and Pavel, 2001; Trapananti *et al.*, 2002; Dang *et al.*, 2006). In terms of molecular simulations, however, most of the previous works had relied on molecular mechanical (MM) force fields, in which the potential functions describing the ion-water and water-water interactions are mostly constructed with respect to a set of experimental data or to *ab initio* calculations. For strong interacting systems, like aqueous ionic solutions, however, it has been demonstrated that “quantum effects” are significant and that the inclusion of these effects in the simulations is mandatory (Rode *et al.*, 2004; Rode *et al.*, 2005). Nowadays, a high-level quantum mechanics/molecular mechanics (QM/MM) MD technique has been shown to be an elegant approach for studying condensed-phase systems, in particular the aqueous ionic solutions (Kerdcharoen *et al.*, 1996; Tongraar *et al.*, 1997; Tongraar *et al.*, 1998; Schwenk *et al.*, 2001; Tongraar *et al.*, 2002; Tongraar and Rode, 2003; Rode *et al.*, 2004; Intharathep *et al.*, 2005; Rode *et al.*, 2005; Tongraar and Rode, 2005; Xenides *et al.*, 2005). With regard to the QM/MM MD technique, the most interesting region, a sphere which includes the ion and its surrounding solvent molecules, is treated quantum mechanically. By this scheme, the complicated many-body contributions as well as the polarization effects, which are hardly accessible through the basic

assumptions underlying the MM potentials, can be reliably included into the defined QM region.

In the present work, a combination of XAS (EXAFS and XANES) measurements and QM/MM MD simulations was employed to study the hydration shell structure of Ca^{2+} and Cl^- . For Ca^{2+} , established results in the literature, both experimental and theoretical investigations, reveal a rather inhomogeneous picture of this hydrated ion. X-ray diffraction experiments on calcium halide aqueous solutions reported hydration numbers between 6 and 8 (Licheri *et al.*, 1976; Cummings *et al.*, 1980; Hewish *et al.*, 1982; Probst *et al.*, 1985; Smirnov *et al.*, 1997; Spangberg *et al.*, 2000; Jalilevand *et al.*, 2001), whereas neutron diffractions yielded larger deviated values, ranging from 5.5 to 10 (Cummings *et al.*, 1980; Hewish *et al.*, 1982). Although the observed difference in these experimental data is considered mainly as a consequence of concentration dependence, the uncertainty in the coordination number exist even at similar concentrated solutions (Cummings *et al.*, 1980; Hewish *et al.*, 1982; Smirnov *et al.*, 1997). Recent EXAFS measurements indicated that this ion has coordination numbers between 7 and 8 (Spangberg *et al.*, 2000; Fulton *et al.*, 2003; Dang *et al.*, 2006). Computer simulations also provided large deviation in the coordination numbers, ranging from 6 to 10 (Probst *et al.*, 1985; Pálincás and Heinzinger, 1986; Floris *et al.*, 1994; Kalko *et al.*, 1996; Kerdcharoen *et al.*, 1996; Obst and Bradaczek, 1996). This observed discrepancy could be attributed strongly to the different theoretical models, *i.e.*, the potential functions, employed in the simulations. In the case of Cl^- , the interactions of this ion with its surrounding water molecules are generally weaker than that of Ca^{2+} and energetically comparable with water-water interactions in bulk water. This makes the structural determination of the Cl^- hydrate

becomes more difficult. Consequently, the uncertainty in the coordination number of Cl⁻ in water is found both in experimental and theoretical studies, varying from 4 to 9 (Neilson and Tromp, 1991; Ohtaki and Radnai, 1993) and from 5.1 to 8.4 (Clementi *et al.*, 1976; Mezei and Beveridge, 1981; Impey *et al.*, 1983; Chandrasekhar *et al.*, 1984; Heinzinger, 1985; Smith and Dang, 1994; Koneshan *et al.*, 1998; Ignaczak *et al.*, 1999; Tongraar and Rode, 2003), respectively.

6.2 Experimental Details

The experimental Ca and Cl *K*-edge XAS spectra of 2.0 M aqueous CaCl₂ solution were measured at beamline 8 of Synchrotron Light Research Institute (SLRI) in Nakhon Ratchasima, Thailand. (see Figure 6.1) All EXAFS and XANES spectra were recorded in transmission mode using ionization chambers as detectors. All XAS

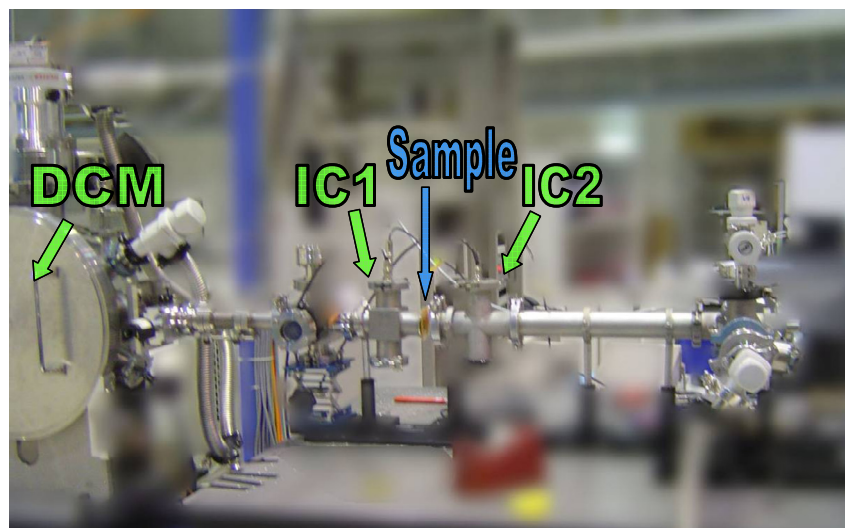


Figure 6.1 The x-ray absorption instrument at beamline 8 (BL-8) of Siam Photon Source (electron energy of 1.2 GeV, beam current 120-80 mA), Synchrotron Light Research Institute, Thailand.

spectra were collected at ambient temperature and atmospheric pressure. Double crystal monochromator Si(111) was used to scan the x-ray energy with the photon energy step of 0.25 eV in the energy range of 3,890-4,440 and 2,720-3,200 eV which cover the EXAFS region for Ca and Cl *K*-edge, respectively. The SLRI storage ring was running at energy of 1.2 GeV with electron currents between 120-80 mA. The solutions were kept in cells with Kapton film windows and Teflon spacers of 0.25 mm. All structural factors $\chi(k)$ were weighted by k^2 and windowed between $2.0 < k < 8.0 \text{ \AA}^{-1}$ using a Hanning window (Hay and Wadt, 1985; Rehr *et al.*, 1992; Newville *et al.*, 1995) $W(k)$ with $dk = 1.0 \text{ \AA}^{-1}$.

6.3 Computational Details

6.3.1 QM/MM MD simulations

By the QM/MM MD technique (Kerdcharoen *et al.*, 1996; Tongraar *et al.*, 1997; Tongraar *et al.*, 1998; Schwenk *et al.*, 2001; Tongraar *et al.*, 2002; Tongraar and Rode, 2003; Rode *et al.*, 2004; Intharathep *et al.*, 2005; Rode *et al.*, 2005; Tongraar and Rode, 2005; Xenides *et al.*, 2005), the system is divided into two parts, namely QM and MM regions. The total interaction energy of the system is defined as

$$E_{total} = \langle \Psi_{QM} | \hat{H} | \Psi_{QM} \rangle + E_{MM} + E_{QM-MM}, \quad (6.1)$$

where $\langle \Psi_{QM} | \hat{H} | \Psi_{QM} \rangle$ refers to the interactions within the QM region, while E_{MM} and E_{QM-MM} represent the interactions within the MM and between the QM and MM regions, respectively. The QM region, the most interesting part which contains the ion and its surrounding water molecules, is treated quantum mechanically, while the rest of the system is described by classical pair potentials. In general, the post-HF methods

with the extended basis sets are most suitable for the QM treated region but it turns out to be computationally prohibitive. In practice, some essential parameters such as level of quantum mechanics calculations, basis set and size of QM region must be optimized, compromising between the quality of the simulation results and the requirement of CPU time. Since the performance of correlated *ab initio* methods is still far too time-consuming, Hartree-Fock (HF) method was employed for the treatment of all interactions within the QM region. The HF method has been well validated in previous QM/MM studies (Kerdcharoen *et al.*, 1996; Tongraar *et al.*, 1997; Tongraar *et al.*, 1998; Schwenk *et al.*, 2001; Tongraar *et al.*, 2002; Tongraar and Rode, 2003; Rode *et al.*, 2004; Intharathep *et al.*, 2005; Rode *et al.*, 2005; Tongraar and Rode, 2005; Xenides *et al.*, 2005), even for the treatment of anions (Tongraar and Rode, 2003). All quantum mechanical calculations were carried out using DZV+ (Dunning and Hay), LANL2DZ (Dunning and Hay; Hay and Wadt, 1985) and 6-31+G (Hehre *et al.*, 1972; Frisch *et al.*, 1984) basis sets for H₂O, Ca²⁺ and Cl⁻, respectively. The QM sizes with diameters of 8.8 and 9.2 Å were chosen for the systems of aqueous Ca²⁺ and Cl⁻ solutions, respectively. These QM sizes were considered large enough to ensure that the quantum mechanical forces beyond the QM region smoothly converge to pair potential forces. For the treatment of all interactions within the MM and between the QM and MM regions, a flexible model, which describes intermolecular (Stillinger and Rahman, 1976) and intramolecular (Bopp *et al.*, 1983) interactions, was employed for water and the pair potential functions for describing Ca²⁺-H₂O and Cl⁻-H₂O interactions were obtained from previous works (Tongraar *et al.*, 1997; Tongraar and Rode, 2003).

During the QM/MM simulations, exchange of water molecules between the QM and MM regions took place frequently. With regard to this point, the forces acting on each particle in the system were switched according to which region the water molecule was entering or leaving the QM region and is defined as

$$F_i = S_m(r)F_{QM} + (1 - S_m(r))F_{MM}, \quad (6.2)$$

where F_{QM} and F_{MM} are quantum mechanical and molecular mechanical forces, respectively. $S_m(r)$ is a smoothing function (Brooks *et al.*, 1983) described by

$$\begin{aligned} S_m(r) &= 1, & \text{for } r \leq r_1, \\ S_m(r) &= \frac{(r_0^2 - r^2)^2(r_0^2 + 2r^2 - 3r_1^2)}{(r_0^2 - r_1^2)^3}, & \text{for } r_1 < r \leq r_0, \\ S_m(r) &= 0, & \text{for } r > r_0, \end{aligned} \quad (6.3)$$

where r_1 and r_0 are the distances characterizing the start and the end of the QM region, applied within an interval of 0.2 Å (*i.e.*, between the Ca^{2+} -O and Cl^- -O distances of 4.2-4.4 and 4.4-4.6 Å, respectively).

The QM/MM MD simulations for aqueous Ca^{2+} and Cl^- solutions were separately performed in a canonical ensemble at 298 K with periodic boundary conditions. The system's temperature was kept constant using the Berendsen algorithm (Berendsen *et al.*, 1984). A periodic box, with a box length of 18.17 Å, contains one ion and 199 water molecules, corresponding to the experimental density of pure water. The reaction-field method (Adams *et al.*, 1979) was employed for the treatment of long-range interactions. The Newtonian equations of motions were treated by a general predictor-corrector algorithm. The time step size was set to 0.2 fs, which allows for the explicit movement of the hydrogen atoms of water molecules. For both aqueous Ca^{2+} and Cl^- solutions, the simulations were started with the system's re-equilibration for 25000 time steps, followed by another 250000 (Ca^{2+}) and 100000 (Cl^-) time steps

to collect the configurations every 10th step. This part were performed by our collaborator (Tongraar, A.).

6.3.2 XAS data analysis

For each of aqueous ion species, the QM/MM MD snapshots taken every 0.5 ps interval were coupled to electron scattering simulations to produce a set of theoretical XAS spectra. To compare with the experimental measurements, the simulated XAS spectrum is thus an average over the spectra of all selected QM/MM MD snapshots. In the present study, FEFF8.2 program codes (Ankudinov *et al.*, 1998; Ankudinov *et al.*, 2002), which utilize a full multiple scattering approach based on *ab initio* overlapping muffin-tin potentials, were used to generate the spectra. The muffin-tin potentials were obtained using self-consistent calculations with Hedin-Lundqvist (HL) exchange-correlation function (Hedin and Lundqvist, 1969). The self-consistent calculations were performed in a sphere with 5.6 Å cutoff radius (contains ~25-30 water molecules) beyond the absorbing atom. This sphere is considered to be large enough to take into account the influence of outer solvation shell in the computed spectra, yielding realistic electron relaxations. The full multiple scattering calculations include all possible paths within a larger cluster with radius of 9.2 Å (~105-110 water molecules).

According to the standard method in the EXAFS data analysis (Rehr *et al.*, 1992; Newville *et al.*, 1995), the average EXAFS spectrum is obtained from a configurational average,

$$\bar{\chi}(E) = \frac{\mu(E) - \mu_0(E)}{\Delta\mu_0(E_0)}, \quad (6.4)$$

where $\mu(E)$ is the absorption coefficient as a function of the x-ray energy $E = E_0 + \hbar^2 k^2 / 2m_e$, $\mu_0(E)$ is the background absorption coefficient, and $\Delta\mu_0(E_0)$ is the absorption edge height. Structural parameters corresponding to this spectrum can be obtained by fitting a model to an expression

$$\bar{\chi}(k) = \sum_i N_i S_0^2 \frac{\bar{F}_i(k)}{k\bar{R}_i^2} e^{-2\bar{R}_i/\lambda(k) - 2k^2\sigma_i^2} \sin[2k\bar{R}_i + \bar{\varphi}_i(k) - \frac{4}{3}C_{3,i}k^3], \quad (6.5)$$

where $\bar{\chi}(k)$ is the average of the total amplitude as a function of the wavenumber, k . The fitted parameters include N_i , the coordination number, R_i , the mean ion-oxygen distance, σ_i^2 , the Debye-Waller (DW) factor, and $C_{3,i}$, the anharmonicity of the pair-distribution. $\bar{F}_i(k)$, $\bar{\varphi}_i(k)$, and $\lambda(k)$ are the average amplitude, average phase, and mean-free-path factors, respectively. These parameters are obtained by fitting a spectrum with EXAFSPAK package (George and Pickering, 1995). The S_0^2 term is the core-hole or amplitude-reduction factor, which is treated empirically (Fulton *et al.*, 2003). In the EXAFS data analysis, it should be noted that the uncertainties in the experimental estimate of S_0^2 could lead to an error of approximately 20% for the values of the coordination numbers. Especially for more disordered systems, where the multi-electron excitation is a significant portion of the background function, the errors in estimating the coordination numbers may be higher. Contact ion pairs could be excluded, since it has been shown that there was no Ca^{2+} - Cl^- formation even for 6.0 *m* CaCl_2 aqueous solution (Fulton *et al.*, 2003).

To obtain a real-space representation of the EXAFS spectra, Fourier transformations (FT), as implemented in the FEFFIT package (Rehr *et al.*, 1992; Newville *et al.*, 1995), of the structural factors were carried out using

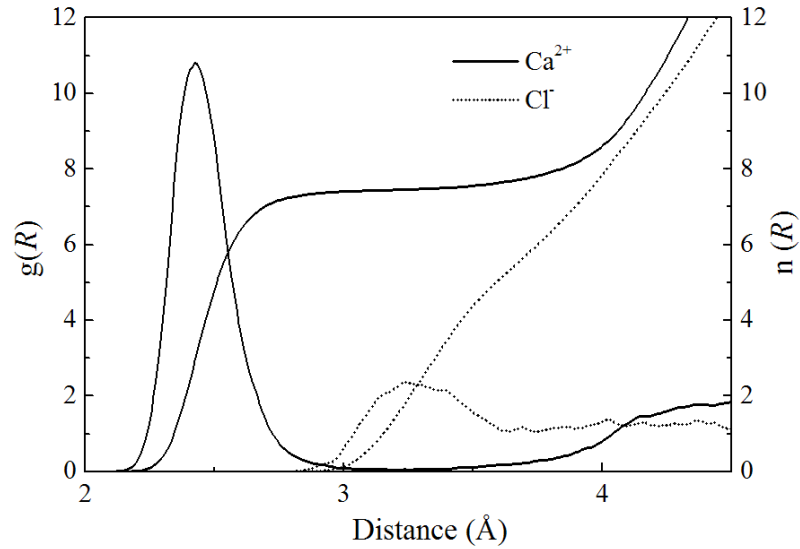


Figure 6.2 Ca^{2+} -O and Cl^- -O RDFs and their corresponding integration numbers.

$$\tilde{\chi}(R) = \frac{1}{\sqrt{2\pi}} \int_0^{\infty} k \chi(k) W(k) e^{i2kR} dk. \quad (6.6)$$

6.4 Results and Discussion

6.4.1 QM/MM MD results

Structural properties of the hydrated Ca^{2+} and Cl^- can be explained in terms of Ca^{2+} -O and Cl^- -O radial distribution functions (RDFs) and their corresponding integration numbers, as shown in Figure. 6.2. For Ca^{2+} , a pronounced first Ca^{2+} -O peak is observed, with maximum at 2.42 Å. The first solvation shell is well-separated from the second one, giving an average coordination number of 7.4 ± 0.1 . In comparison to the previous QM/MM MD results (Tongraar *et al.*, 1997), which reported a broad minimum of the first Ca^{2+} -O RDF with an average number of first-shell waters of 8.3, the observed difference in the coordination number could be

attributed to the use of larger QM size (*i.e.*, in Eq. (3) $r_0 = 4.4$ versus 3.6 \AA (Tongraar *et al.*, 1997)). This implies information that the QM treatment for the non-additive contributions beyond the first hydration shell is crucial in order to correctly describe the hydration shell structure of Ca^{2+} . In the case of Cl^- , a less pronounced first Cl^- -O RDF, with maximum at 3.24 \AA , is observed. The shape and height of the first Cl^- -O peak clearly indicate a high flexibility of this hydrated ion. In addition, the first peak of Cl^- -O RDF is not distinctly separated from the bulk, which suggests an easy exchange of water molecules between the first hydration shell and the outer region. An integration up to first Cl^- -O minimum leads to an average coordination number of 5.8 ± 0.3 . In fact, as a consequence of broad Cl^- -O minimum, the observed coordination number of Cl^- could be regarded as rough estimate, *i.e.*, a small shift in the position of the Cl^- -O minimum could lead to significant difference in the average coordination number. For example, as can be seen in Figure 6.2, the integrations up to the Cl^- -O distances of 3.5 and 4.0 \AA yield 4.5 and 8.0 water molecules, respectively.

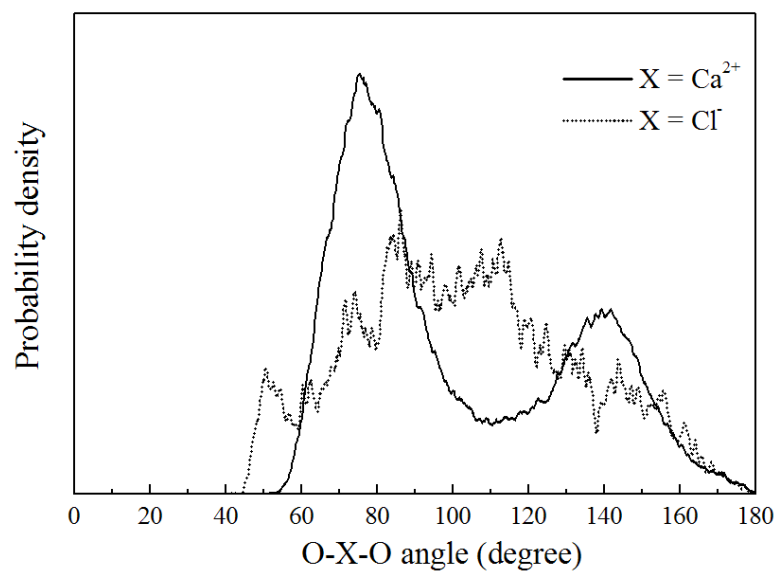


Figure 6.3 Distributions of the coordination numbers of Ca^{2+} and Cl^- , calculated within the first minimum of the Ca^{2+} -O and Cl^- -O RDFs.

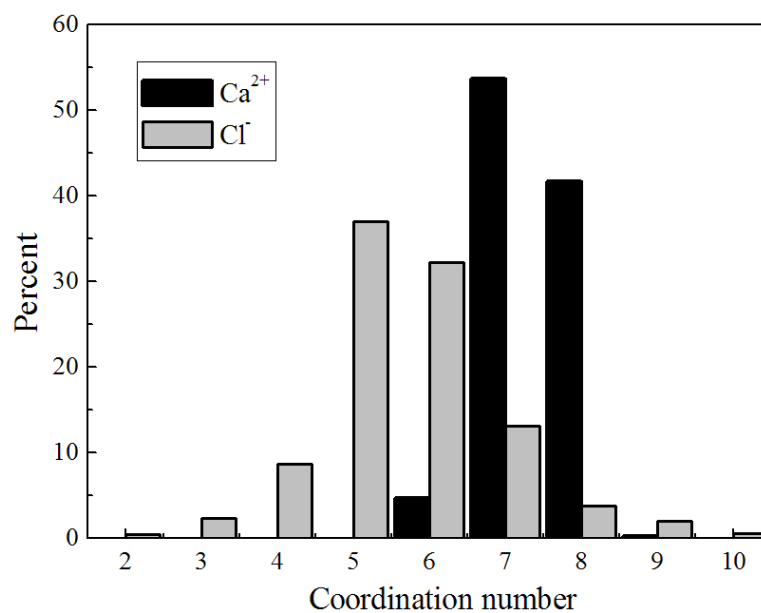


Figure 6.4 Distributions of the coordination numbers of Ca^{2+} and Cl^- , calculated within the first minimum of the Ca^{2+} -O and Cl^- -O RDFs.

Figure 6.3 shows probability distributions of the coordination numbers, calculated within the first minimum of the Ca^{2+} -O and Cl^- -O RDFs, respectively. For Ca^{2+} , the most frequent coordination number for this ion is 7, followed by 8 in smaller amount. In addition, a slight distribution for the coordination number of 6 (~5%) clearly indicate a less significance of $\text{Ca}^{2+}(\text{H}_2\text{O})_6$ formation. In the case of Cl^- , although the 5- and 6-fold coordinated complexes are most frequently found during the QM/MM MD simulation, numerous possible species of the hydrated Cl^- exist, varying from 3 to 9. The observed large variation in the coordination numbers clearly indicates a high flexibility of the hydration structure of Cl^- as well as a high mobility of its first-shell water molecules.

Figure 6.4 displays the O-X-O angular distributions, calculated up to first minimum of the X-O RDFs for $X = \text{Ca}^{2+}$ and Cl^- , respectively. For Ca^{2+} , since the first-shell waters are mainly oriented by the strong influence of the ion, the structural arrangement of this hydrated ion with respect to the distinct coordination numbers between 7 and 8 is well reflected, *i.e.*, by the two pronounced peaks between $60\text{-}90^\circ$ and between $130\text{-}150^\circ$. For Cl^- , the observed broad O- Cl^- -O peak corresponds to the numerous species of hydrated Cl^- complexes appear in aqueous solution. In fact, it should be noted that water molecules in the hydration shell of Cl^- are organized significantly differ from that of Ca^{2+} hydration, *i.e.*, they are arranged with respect to the resultant force of the competition between the $\text{Cl}^- \cdots \text{H-O}$ hydrogen bonds (see Figure 6.5) and the hydrogen bonding among water molecules in the same shell and/or the bulk. Accordingly, this anticipates fast water-exchange rates of the first hydration shell.

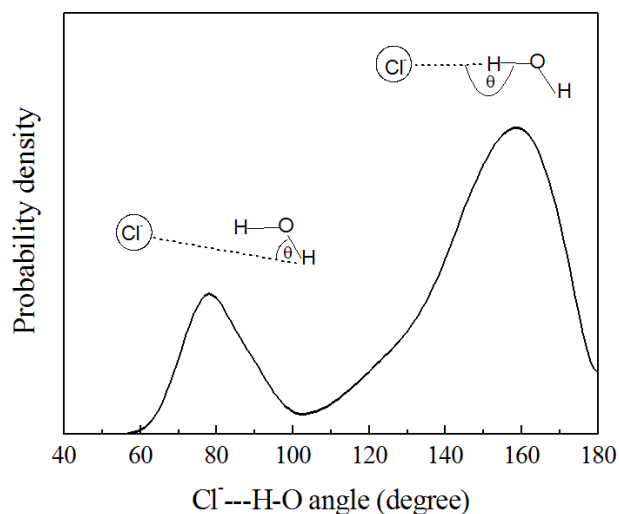


Figure 6.5 Distribution of the Cl⁻---H-O angle, calculated within the first minimum of the Cl⁻-O RDF.

More detailed information on the structural arrangement of the hydrated Ca²⁺ and Cl⁻ complexes can be visualized through the plots of the Ca²⁺-O and Cl⁻-O distances against the simulation times, as shown in Figure 6.6 and 6.7, respectively. According to Figure 6.6, it is obvious that the Ca²⁺(H₂O)₇ and Ca²⁺(H₂O)₈ complexes are dominantly formed in aqueous solution. Within the simulation time of 50 ps, only 12 water molecules are found to be involved in about 27 water exchange processes, indicating that most of the first-shell waters are tightly bound to the ion. This reflects in a well-defined first Ca²⁺ hydration shell. On the contrary, water molecules surrounding the Cl⁻ are quite labile (see Figure 6.7), showing numerous water exchange processes during the QM/MM MD simulation. Such phenomenon is understandable since the Cl⁻-water interactions are relatively weak and are energetically comparable with water-water interactions in bulk water. This clearly indicates an extremely fast dynamics of the hydrated Cl⁻.

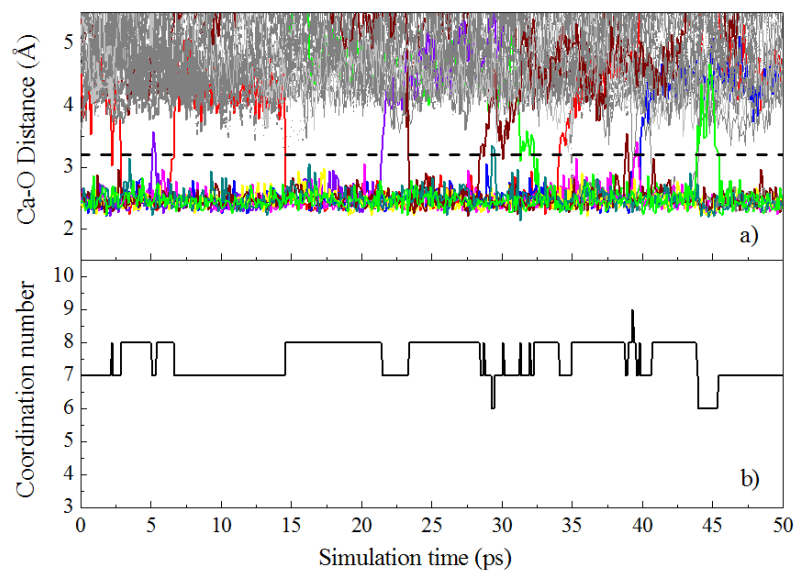


Figure 6.6 Time dependences of (a) Ca^{2+} -O distance and (b) number of first-shell waters, as obtained from the 50 ps of the QM/MM MD simulation. In Figure 6.6a, the dash line parallel to the x-axis positions the first minimum of the Ca^{2+} -O RDF.

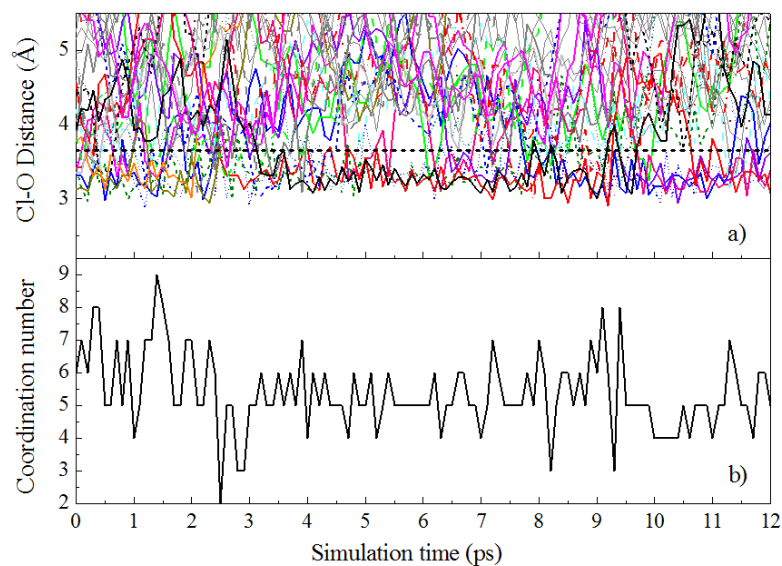


Figure 6.7 Time dependences of (a) Cl^- -O distance and (b) number of first-shell waters, selecting only for the first 12 ps of the QM/MM MD simulation. In Figure 6.7a, the dash line parallel to the x-axis positions the first minimum of the Cl^- -O RDF.

6.4.2 EXAFS and QM/MM-EXAFS spectra

EXAFS is known as a short-range technique, which is well suited in determining the detailed shape of the nearest-neighbor peak in the atom-atom pair correlation functions of disordered systems. For the analysis of EXAFS region, single backscattering processes are dominant and the coordination number of the absorber atom is usually defined with respect to Gaussian shells. However, especially for the relatively large disordered systems, the MS effects may contribute significantly to the spectrum. As a consequence, the pair distribution functions associated with the solvent molecules may not Gaussian in form. Such effects are mostly due to scattering pathways between atoms that located close to the absorber atom. This makes the EXAFS data analysis becomes more difficult, *i.e.*, an incorrect treatment of this asymmetry may reflect in unreliable results (Crozier *et al.*, 1988; D'Angelo *et al.*, 1994).

The combination of MD simulations and EXAFS measurements has recently been applied to Ca^{2+} and Cl^- in aqueous solution (Dang *et al.*, 2006). However, it is important to point out that the MD-EXAFS spectra were generated using MD trajectories derived by means of empirical potentials. A significant contribution of this study is, therefore, to benchmark the performance of QM/MM MD approach in order to generate a more reliable ensemble average, *i.e.*, a better theoretical $\chi(k)$ used in the XAS data analysis. By means of QM/MM-EXAFS, it is worth noting that all details of the ion-water structure inherent in the simulations are represented in the QM/MM-EXAFS spectrum.

According to Figure 6.2, the characteristics of the first Ca^{2+} -O and Cl^- -O RDFs obtained from the QM/MM MD simulations can be analyzed by fitting these two peaks with respect to Gaussian distribution

$$\rho_0 4\pi R^2 g(R) \approx \frac{N_0}{\sqrt{2\pi\sigma^2}} e^{-[(R-R_0)^2]/2\sigma^2}, \quad (6.7)$$

where ρ_0 is the water number density, $4\pi R^2 g(R)$ is the probability of finding the oxygen atoms of water molecules within the interval $(R, R+dR)$ from the ion, N_0 is the coordination number, R_0 is the mean ion-O distance, and σ^2 is the variance or Debye-Waller factor. The results of the fits are plotted in Figure 6.8. All fitted parameters characterizing the first peak of the Ca^{2+} -O and Cl^- -O RDFs are summarized in Table 6.1. As can be seen in Figure 6.8, the first peak of the ion-O RDFs resulting from the QM/MM MD simulations are significantly distorted from Gaussian distributions, especially for the case of Cl^- , showing an asymmetric nature of the first hydration structure. Nevertheless, the fits show reasonable representations of the first hydration shell of both Ca^{2+} and Cl^- . In this respect, it is demonstrated that the neglect of the asymmetric contributions in the fitting could lead to an underestimation of the coordination numbers. A comparison of the coordination numbers as obtained from the detailed analysis of the Ca^{2+} -O and Cl^- -O RDFs in Figure 6.2 and the corresponding data in Table 6.1 clearly confirms this statement. In addition, it should be mentioned that the Debye-Waller factors determined from the simulations are also somewhat different from the “ideal” Gaussian width.

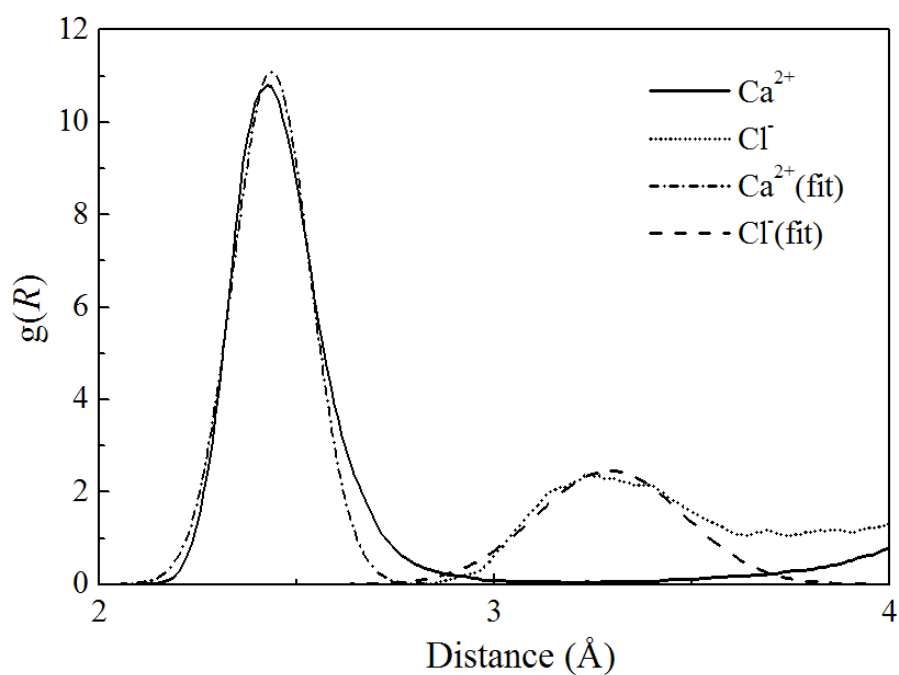


Figure 6.8 Comparison between the first Ca^{2+} -O and Cl^- -O RDFs and their fits with respect to Gaussian function.

Table 6.1 Ion-oxygen distances, Debye-Waller factors, and coordination numbers, as obtained from fitting of the first peak of Ca^{2+} -O and Cl^- -O RDFs.

ion	$R_0(\text{\AA})$	$\sigma^2(\text{\AA}^2)$	N
Ca^{2+}	2.445	0.0096	6.8
Cl^-	3.314	0.0352	5.3

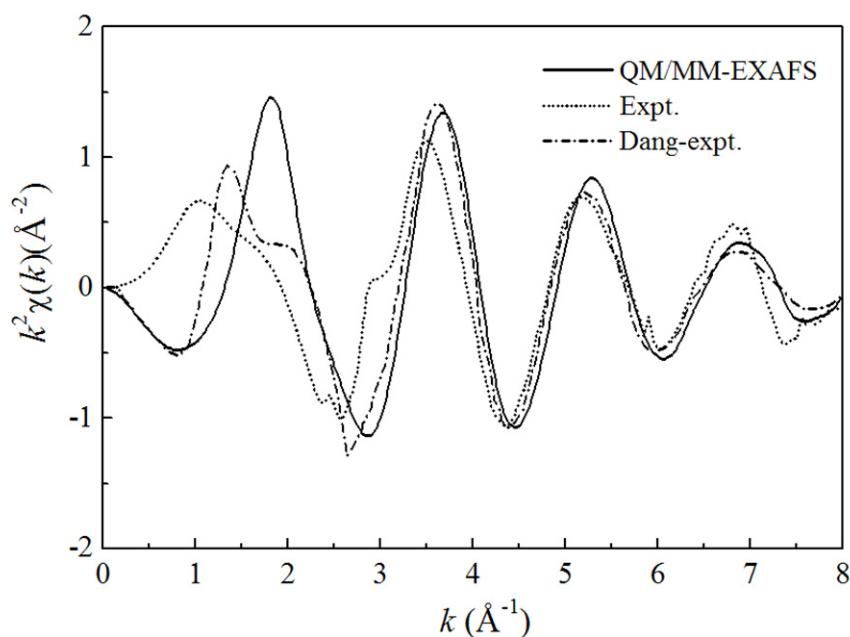


Figure 6.9 Structural factors for Ca^{2+} in water, comparing between the results obtained from the QM/MM MD simulation and the corresponding experimental measurements.

Figure 6.9 and 6.10 show the k^2 -weighted $\chi(k)$ spectra for Ca^{2+} and Cl^- in water, respectively, comparing between the results obtained by the QM/MM MD simulations and the experimental measurements. In addition, the corresponding experimental data measured by Dang *et al.* (Dang *et al.*, 2006) was also given for comparison. For Ca^{2+} (Figure 6.9), the wavelength of the oscillations with respect to k appears to match between the measured EXAFS and the QM/MM-EXAFS spectra, implying that the agreement in the mean Ca^{2+} -O distances is satisfactory. In the case of Cl^- (Figure 6.10), the QM/MM-EXAFS spectrum shows good agreement with the curve measured by Dang *et al.* (Dang *et al.*, 2006) For the pattern of the experimental $\chi(k)$ spectrum, however, the agreement is found to be far from satisfactory, in particular at high k .

Table 6.2 Ion-oxygen distances, Debye-Waller factors, and coordination numbers, as obtained from the analysis of the measured EXAFS spectra.

ion	$R_0(\text{\AA})$	$\sigma^2(\text{\AA}^2)$	N
Ca^{2+}	2.410	0.0123	6.6
	2.429 ^a	0.0115 ^a	6.8 ^a
Cl^-	2.943	0.0455	5.8
	3.110 ^a	0.0290 ^a	6.4 ^a

^a EXAFS measurements from Dang *et al.* (Dang *et al.*, 2006)

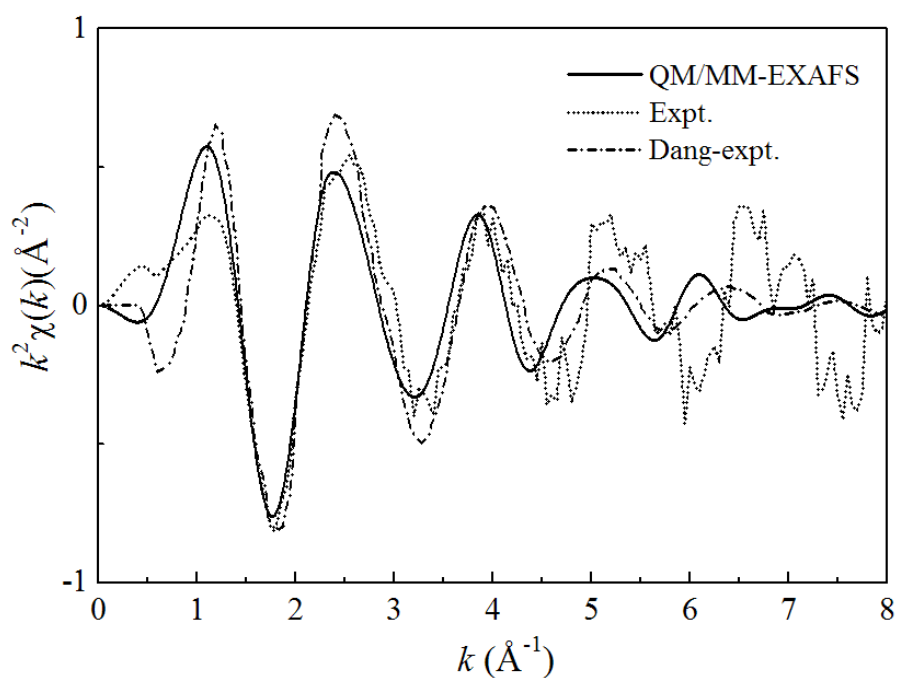


Figure 6.10 Structural factors for Cl^- in water, comparing between the results obtained from the QM/MM MD simulation and the corresponding experimental measurements.

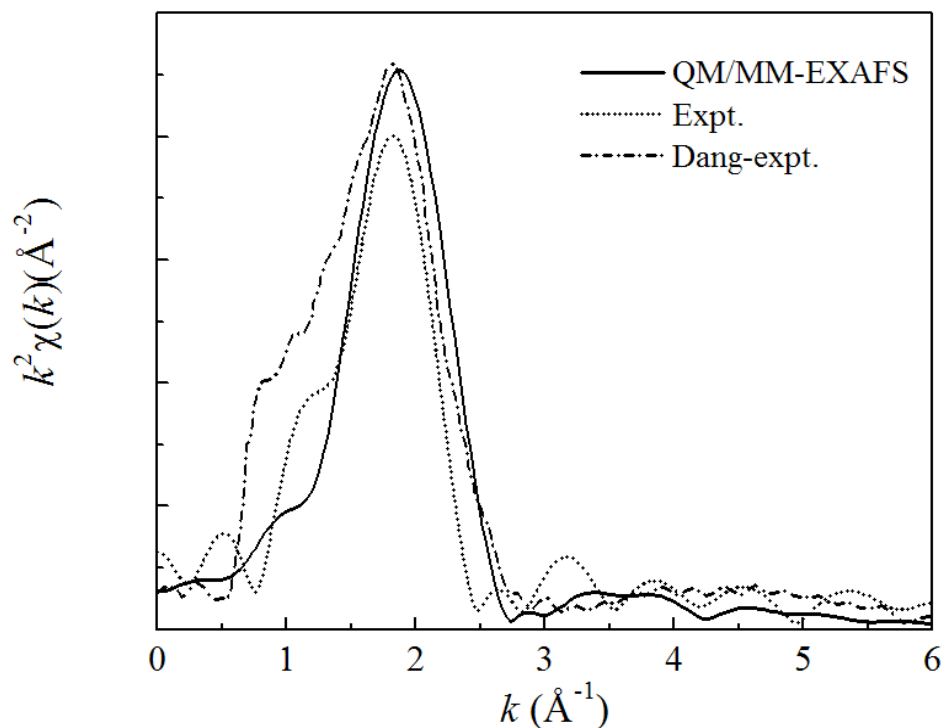


Figure 6.11 Fourier transformations of the structural factors for Ca^{2+} in water, comparing between the results obtained from the QM/MM MD simulation and the corresponding experimental measurements.

Following the expression given by Eq. (6.5), the structural parameters for both aqueous Ca^{2+} and Cl^- systems as determined from the measured EXAFS spectra are reported in Table 6.2. For Ca^{2+} , the simulation results (Table 6.1) are in good agreement with the measured results (Table 6.2), and are in consistent with the experimental data from Dang *et al.* (Dang *et al.*, 2006) In contrast to Ca^{2+} , the problem in determining the hydration shell structure of Cl^- is raised by the weak and asymmetric nature of the Cl^- -water interactions. This apparently reflects in the observed difference of structural parameters determined from the simulations and measurements.

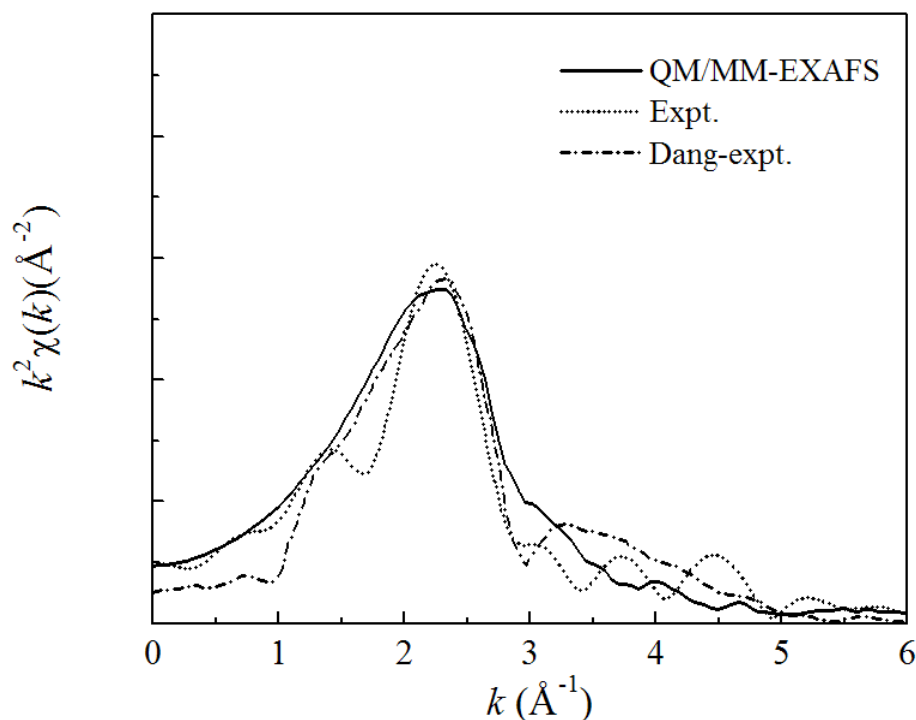


Figure 6.12 Fourier transformations of the structural factors for Cl^- in water, comparing between the results obtained from the QM/MM MD simulation and the corresponding experimental measurements.

For direct comparison, the QM/MM-EXAFS and the corresponding measured EXAFS spectra were transformed (using Eq. (6.6)) into the identical manners, as depicted in Figure 6.11 and 6.12, for the aqueous Ca^{2+} and Cl^- solutions, respectively. With regard to the $\tilde{\chi}(R)$ spectra, the main peak is primarily due to the scattering originated mostly from the oxygen atoms of first-shell water molecules. Considering the feature of the measured EXAFS spectra, the spurious peaks at low-distance values can be understood due to the presence of multi-electron transitions. For both Ca^{2+} and Cl^- systems, it is obvious that the peak positions obtained from the QM/MM-EXAFS spectra are in good accord with the experimental measurements. In addition, the

QM/MM-EXAFS peaks are significantly broader than for the measured ones, supplying information that the solvent molecules surrounding the ions are more disordered in the simulated structures.

6.4.3 XANES and QM/MM-XANES spectra

In the XANES region, since the kinetic energy of the photoelectron is low, the MS effects are dominant. For the case of aqueous Ca^{2+} and Cl^- solutions, these effects are mostly due to scattering pathways between atoms of water molecules surrounding the ions. In general, the XANES spectrum is considered to be insensitive to disorder, but characteristics of the geometrical arrangement of the hydrated ions. Consequently, this spectrum is often used as fingerprint for characterizing neighborhood of the ions. For Ca^{2+} , the XANES spectra generated for every 0.5 ps of the QM/MM MD snapshots are plotted in Figure 6.13. As one can see, the observed variation in the XANES spectra exist, which corresponds to the different geometrical arrangements of the hydrated Ca^{2+} in aqueous solution. To correctly describe the characteristics of this hydrated ion, it should be noted that a representative set of geometries extracted from the QM/MM MD trajectories must cover all possible molecular configurations, *i.e.*, the QM/MM MD simulation must be performed on a time scale that is large enough to provide a reliable ensemble average. A comparison between the measured and simulated XANES spectra is shown in Figure 6.14. Apparently, although each theoretical XANES spectrum shows noticeable difference in the relative intensity of the resonance, the average of them gives satisfactory agreement with the measured one. This supplies information that molecular configurations of Ca^{2+} in aqueous

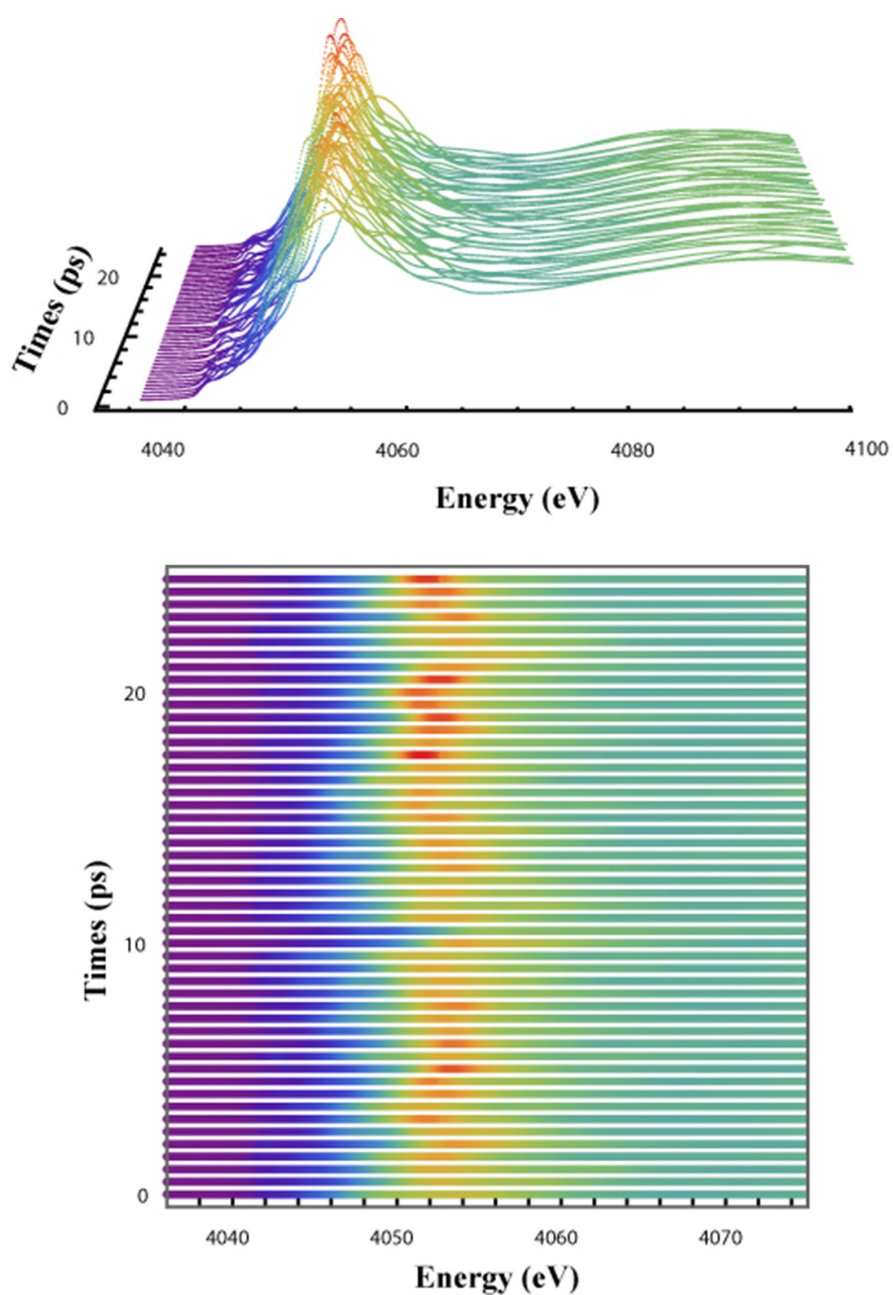


Figure 6.13 Simulated XANES spectra for Ca^{2+} in water, as obtained from each of QM/MM MD snapshots.

solution obtained from the QM/MM MD simulation are realistic, which enable us to understand the characteristics of this hydrated ion, in particular at molecular level.

The feature of the XANES spectrum at about 4049 eV is primarily demonstrated as a result of Ca^{2+} -O single scattering in the first hydration shell (Fulton *et al.*, 2003), in conjunction with minor contributions from the second hydration shell as well as from the first-shell multiple scattering. As can be seen in Figure 6.14, a small feature at about 4039 eV is recognizable, which is assigned to $1s \rightarrow 3d$ transition. This transition is considered as an evidence for the absence of multiple scattering contributions originating from a symmetric octahedral structure. Such phenomenon is in consistent with the coordination number of 6.6 resulted in the EXAFS data analysis.

In the case of Cl^- hydration, where the hydration structure is not well defined, the simulated XANES spectra obtained for every 0.5 ps of the QM/MM MD snapshots show even larger variations (see Figure 6.15), compared to the case of Ca^{2+} . In this sense, the statistical information regarding all possible hydration shell structures instantaneously distorted during the QM/MM MD simulation has an important effect on the average spectrum. In Figure 6.16, it is apparent that the average XANES spectrum shows its feature that is in good accord with the experimental one. This indicates that the geometrical arrangements of the hydrated Cl^- obtained in the QM/MM MD simulation are also realistic. In this context, the molecular configurations obtained by the QM/MM MD simulation can be used as reliable representatives for the geometrical arrangement of the Cl^- hydration.

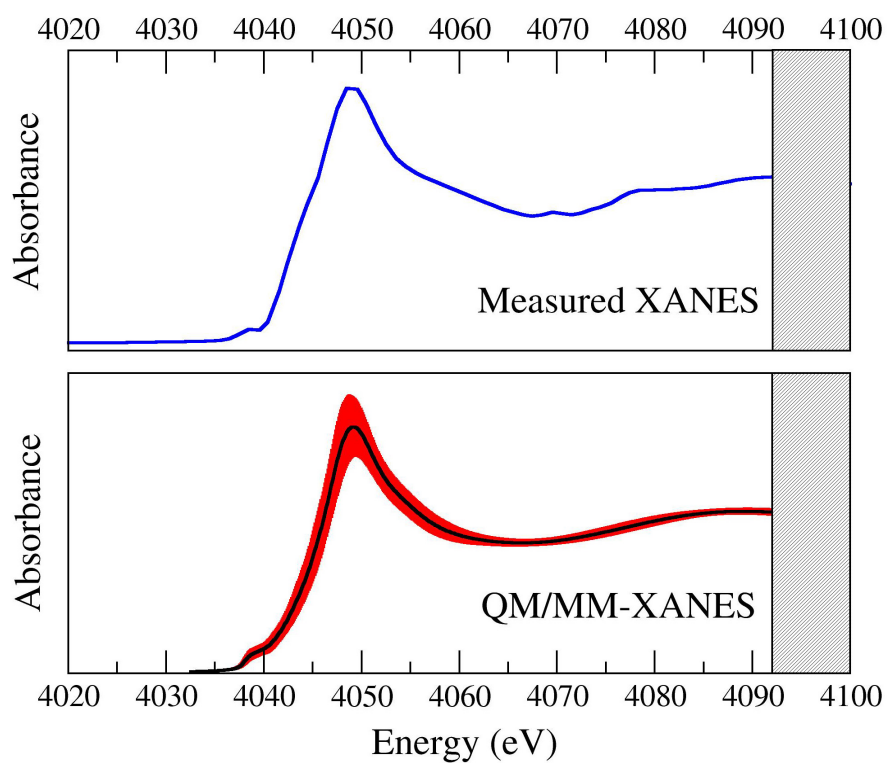


Figure 6.14 Comparison between the experimental Ca *K*-edge XANES spectrum and the spectra obtained from the QM/MM MD simulation. The simulation results are displayed in terms of an average XANES spectrum, together with the standard deviations taken from the overall QM/MM MD snapshots.

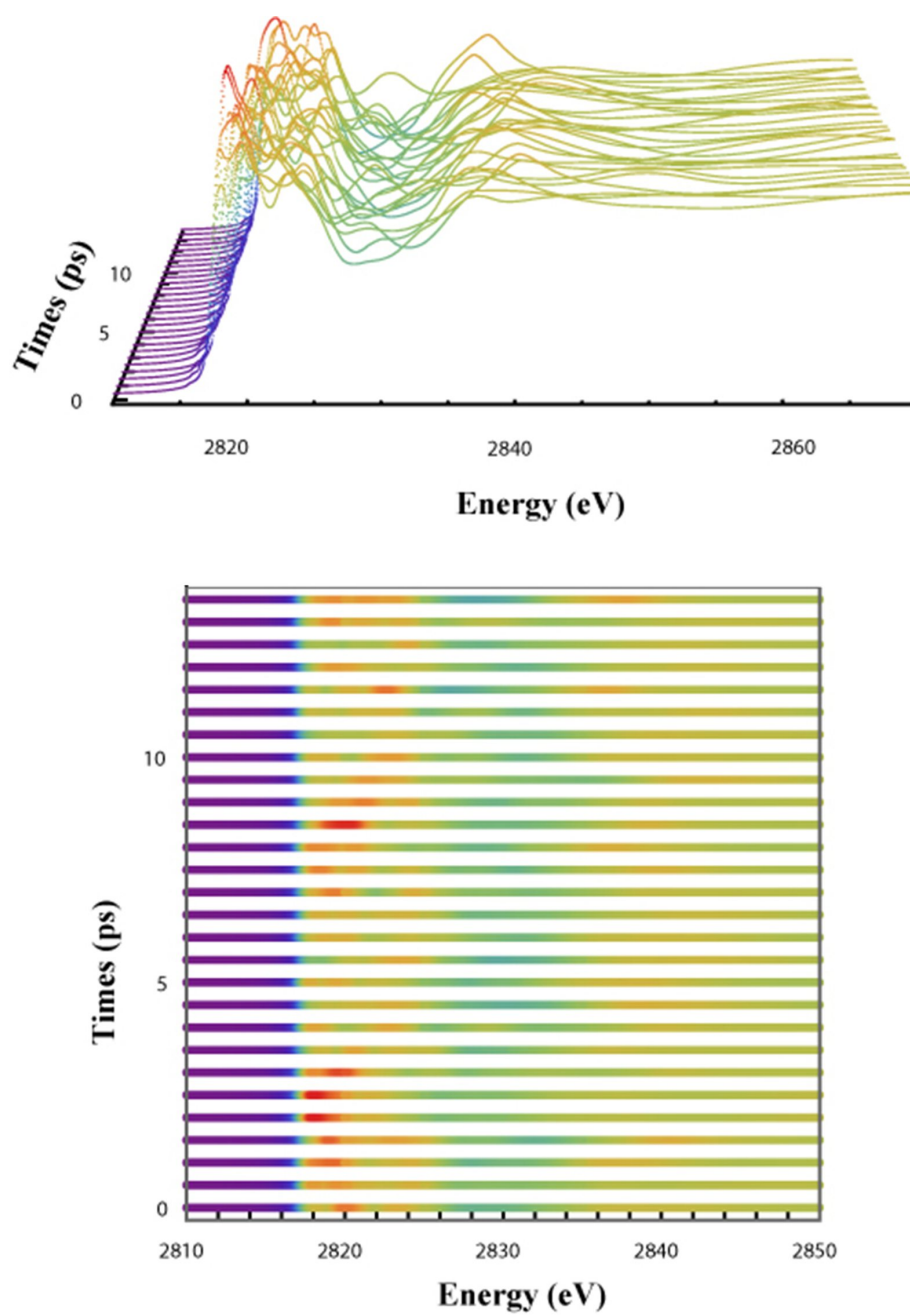


Figure 6.15 Simulated XANES spectra for Cl^- in water, as obtained from each of QM/MM MD snapshots.

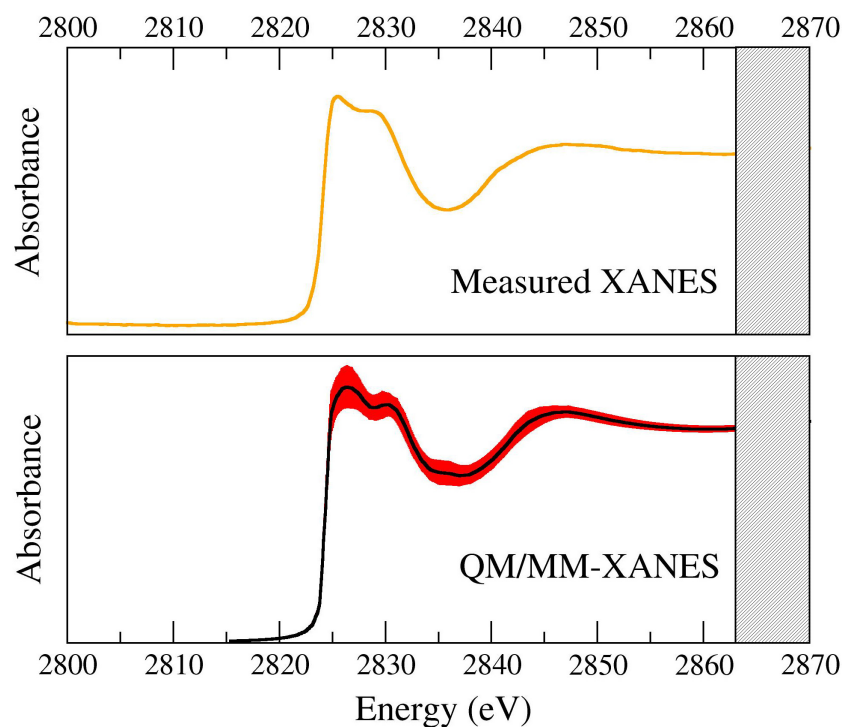


Figure 6.16 Comparison between the experimental Cl *K*-edge XANES spectrum and the spectra obtained from the QM/MM MD simulation. The simulation results are displayed in terms of an average XANES spectrum, together with the standard deviations taken from the overall QM/MM MD snapshots.

6.5 Conclusion

In this work, we combine the QM/MM MD technique with the corresponding XAS measurements for studying the hydration shell structure of Ca^{2+} and Cl^- . The QM/MM MD results and the detailed analysis on the measured XAS spectra clearly indicate the characteristically low symmetry and disordered nature of the first coordination shell of these ions, especially for the case of Cl^- . In terms of XAS measurements, the presence of MS effects in the measured spectra and the errors from asymmetric distributions are of the major problems in the analysis of the XAS data.

To simplify these problems, QM/MM MD simulations have been performed to generate theoretical XAS spectra, from which these spectra have been used as starting models in the XAS data analysis. By this scheme, since the accuracy in the interpretation of XAS data depends crucially on the reliability of the simulated XAS models, the use of QM/MM MD technique is highly recommended, over other MM approaches, in order to generate a more reliable ensemble average, *i.e.*, a better theoretical $\chi(k)$. In particular for XANES, since there is no direct relationship between the XANES spectrum and the geometry of the hydrated ion, a representative set of geometries of the hydrated ions extracted from the QM/MM MD trajectories is extremely useful in order to simplify the process of XANES data interpretation.

6.6 References

- Adams, D. J., Adams, E. H., and Hills, G. J. (1979). The computer simulation of polar liquids. **Mol. Phys.** 38: 387.
- Ankudinov, A. L., Bouldin, C. E., Rehr, J. J., Sims, J., and Hung, H. (2002). Parallel calculation of electron multiple scattering using Lanczos algorithms. **Phys. Rev. B** 65: 104107.
- Ankudinov, A. L., Ravel, B., Rehr, J. J., and Conradson, S. D. (1998). Real-space multiple-scattering calculation and interpretation of x-ray-absorption near-edge structure. **Phys. Rev. B** 58: 7565.
- Berendsen, H. J. C., Postma, J. P. M., van Gunsteren, W. F., DiNola, A., and Haak, J. R. (1984). Molecular dynamics with coupling to an external bath. **J. Phys. Chem.** 81: 3684.

- Bopp, P., Jancsó, G., and Heinzinger, K. (1983). An improved potential for non-rigid water molecules in the liquid phase. **Chem. Phys. Lett.** 98: 129.
- Brooks, B. R., Bruccoleri, R. E., Olafson, B. D., States, D. J., Swaminathan, S., and Karplus, M. (1983). A program for macromolecular energy, minimization, and dynamics calculations. **J. Comput. Chem.** 4: 187.
- Chandrasekhar, J., Spellmayer, D. C., and Jorgensen, W. L. (1984). Energy component analysis for dilute aqueous solutions of lithium(1+), sodium(1+), fluoride(1-), and chloride(1-) ions. **J. Am. Chem. Soc.** 106: 903.
- Clementi, E., Barsotti, R., Fromm, J., and Watts, R. O. (1976). Study of the structure of molecular complexes. **Theor. Chim. Acta** 43: 101.
- Crozier, D. E. (1995). Impact of the asymmetric pair distribution function in the analysis of XAFS. **Physica B** 208-209: 330.
- Crozier, D. E. (1997). A review of the current status of XAFS spectroscopy. **Nucl. Instrum. Methods Phys. Res. B** 133: 134.
- Crozier, D. E., Rehr, J. J., and Ingalls, R. (1988). **X-ray Absorption: Principles, Applications, Techniques of EXAFS, SEXAFS and XANES**. New York: Wiley.
- Cummings, S., Enderby, J. E., and Howe, R. A. (1980). Ion hydration in aqueous CaCl₂ solutions. **J. Phys. C** 13: 1.
- D'Angelo, P., Di Nola, A., Filipponi, A., Pavel, N. V., and Roccatano, D. (1994). An Extended X-ray Absorption Fine Structure study of aqueous solutions by employing Molecular Dynamics simulations. **J. Chem. Phys.** 100: 985.

- D'Angelo, P., Di Nola, A., Giglio, E., Mangoni, M., and Pavel, N. V. (1995). EXAFS Study of Micellar Aggregates of Bile Acid Rubidium Salts. **J. Phys. Chem.** 99: 5471.
- D'Angelo, P. and Pavel, N. V. (1999). Evidence of three-body correlation functions in Rb^+ and Sr^{2+} acetonitrile solutions. **J. Chem. Phys.** 111: 5107.
- D'Angelo, P. and Pavel, N. V. (2001). EXAFS and molecular dynamics studies of ionic solutions. **J. Synchrotron Rad.** 8: 173.
- Dang, L. X., Schenter, G. K., Glezakou, V.-A., and Fulton, J. L. (2006). Molecular simulation analysis and X-ray absorption measurement of Ca^{2+} , K^+ and Cl^- ions in solution. **J. Phys. Chem. B** 110: 23644.
- Di Cicco, A. (1996). Local Structure in binary liquids probed by EXAFS. **J. Phys.: Condens. Matter** 8: 9341.
- Di Cicco, A., Rosolen, M. J., Marassi, R., Tossici, R., Fillipponi, A., and Rybicki, J. (1996). Short-range order in solid and liquid KBr probed by EXAFS. **J. Phys.: Condens. Matter** 8: 10779.
- Di Cicco, A., Taglienti, M., Minicucci, M., and Filippini, A. (2000). Short-range structure of solid and liquid AgBr determined by multiple-edge x-ray absorption spectroscopy. **Phys. Rev. B** 62: 12001.
- Dunning, T. H. J. and Hay, P. J. **Modern Theoretical Chemistry.** New York: Plenum.
- Enderby, J. E. and Neilson, G. W. (1981). The structure of electrolyte solutions. **Rep. Prog. Phys.** 44: 593.

- Floris, F. M., Persico, M., Tani, A., and Thomasi, J. (1994). Hydration shell structure of the calcium ion from simulations with ab initio effective pair potentials. **Chem. Phys. Lett.** 227: 126.
- Frank, H. (1956). **Chemical Physics of Ionic Solutions.** New York: John Wiley&Sons.
- Frisch, M. J., Pople, J. A., and Binkley, J. S. (1984). Self-consistent molecular orbital methods 25. Supplementary functions for Gaussian basis sets. **J. Chem. Phys.** 80: 3265.
- Fulton, J. L., Heald, M. S., Badyal, Y. S., and Simonsom, J. M. (2003). Understanding the Effects of Concentration on the Solvation Structure of Ca^{2+} in Aqueous Solution. I: The Perspective on Local Structure from EXAFS and XANES. **J. Phys. Chem. A** 107: 4688.
- Fulton, J. L., Hoffmann, M. M., Darab, J. G., Palmer, B. J., and Stern, E. A. (2000). Copper(I) and Copper(II) Coordination Structure under Hydrothermal Condition at 325°C: An XAFS, and MD Study. **J. Phys. Chem. A** 104: 11651.
- George, G. N. and Pickering, I. J. (1995). EXAFSPAK, a suite of computer programs for analysis of X-ray absorption spectra. Stanford Synchrotron Radiation Laboratory, Standford, CA.
- Hay, P. J. and Wadt, W. R. (1985). Ab initio effective core potentials for molecular calculations. Potentials for the transition metal atoms Sc to Hg. **J. Chem. Phys.** 82: 270.
- Hedin, L. and Lundqvist, S. (1969). Effects of Electron-Electron and Electron-Phonon Interactions on the One-Electron States of Solids. **Solid State Phys.** 23: 1.

- Hehre, W. J., Ditchfield, R., and Pople, J. A. (1972). Self-Consistent Molecular Orbital Methods. XII. Further Extensions of Gaussian-Type Basis Sets for Use in Molecular Orbital Studies of Organic Molecules. **J. Chem. Phys.** 56: 2257.
- Heinzinger, K. (1985). The structure of aqueous electrolyte solutions as derived from MD (molecular dynamics) simulations. **Pure Appl. Chem.** 57: 1031.
- Hewish, N. A., Neilson, G. W., and Enderby, J. E. (1982). Environment of Ca^{2+} ions in aqueous solvent. **Nature** 297: 138.
- Howell, I. and Neilson, G. W. (1996). Li^+ hydration in concentrated aqueous solution. **J. Phys.: Condensed Matter.** 8: 4455.
- Ignaczak, A., Gomes, J. A. N. F., and Cordeiro, M. N. D. S. (1999). Quantum and simulation studies of $\text{X}^-(\text{H}_2\text{O})_n$ systems. **Electrochim. Acta** 45: 659.
- Impey, R. W., Madden, P. A., and McDonald, I. R. (1983). Hydration and mobility of ions in solution. **J. Phys. Chem.** 87: 5071.
- Intharathap, P., Tongraar, A., and Sagarik, K. (2005). Structure and dynamics of hydrated NH_4^+ : An ab initio QM/MM molecular dynamics simulation. **J. Comput. Chem.** 26: 1329.
- Jalilevand, F., Spangberg, D., Lindqvist-Reis, P., Hermansson, K., Persson, I., and Sandström, M. (2001). Hydration of the Calcium Ion. An EXAFS, Large-Angle X-ray Scattering, and Molecular Dynamics Simulation Study. **J. Am. Chem. Soc.** 123: 431.
- Kalko, S. G., Sesé, G., and Padro, J. A. (1996). On the effects of truncating the electrostatic interactions: Free energies of ion hydration. **J. Chem. Phys.** 104: 9578.

- Kerdcharoen, T., Liedl, K. R., and Rode, B. M. (1996). QM/MM simulation method applied to the solvation of Li^+ in ammonia. **Chem. Phys.** 211: 313.
- Koneshan, S., Rasaiah, J. C., Lynden-Bell, R. M., and Lee, S. H. (1998). Solvent Structure, Dynamics, and Ion Mobility in Aqueous Solutions at 25°C. **J. Phys. Chem. B** 102: 4193.
- Kuzmin, A., Obst, S., and Purans, J. (1997). X-ray absorption spectroscopy and molecular dynamics studies of Zn^{2+} hydration in aqueous solutions. **J. Phys.; Condens. Matter** 9: 10065.
- Licheri, G., Piccaluga, G., and Pinna, P. (1976). X-ray diffraction study of the average solute species in CaCl_2 aqueous solutions. **J. Chem. Phys.** 64: 2437.
- Magini, M. (1988). **X-ray Diffraction of Ions in Aqueous Solution: Hydration and Complex Formation.** Florida: CRC Press Inc.
- Mezei, M. and Beveridge, D. L. (1981). Monte Carlo studies of the structure of dilute aqueous solutions of Li^+ , Na^+ , K^+ , F^- , and Cl^- . **J. Chem. Phys.** 74: 6902.
- Neilson, G. W. (1988). Diffraction studies of aqueous electrolyte solutions. **Pure & Appl. Chem.** 60: 1797.
- Neilson, G. W. and Tromp, R. H. (1991). Neutron and X-ray diffraction on aqueous solutions. **Annul. Rev. Phys. Chem. c.** 88: 45.
- Newville, M., Ravel, B., Haskel, D., Rehr, J. J., Stern, E. A., and Yacoby, Y. (1995). Analysis of multiple-scattering XAFS data using theoretical standards. **Physica B** 208-209: 154.
- Obst, S. and Bradaczek, H. (1996). Molecular Dynamics Study of the Structure and Dynamics of the Hydration Shell of Alkaline and Alkaline-Earth Metal Cations. **J. Phys. Chem.** 100: 15677.

- Ohtaki, H. and Radnai, T. (1993). Structure and dynamics of hydrated ions. **Chem. Rev.** 93: 1157.
- Pálinkás, G. and Heinzinger, K. (1986). Hydration shell structure of the calcium ion. **Chem. Phys. Lett.** 126: 251.
- Probst, M. M., Radnai, T., Heinzinger, K., Bopp, P., and Rode, B. M. (1985). Molecular Dynamics and X-Ray Investigation of an Aqueous CaCl₂ Solution. **J. Phys. Chem.** 89: 753.
- Rehr, J. J., Albers, R. C., and Zabinsky, S. I. (1992). High-order multiple-scattering calculations of x-ray-absorption fine structure. **Phys. Rev. Lett.** 69: 3397.
- Rode, B. M., Schwenk, C. F., Hofer, T. S., and Randolph, B. R. (2005). Coordination and ligand exchange dynamics of solvated metal ions. **Coor. Chem. Rev.** 249: 2993.
- Rode, B. M., Schwenk, C. F., and Tongraar, A. (2004). Structure and dynamics of hydrated ions - New insights through quantum mechanical simulations. **J. Mol. Liq.** 110: 105.
- Rossano, S., Ramos, A., Delaye, J.-M., Filipponi, A., Brouder, C., and Calas, G. (1999). Iron surrounding in CaO-FeO-2SiO₂ glass: EXAFS and molecular dynamics simulation. **J. Synchrotron Radiat.** 6: 247.
- Schwenk, C. F., Loeffler, H. H., and Rode, B. M. (2001). Molecular dynamics simulations of Ca²⁺ in water: Comparison of a classical simulation including three-body corrections and Born-Oppenheimer ab initio and density functional theory quantum mechanical/molecular mechanics simulations. **J. Chem. Phys.** 115: 10808.

- Skipper, N. T., Neilson, G. W., and Cummings, S. C. (1989). An X-ray diffraction study of $\text{Ni}_{(\text{aq})}^{2+}$ and $\text{Mg}_{(\text{aq})}^{2+}$ by difference methods. **J. Phys.: Condensed Matter.** 1: 3489.
- Smirnov, P., Yamagami, M., Wakita, H., and Yamaguchi, T. (1997). An X-Ray Diffraction Study on Concentrated Aqueous Calcium Nitrate Solutions at Subzero Temperatures. **J. Mol. Liq.** 73-74: 305.
- Smith, D. E. and Dang, L. X. (1994). Computer simulations of cesium–water clusters: Do ion–water clusters form gas-phase clathrates?. **J. Chem. Phys.** 101: 7873.
- Spangberg, D., Hermansson, K., Lindqvist-Reis, P., Jalilevand, F., Sandström, M., and Persson, I. (2000). Model Extended X-ray Absorption Fine Structure (EXAFS) Spectra from Molecular Dynamics Data for Ca^{2+} and Al^{3+} Aqueous Solutions. **J. Phys. Chem. B** 104: 10467.
- Stillinger, F. H. and Rahman, A. (1976). Revised central force potentials for water. **J. Chem. Phys.** 68: 666.
- Tongraar, A., Liedl, K. R., and Rode, B. M. (1997). Solvation of Ca^{2+} in Water Studied by Born–Oppenheimer ab Initio QM/MM Dynamics. **J. Phys. Chem. A** 101: 6299.
- Tongraar, A., Liedl, K. R., and Rode, B. M. (1998). Born–Oppenheimer ab Initio QM/MM Dynamics Simulations of Na^+ and K^+ in Water: From Structure Making to Structure Breaking Effects. **J. Phys. Chem. A** 102: 10340.
- Tongraar, A. and Rode, B. M. (2003). The hydration structures of F^- and Cl^- investigated by ab initio QM/MM molecular dynamics simulation. **Phys. Chem. Chem. Phys.** 5: 357.

- Tongraar, A. and Rode, B. M. (2005). Ab initio QM/MM dynamics of anion-water hydrogen bonds in aqueous solution. **Chem. Phys. Letts.** 403: 314.
- Tongraar, A., Sagarik, K., and Rode, B. M. (2002). Preferential solvation of Ca^{2+} in aqueous ammonia solution: Classical and combined ab initio quantum mechanical/molecular mechanical molecular dynamics simulations. **Phys. Chem. Chem. Phys.** 4: 628.
- Trapananti, A., Di Cicco, A., and Minicucci, M. (2002). Structural disorder in liquid and solid CuI at high temperature probed by x-ray absorption spectroscopy. **Phys. Rev. B** 66: 014202.
- Wallen, S. L., Palmer, B. J., and Fulton, J. L. (1998). The ion pairing and hydration structure of Ni^{2+} in supercritical water at 425°C determined by x-ray absorption fine structure and molecular dynamics studies. **J. Chem. Phys.** 108: 4039.
- Williams, R. J. P. (1971). **Bio-inorganic Chemistry**. Washington DC: American Chemical Society.
- Xenides, D., Randolph, B. R., and Rode, B. M. (2005). Structure and Ultrafast Dynamics of Liquid Water: A QM/MM MD Simulations Study. **J. Chem. Phys.** 122: 174506.

CHAPTER VII

CONCLUSION AND FUTURE WORK

A brief theoretical background of first-principles density functional theory was given in Chapter II. In Chapter IV, the vibrational frequency of O and H defects in CdTe obtained from first-principles calculations were calculated and used to compare with the corresponding IR measurements. Our results show that the IR signature of O_{Te} in CdTe has been correctly identified by Ramdas's Group. However, our results show that their identifications of high frequency modes are faulty. The more likely structures are presented and discussed. In Chapter V, the study of InON alloys was presented. A combination of first-principles calculations and XAS measurement was used to identify the local structure of indium oxynitride films with various O:N ratios. The XANES spectra are sensitive to the local structure of the absorbing atom (in this case In). It is found that the XANES shape is sensitive to the coordination number of In (four-fold/six-fold) but not very sensitive to the neighboring specie (O or N). The XANES spectrum of each sample, when used in conjunction with the simulation, was used to determine the amount of four-fold and six-fold In atoms in the alloy. In Chapter IV, a combination of first-principles calculations and XAS measurement was used to verify the dynamic hydration structures of ions (Ca^{2+} and Cl^-) in aqueous solutions. It is found that XANES spectrum is sensitive to the movement (dynamic) of water molecules around ion. As a result, the XANES measurement can be used to compare with the average XANES spectrum based on QM/MM dynamics over

sufficiently long time. If the dynamic of the hydration structure is properly simulated, the average XANES spectrum should be consistent with the measured one.

A combination of first-principles density functional simulations with the corresponding experimental measurements such as IR or XAS measurements is a powerful technique for analyzing the defect structures in materials. This technique can be applied to both periodic systems (solid) as well as non-periodic systems (liquid).

In the future, we are planning to investigate the local structures and some physical properties of various defects and impurities in different materials. Examples include Cr-doped Al_2O_3 , Mn-doped BaTiO_3 , and Br^- in aqueous solutions.

APPENDICES

APPENDIX A

CODES FOR PREPARATION OF INPUT FILES AND EXTRACTING FORCES FOR DYNAMIC MATRIX CALCULATIONS

Vibrational frequencies of defects or impurities in the crystals can be determined by using first-principles method described in the Chapter II and IV. In each case of the full dynamic matrix calculations, we need to construct the dynamic matrix from the forces acting on each atom (Hellmann-Feynman forces) as an atom in the system displaced. Since there are, in general, many atoms in the system, the task of displacing one atom in one direction at a time and collecting all forces is very laborious to do manually. For this reason, we created Fortran codes to prepare a set of VASP input files. At the issuing a series of VASP run, the codes construct the dynamic matrix and calculate the vibrational frequencies by solving the dynamic matrix. First, we created the codes to shift each atom from its equilibrium positions (one at a time), i.e., $x \pm \Delta$, $y \pm \Delta$, or $z \pm \Delta$, where Δ is a small value (Table A.1). From this codes, we get $3N \times 2$ (N is the number of atoms in the crystal) position files (POSCAR). After that, a script to issue a series of VASP run is used to calculate the Hellmann-Feynman forces acting on each atom from each position file. To construct the dynamic matrix, we created the codes (shown in Table A.2) to pick the needed data from the output files of VASP codes and constructed the dynamic matrix. The vibrational frequency and

vibrational mode can be obtained from the eigenvalues and eigenvectors of the constructed dynamic matrix. We generated the codes to diagonalize the dynamic matrix to obtain the eigenvalues and eigenvectors (Table A.3).

Table A.1 The Fortran codes used for moving each atom from its equilibrium position.

```
*   Written by Mr.Jiraroj T-Thienprasert
      program vaspDYNAMIC
*
*
*
      implicit none
      integer typemax,nmax
      parameter(typemax=5,nmax=500)
      integer i,typ,atom,n(typemax),p,s,t,q,k,l
      real*8 ax(3),ay(3),az(3),step
      double precision alat,x(nmax),y(nmax),z(nmax),xp(nmax)
      double precision xn(nmax),yp(nmax),yn(nmax),zp(nmax),zn(nmax)
      .,A(nmax,3),B(nmax,3),C(nmax,3)
      character*80 heading
      character*12 pick
      character*12 posn(500,3),posp(500,3)
      character*1 lattype
*
*   direction + step
      posp(1,1) = 'POSCARP1,1'
      posp(1,2) = 'POSCARP1,2'
      posp(1,3) = 'POSCARP1,3'
      posp(2,1) = 'POSCARP2,1'
      posp(2,2) = 'POSCARP2,2'
      ...
      posp(108,3) = 'POSCARP108,3'
      posp(109,1) = 'POSCARP109,1'
      posp(109,2) = 'POSCARP109,2'
      posp(109,3) = 'POSCARP109,3'
*   direction -step
      posn(1,1) = 'POSCARN1,1'
      posn(1,2) = 'POSCARN1,2'
      posn(1,3) = 'POSCARN1,3'
      posn(2,1) = 'POSCARN2,1'
      posn(2,2) = 'POSCARN2,2'
      ...
      posn(108,3) = 'POSCARN108,3'
      posn(109,1) = 'POSCARN109,1'
      posn(109,2) = 'POSCARN109,2'
      posn(109,3) = 'POSCARN109,3'
*
*   read file from CONTCAR
*
      pick = 'CONTCAR'
      OPEN(UNIT=1000,FILE=pick,ACCESS='SEQUENTIAL',FORM='FORMATTED')
      read(1000,104) heading
      read(1000,*) alat
      read(1000,*)(ax(i),ay(i),az(i),i=1,3)
      write(*,105) 'Please give input number of species: '
      read(*,*) typ
      read(1000,*)(n(i),i=1,typ,1)
      atom = 0
      do i=1,typ
      atom = atom + n(i)
      enddo
```

```

write(*,*)'Total atom:',atom
read(1000,'(a)') lattype
if (lattype.NE.'C'.and.lattype.NE.'c') then
write(*,*) 'ERROR The input file is not Cartesian type!!!'
write(*,*) 'Please use vaspD2C to convert CONTCAR first!'
endif
read(1000,*) (x(i),y(i),z(i),i=1,atom)
CLOSE(UNIT=1000)
* END of read file from CONTCAR
write(*,105) 'Please put your small change: '
read(*,*) step
do i=1,atom
xp(i) = x(i) + step
xn(i) = x(i) - step
yp(i) = y(i) + step
yn(i) = y(i) - step
zp(i) = z(i) + step
zn(i) = z(i) - step
enddo

*
*
*
make matrix -- perturb in + B and - Cstep --
s =1
19 IF (s.LE.atom) then
B(s,1) = xp(s)
B(s,2) = yp(s)
B(s,3) = zp(s)
C(s,1) = xn(s)
C(s,2) = yn(s)
C(s,3) = zn(s)
s = s + 1
go to 19
endif

*
* Make POSCAR in + STEP
do s=1,atom
k = 1
*----- make matrix -- don't perturb --
20 IF (k.LE.atom) THEN
A(k,1) = x(k)
A(k,2) = y(k)
A(k,3) = z(k)
k = k + 1
go to 20
END IF
*-----

21 l = 1
if (l.LE.atom) then
l = l + 1
go to 21
end if

do t=1,3
22 k = 1
IF (k.LE.atom) THEN
A(k,1) = x(k)
A(k,2) = y(k)
A(k,3) = z(k)
k = k + 1
go to 22
END IF
pick = posp(s,t)
A(s,t) = B(s,t)
OPEN(UNIT=1002,FILE=pick,ACCESS='SEQUENTIAL',FORM='FORMATTED')

write(1002,104) heading
write(1002,101) alat
write(1002,101) (ax(i),ay(i),az(i),i=1,3)
write(1002,102) (n(i),i=1,typ,1)
write(1002,106) 'CARTESIAN-by-vaspD2C'
do p=1,atom
write(1002,101) (A(p,q),q=1,3)

```

```

                                enddo
                                Close(UNIT=1002)
                                enddo
                                enddo

* Make POSCAR in - STEP
do s=1,atom
  k = 1
*-----
  30   make matrix -- don't perturb --
      IF (k.LE.atom) THEN
          A(k,1) = x(k)
          A(k,2) = y(k)
          A(k,3) = z(k)
          k = k + 1
      go to 30
      END IF
*-----
      l = 1
  31   if (l.LE.atom) then
          l = l + 1
          go to 31
      end if

      do t=1,3
          k = 1
  32   IF (k.LE.atom) THEN
          A(k,1) = x(k)
          A(k,2) = y(k)
          A(k,3) = z(k)
          k = k + 1
          go to 32
          END IF
      pick = posn(s,t)
      A(s,t) = C(s,t)
      OPEN(UNIT=1005,FILE=pick,ACCESS='SEQUENTIAL',FORM='FORMATTED')

          write(1005,104) heading
          write(1005,101) alat
          write(1005,101) (ax(i),ay(i),az(i),i=1,3)
          write(1005,102) (n(i),i=1,typ,1)
          write(1005,106) 'CARTESIAN-by-vaspD2C'
          do p=1,atom
              write(1005,101) (A(p,q),q=1,3)
          enddo
      Close(UNIT=1005)
      enddo
  enddo

* format for writting
101 format(3f22.15)
102 format(6I7)
103 format(a20)
104 format(a80)
105 format(A\ )
106 format(a20)
      end

```

Table A.2 The Fortran codes used for constructing the dynamic matrix.

```

*   Written by Mr.Jiraroj T-Thienprasert
      program vaspInfraredMatrix
*   This programe is used to get position and force and construct effective charge
*   matrix of each atom from OUTCAR file
*
      implicit none
      integer typemax,nmax,tota,numf,speci,num
      parameter(typemax=10,nmax=30000)
      integer i,typ,atom,n(typemax),p,j,k,o,q

```

```

real*8 ax(3),ay(3),az(3),step,lallt,mass,Mas(nmax)
double precision alat, xp(nmax), yp(nmax), zp(nmax), xn(nmax)
.,FPy(nmax),FPz(nmax),yn(nmax),zn(nmax),FNx(nmax),FNy(nmax)
.,FNz(nmax),FPx(nmax),Fax(nmax),Fay(nmax),Faz(nmax),kx(nmax)
.,ky(nmax),kz(nmax),DYN(400,400),Masss(nmax),Mac(400,400)
.,DYNAMIC(400,400)
double precision none
character*80 heading,pick3
character*10 pick
character*1 latttype
character*10 pick2,name,Nam(nmax)
*
* read file
*
write(*,*) '!!! YOU MUST HAVE "OUTCAR-P" and "OUTCAR-N" !!!'
*----- read file from "OUTCAR-P"
pick = 'OUTCAR-P'
OPEN(UNIT=1000,FILE=pick,ACCESS='SEQUENTIAL',FORM='FORMATTED')

write(*,105) 'Please put your Total atom : '
read(*,*) tota
numf = tota*3
write(*,105) 'Please put Step change (0.01,0.02 or ...) : '
read(*,*) step
write(*,105) 'Please put your lattice constant : '
read(*,*) lallt
*----- this loop for number of file -----
do i=1,numf
    read(1000,103) pick2
10      IF (pick2(1:9).NE.' POSITION') THEN
        read(1000,106) pick2
        go to 10
        ENDIF
        read(1000,106) pick2
        do j=((i*tota) - (tota-1)),tota*i
            read(1000,*) xp(j),yp(j),zp(j),FPx(j),FPy(j),FPz(j)
        enddo
    enddo
CLOSE(UNIT=1000)
*
*
*----- read file from "OUTCAR-N"
pick = 'OUTCAR-N'
OPEN(UNIT=1000,FILE=pick,ACCESS='SEQUENTIAL',FORM='FORMATTED')
*----- this loop for number of file -----
do i=1,numf
    read(1000,103) pick2
11      IF (pick2(1:9).NE.' POSITION') THEN
        read(1000,106) pick2
        go to 11
        ENDIF
        read(1000,106) pick2
        do j=((i*tota) - (tota-1)),tota*i
            read(1000,*) xn(j),yn(j),zn(j),FNx(j),FNy(j),FNz(j)
        enddo
    enddo
CLOSE(UNIT=1000)
*
*
*-----Make force average-----
do i=1,numf*tota
    Fax(i) = (FPx(i) - FNx(i))/2
    Fay(i) = (FPy(i) - FNy(i))/2
    Faz(i) = (FPz(i) - FNz(i))/2
enddo
*-----Make spring constant k---
do i=1,numf*tota
    kx(i) = -Fax(i)/(step*lallt)
    ky(i) = -Fay(i)/(step*lallt)
    kz(i) = -Faz(i)/(step*lallt)
enddo

k=0

```

```

write(*,105) 'Please give input number of species : '
read(*,*) speci
do i=1,speci
write(*,111) i,'atom name , atomic mass and number of atom : '
read(*,112) name
read(*,*) mass
read(*,114) num
      do j=1,num
        k=k+1
        Mas(k) = mass
        Nam(k) = name
      end do
end do
*--- Mass and Name of each atoms-----
do i=tota+1,tota*numf
Mas(i) = Mas(i - tota)
Nam(i) = Nam(i - tota)
enddo

*-----Rearrange matrix k(spring constant)-----
o = 1
do i=1,numf
p = 1
      do j=1,tota
DYN(i,p) = kx(o)
p = p + 1
DYN(i,p) = ky(o)
p = p + 1
DYN(i,p) = kz(o)
p = p + 1
o = o + 1
      end do
end do

*-----Write new Matrix for mass-----
j = 1
DO i=1,tota
Masss(j) = Mas(i)
j = j + 1
Masss(j) = Mas(i)
j = j + 1
Masss(j) = Mas(i)
j = j + 1
END do

DO i=1,numf
do j=1,tota*3
Mac(i,j) = Masss(i)*Masss(j)
enddo
ENDDO

*-----write DYNAMIC MATRIX-----
DO i=1,numf
do j=1,tota*3
DYNAMIC(i,j) = DYN(i,j) / (SQRT(Mac(i,j)))
enddo
ENDDO

*----- write to file Data.dat-----
*
OPEN(UNIT=1001,FILE='Data',ACCESS='SEQUENTIAL',FORM='FORMATTED
.')
write(1001,108) 'POSITION-P','FORCE-P','POSITION-N','FORCE-N'
Write(1001,107) (Nam(i),xp(i),yp(i),zp(i),FPx(i),FPy(i),FPz(i)
.,xn(i),yn(i),zn(i),FNx(i),FNy(i),FNz(i),i=1,numf*tota)
write(1001,*) ' '
write(1001,109) 'FORCE-Average','k-spring'
Write(1001,110) (Nam(i),Fax(i),Fay(i),Faz(i),kx(i),ky(i),kz(i),i=1
.,numf*tota)
Close(UNIT=1001)
*
*----- write DYNAMIC MATRIX to file DYNAMIC.dat-----
OPEN(UNIT=1010,FILE='Data2',ACCESS='SEQUENTIAL',FORM='FORMATTED

```

```

.')
  OPEN(UNIT=1011,FILE='Dynamic-matrix',ACCESS='SEQUENTIAL',FORM=
.'FORMATTED')
  write(1010,105) 'Written by Jiraroj T.thenprasert '
  write(1010,105) ' '
  write(1010,105) 'spring constant '
  do i=1,numf
  write(1010,116) (DYN(i,j),j=1,tota*3)
  enddo
  write(1010,*) ' '
  write(1010,105) 'Mass '
  do i=1,numf
  write(1010,116) (Mac(i,j),j=1,tota*3)
  enddo
  write(1010,*) ' '
  write(1010,105) 'DYNAMIC MATRIX '
  write(1011,'(I10)') tota*3
  do i=1,numf
  write(1010,116) (DYNAMIC(i,j),j=1,tota*3)
  write(1011,116) (DYNAMIC(i,j),j=1,tota*3)
  enddo
  Close(UNIT=1010)
  Close(UNIT=1011)

*
*----- format for writting-----
*
  101 format(3f20.6)
  102 format(7(I4,1X))
  103 format(a20)
  104 format(a50)
  105 format(A)
  106 format(a10)
  107 format(a3,2x,f12.6,2x,f12.6,2x,f12.6,2x,f12.6,2x,f12.6,2x,f12.6,2x,f12.6,2x,f12.6,2x,f12.6,2x,f12.6,2x,f12.6)
  108 format(22x,A,33x,A,34x,A,33x,A)
  109 format(21x,A,31x,A)
  110 format(a3,2x,f12.6,2x,f12.6,2x,f12.6,2x,f12.6,2x,f12.6,2x,f12.6)
  111 format(5x,I2,1x,A)
  112 format(A3)
  113 format(f)
  114 format(i4)
  115 format(A3,5x,f12.5)
  116 format(300(2x,f15.8))
  end

```

Table A.3 The Fortran codes used for solving the dynamic matrix.

```

  Programe LVM calculation of fulldynamic matrix
**  written by Jiraroj T thenprasert
  real*8 factor
  parameter (factor=521.471)
  INTEGER NP,INFO,LDA,LDVL,LDVR,LWORK
  character*15 pick,reply
  PARAMETER(NP=800,iopt=1,naux=800,lda=np,ldvl=np,ldvr=np)
  parameter(LWORK=5*NP)
  real*8 wn(NP),wr(NP),wi(NP),VL(NP,NP),VR(NP,NP),WORK(NP)
  real*8 zn(NP,NP)
  INTEGER i,j,nrot,kk,ik,n,DataNum,ig,ij,ia
  REAL*8 d(NP),v(NP,NP),c(NP,NP),Mpure(NP,NP),MUnPure(NP,NP),
  .EV(NP),EVEC(NP,NP),SUM1,SUM2,delta(NP),ppure(NP,NP),Pos(NP)
  .,dd(NP),vv(NP,NP),srr(NP),eev(NP),Pos2(NP),eev2(NP),srrr(NP)
  .,eigen(NP,NP),x(NP),Charge(NP,NP),Infra(NP),sum,summ,Ram(NP)
  .,Raman(NP,NP),omegai,freq,Inf(NP,NP) !!!
  logical ldum(NP)
  real*8 aux(naux)
*****
***** input two files *****
*****

```

```

write(*,*) 'Put your input file name : '
read(*,*) pick

write(*,*) 'Do you want to calculate Ir and Raman (yes or No)'
read(*,*) reply

If (reply.eq.'y'.or.reply.eq.'yes') then
write(*,*) ' Put your frequency for Raman spectroscopy (nm)'
read(*,*) freq

omegai = (2.997924580E8 / 659E-9) / 30E9
write(*,'(a19,f10.4)') 'Frequency in cm-1: ', omegai

endif

OPEN(UNIT=1000,FILE=pick,ACCESS='SEQUENTIAL',FORM='FORMATTED')
read(1000,*) n
do i=1,n
read(1000,*) (ppure(i,j),j=1,n)
enddo

CLOSE(UNIT=1000)

If (reply.eq.'y'.or.reply.eq.'yes') then
OPEN(UNIT=1000,FILE='Charge-matrix',ACCESS='SEQUENTIAL',FORM=
.'FORMATTED')
read(1000,*) n
do i=1,3
read(1000,*) (Charge(i,j),j=1,n)
enddo

CLOSE(UNIT=1000)
endif

,

*****
ccc      Lapack subroutine
      call DGEEV('N','V',n,ppure,LDA,wr,wi,VL,LDVL,
.VR,LDVR,WORK,LWORK,INFO)

      write(*,*) 'INFO',info
      do i =1,n
          d(i) = wr(i)
      enddo
      do i =1,n
      do j =1,n
          v(i,j) = vr(i,j)
      enddo
      enddo

*****
      call picksort(n,Np,d,v,dd,vv)

      Do i=1,n
      do j=1,n
          v(i,j) = vv(i,j)
      enddo
      enddo
      do i=1,n
          d(i) = dd(i)
      enddo
*****
write(*,*) 'Put your output file name : '
read(*,*) pick

do i=1,n
z=0
      do j=1,n
          if (z.lt.abs(v(j,i))) then
              z = abs(v(j,i))
              Pos(i) = j
          end if
      enddo
enddo

```



```

                                eev(i) = z
                                endif
                                enddo
                                enddo

                                If (reply.eq.'y'.or.reply.eq.'yes') then

                                do k =1,n
                                    summ = 0.0d0
                                    sum = 0.0d0
                                    do i=1,3

                                        do j=1,n

                                            sum = sum + Charge(i,j)*v(j,k)

                                        enddo
                                        Inf(k,i) = sum /(n/3)

                                        summ = summ + abs(sum*sum)
                                        sum = 0.d0
                                    enddo

                                    Infra(k) = summ/(n/3)
                                enddo

                                do k =1,n
                                    summ = 0.0d0
                                    sum = 0.0d0
                                    do i=1,3

                                        do j=1,n

                                            sum = sum + Charge(i,j) / v(j,k)

                                        enddo

                                        summ = summ + abs(sum*sum)
                                        sum = 0.d0
                                    enddo

                                    Ram(k) = summ
                                enddo
                                endif

                                *****
                                ***** OUTPUT two files *****
                                *****
                                OPEN(UNIT=1000,FILE='check.txt',ACCESS='SEQUENTIAL',FORM='FORMATTED')

                                write(1000,*) ' Eigenvalues and Eigenvector Calculation written by
                                . MR.Jiraroj T.theinprasert '
                                write(1000,*) ' '
                                do i=1,n
                                    write(1000,'(a,2x,f10.5,2x,f10.5,a,f10.5,a,f10.5)') ' Eigenvalues
                                .:',d(i),sqrt(
                                .Abs(d(i)))*factor,' POST ; ',Pos(i),' Eigenvector',eev(i)
                                enddo

                                CLOSE(UNIT=1000)

                                OPEN(UNIT=1000,FILE=pick,ACCESS='SEQUENTIAL',FORM='FORMATTED')
                                OPEN(UNIT=1001,FILE='check2.txt',ACCESS='SEQUENTIAL',FORM='FORMATTED')
                                write(1000,*) ' Eigenvalues and Eigenvector Calculation written by
                                . MR.Jiraroj T.theinprasert '
                                write(1000,*) ' '
                                do i=1,n
                                    ik = 1
                                    do j=1,n/3
                                        srr(ik) = v(ik,i)**2 + v(ik+1,i)**2 +v(ik+2,i)**2
                                        srr(ik+1) = v(ik,i)**2 + v(ik+1,i)**2 +v(ik+2,i)**2
                                        srr(ik+2) = v(ik,i)**2 + v(ik+1,i)**2 +v(ik+2,i)**2

```

```

ik = ik + 3
enddo
do ig=1,n
  do jg=1,n
    eigen(ig,jg) = v(ig,jg)
  enddo
enddo

do ig=1,n
  x(ig) = ig
enddo

ik = 1
do j=1,n,3
  srrr(ik) = srr(j)
  ik = ik + 1
enddo
zz = 0
do jj=1,n
  if (zz.lt.abs(srrr(jj))) then
    zz = abs(srrr(jj))
    Pos2(i) = jj
    eev2(i) = zz
  endif
enddo

write(1000,*) ' -----'
write(1000,'(a,2x,f10.5,2x,f10.5,a,f10.5)') ' Eigenvalues :',d(i),sqrt(
.Abs(d(i)))*factor,' POST ; ',Pos2(i)
write(1000,*) ' Eigenvectors :          '
write(1001,'(a,2x,f10.5,2x,f10.5,a,f10.5,a,f10.5)') ' Eigenvalues
.:',d(i),sqrt(
.Abs(d(i)))*factor,' POST ; ',Pos2(i),' Eigenvector',eev2(i)

write(1000,'(a5,400(2x,f10.5))') 'atom',(x(j),j=1,n/3)
write(1000,'(a5,400(2x,f10.5))') 'Ex',(eigen(j,i),j=1,n,3)
write(1000,'(a5,400(2x,f10.5))') 'Ey',(eigen(j,i),j=2,n,3)
write(1000,'(a5,400(2x,f10.5))') 'Ez',(eigen(j,i),j=3,n,3)
write(1000,*) 'Sum square'
write(1000,'(a5,400(2x,f10.5))') 'Sum',(eigen(ia,i)**2 +
.eigen(ia+1,i)**2 + eigen(ia+2,i)**2 ,ia=1,n,3)
write(1000,*) ' -----'
enddo
write(1000,*) ' '
CLOSE(UNIT=1001)
CLOSE(UNIT=1000)

If (reply.eq.'y'.or.reply.eq.'yes') then

  OPEN(UNIT=1000,FILE='Infrared-Graph',ACCESS='SEQUENTIAL',
.FORM='FORMATTED')

  write(1000,*) '# Eigenvalues and Infrared intensity Calculation
.written by MR.Jiraroj '
  write(1000,*) '#   Eigenvalues      and      Intensity (IR) X  Y  Z
. SUM^2  1/SUM^2'
  write(1000,*) ' '
  do i=1,n
    write(1000,'(2x,f10.5,2x,f25.7,2x,f25.7,2x,f25.7,2x,f25.7,2x,f25.7)')
.sqrt(Abs(d(i)))*factor,
.Inf(i,1),Inf(i,2),Inf(i,3),infra(i), 1.d0/infra(i)
  enddo

  OPEN(UNIT=1000,FILE='Raman-graph',ACCESS='SEQUENTIAL',
.FORM='FORMATTED')
  write(1000,*) '# Eigenvalues and Infrared intensity Calculation
.written by MR.Jiraroj '
  write(1000,*) '#   Eigenvalues      and      Intensity (IR)'
  write(1000,*) ' '
  do i=1,n
    write(1000,'(2x,f10.5,2x,E25.7)') sqrt(Abs(d(i)))*factor,

```

```

.Ram(i)*(omegai - sqrt(Abs(d(i)))*factor)**4
./ (sqrt(Abs(d(i)))*factor)
  enddo

endif

write(800,*) ' Eigenvector Calculation written by
. MR.Jiraroj T.theinprasert '
write(800,*) n
write(800,'(300(2x,f10.4))') (sqrt(Abs(d(i)))*factor,i=1,n)
do i=1,n
write(800,'(300(2x,f10.7))') (v(i,j),j=1,n)
enddo

write(800,*) ' '
CLOSE(UNIT=1000)
CLOSE(UNIT=800)

end

*****
SUBROUTINE picksort(n,NP,d,v,dd,vv)
implicit real*8 (a-h,o-z)
INTEGER NnP
PARAMETER(NnP=800)
real*8 d(NnP),v(NnP,NnP),dd(NnP),vv(NnP,NnP),vvv(NnP,NnP)

Do i=1,n
do j=1,n
    vvv(i,j) = v(i,j)
enddo
enddo

is =1
DO j =1,n
i = 0
ick = i
ddl = 0.d0
10 i = i + 1
dd2 = v(j,i)

IF (i.gt.n) then
go to 20
end if

If (abs(dd2).gt.abs(dd1)) then

ddl =dd2
ick = i

endif
go to 10

20 Do jj=1,n
    vv(jj,is) = vvv(jj,ick)
    enddo
    dd(is) = d(ick)
*****clear*****
Do jj=1,n
    v(jj,ick) = 0.d0
enddo
*****
is = is + 1
end do

return
end

```

APPENDIX B

UTILITY SCRIPTS FOR VASP AND FEFF CODES

In our work, a supercell approach is extensively used to calculate the defects or impurities in the crystal. Therefore, we have created our own script that can be used to generate a supercell from a unit cell, as shown in Table B.1. The script takes a unit cell file in VASP format (POSCAR) and generates a supercell in the same format. To calculate x-ray absorption, a cluster instead of a repeated supercell is needed for FEFF codes. Hence, we generate a cluster from a supercell relaxed by VASP codes by using our programs in Table B.2.

Table B.1 The Python script used for constructing a supercell.

```
#!/usr/bin/python
#
import sys, os, re
if len(sys.argv) < 2:
    print ""
Usage: vaspSupercellxyz.py <input filename>

This script convert VASP position file format (CONTCAR, POSCAR) to xyz
and extend in x, y and z direction for making CONTCAR.supercell
"""
    sys.exit()

infile=open('%s' %sys.argv[1],'r')
head=infile.readline().strip()
alat=float(infile.readline().strip())

ai=[]
bi=[]
ci=[]
for i in range(3):
    a_i=infile.readline().split()
    ai.append(a_i)
for i in range(3):
    for j in range(3):
        ai[i][j]=float(ai[i][j])
# comment the tranlation vector
# ai[0][0] ai[0][1] ai[0][2]
# ai[1][0] ai[1][1] ai[1][2]
# ai[2][0] ai[2][1] ai[2][2]
num=infile.readline().split()
```

```

num2=[]
typ=len(num)
total=0
for i in range(typ):
    num[i]=int(num[i])
    total=total+num[i]

DC=infile.readline().strip()
if DC[0] == 'D' or DC[0] == 'd':
    print "input file in Direct"

    for i in range(total):
        b_i=infile.readline().split()
        ci.append(b_i)
    for i in range(total):
        atmx = alat * ( float(ci[i][0])*ai[0][0] + float(ci[i][1])*ai[1][0] +
float(ci[i][2])*ai[2][0] )
        atmy = alat * ( float(ci[i][0])*ai[0][1] + float(ci[i][1])*ai[1][1] +
float(ci[i][2])*ai[2][1] )
        atmz = alat * ( float(ci[i][0])*ai[0][2] + float(ci[i][1])*ai[1][2] +
float(ci[i][2])*ai[2][2] )
        bi.append((atmx,atmy,atmz))
else:
    print "input file in Cartesian"
    for i in range(total):
        b_i=infile.readline().split()
        ci.append(b_i)
    for i in range(total):
        atmx = alat * float(ci[i][0])
        atmy = alat * float(ci[i][1])
        atmz = alat * float(ci[i][2])
        bi.append((atmx,atmy,atmz))

#-----#
# for extending in direction x, y and z
#-----#
name=[]
for i in range(1,typ+1):
    text=str(raw_input((" Enter the name of species no. %d : " % i)))
    for j in range(num[i-1]):
        name.append(text)
extend=[]
for i in ("x","y","z"):
    ex=int(raw_input((" Enter number for extending in direction %s : " % i)))
    extend.append(ex)

atom=[]

for i in range(typ):
    n2=str(num[i]*extend[0]*extend[1]*extend[2])
    num2.append(n2)
print num2
#-----#
outname = 'contcar.xyz'

outfile=open('%s' %outname,'w')
outfile.write(' %d\n' % (total*extend[0]*extend[1]*extend[2]))
outfile.write('%s\n' % head)
for i in range(extend[0]):
    for j in range(extend[1]):
        for k in range(extend[2]):
            for m in range(total):

                outfile.write('%s %20.15f %20.15f %20.15f\n' %(name[m],bi[m][0] +
alat*(i*ai[0][0]+j*ai[1][0]+k*ai[2][0]), bi[m][1] +
alat*(i*ai[0][1]+j*ai[1][1]+k*ai[2][1]), bi[m][2] +
alat*(i*ai[0][2]+j*ai[1][2]+k*ai[2][2])))
outfile.close()

outname = 'pick'

outfile=open('%s' %outname,'w')

```

```

outfile.write(' %d\n' % (total*extend[0]*extend[1]*extend[2]))
outfile.write('%s\n' % head)
for i in range(extend[0]):
    for j in range(extend[1]):
        for k in range(extend[2]):
            for m in range(total):

outfile.write('%s %20.15f %20.15f %20.15f\n' %(name[m],bi[m][0]/alat +
(i*ai[0][0]+j*ai[1][0]+k*ai[2][0]), bi[m][1]/alat + (i*ai[0][1]+j*ai[1][1]+k*ai[2][1]),
bi[m][2]/alat + (i*ai[0][2]+j*ai[1][2]+k*ai[2][2])))
outfile.close()
print '-----'
#-----#
#           Making file for supercell           #
#-----#
outname = 'CONTCAR.supercell'
outfile=open('%s' %outname,'w')
outfile.write('%s\n' %head)
outfile.write(' %17.15f\n' % alat)
outfile.write(' %17.15f %17.15f %17.15f\n' %
(extend[0]*ai[0][0],extend[0]*ai[0][1],extend[0]*ai[0][2]))
outfile.write(' %17.15f %17.15f %17.15f\n' %
(extend[1]*ai[1][0],extend[1]*ai[1][1],extend[1]*ai[1][2]))
outfile.write(' %17.15f %17.15f %17.15f\n' %
(extend[2]*ai[2][0],extend[2]*ai[2][1],extend[2]*ai[2][2]))
outfile.write(' %s\n' % (" " .join(num2)))
outfile.write('Cartesian-by-Jiraroj\n')

outfile2 = open('pick','r')
text = outfile2.read()
outfile2.close()
pick2=[]
k=0
for i in range(typ):
    print name[k]
    match = re.findall("%s\s*[-?]\d*\.\d*\s*[-?]\d*\.\d*\s*[-?]\d*\.\d*" %name[k],text)
    k = k + num[i]
    pick2.append(match)
outname = 'pick3'

outfile2=open('%s' %outname,'w')
for i in range(typ):
    for j in range(num[i]*extend[0]*extend[1]*extend[2]):
        outfile2.write("%s\n" % pick2[i][j])

outfile2.close()

outfile.close()

os.system(''awk '{print " %2" %$2" %3" %4}' pick3 >> CONTCAR.supercell''')
os.system("rm -f pick pick3")

```

Table B.2 The Python script and Fortran program used for constructing a cluster.

```

#!/usr/bin/python
import sys, os, re
if len(sys.argv) < 4:
    print ""
Usage: vasp2feff.py <input filename> <radius to grep> <absorber number>

This script used to convert VASP position file format (CONTCAR, POSCAR) to feff.inp

"""
sys.exit()
radius = float(sys.argv[2])
absorb = int(sys.argv[3])

infile=open('%s' %sys.argv[1],'r')

```

```

head=infile.readline().strip()
alat=float(infile.readline().strip())
ai=[]
bi=[]
ci=[]
for i in range(3):
    a_i=infile.readline().split()
    ai.append(a_i)
for i in range(3):
    for j in range(3):
        ai[i][j]=float(ai[i][j])
# comment the tranlation vector
# ai[0][0] ai[0][1] ai[0][2]
# ai[1][0] ai[1][1] ai[1][2]
# ai[2][0] ai[2][1] ai[2][2]
num=infile.readline().split()
num2=[]
typ=len(num)
total=0
for i in range(typ):
    num[i]=int(num[i])
    total=total+num[i]

DC=infile.readline().strip()
if DC[0] == 'D' or DC[0] == 'd':
    print "input file in Direct"

    for i in range(total):
        b_i=infile.readline().split()
        ci.append(b_i)
    for i in range(total):
        atmx = alat * ( float(ci[i][0])*ai[0][0] + float(ci[i][1])*ai[1][0] +
float(ci[i][2])*ai[2][0] )
        atmy = alat * ( float(ci[i][0])*ai[0][1] + float(ci[i][1])*ai[1][1] +
float(ci[i][2])*ai[2][1] )
        atmz = alat * ( float(ci[i][0])*ai[0][2] + float(ci[i][1])*ai[1][2] +
float(ci[i][2])*ai[2][2] )
        bi.append((atmx,atmy,atmz))
else:
    print "input file in Cartesian"
    for i in range(total):
        b_i=infile.readline().split()
        ci.append(b_i)
    for i in range(total):
        atmx = alat * float(ci[i][0])
        atmy = alat * float(ci[i][1])
        atmz = alat * float(ci[i][2])
        bi.append((atmx,atmy,atmz))
#-----#
# for extending in direction x, y and z
#-----#
name=[]
for i in range(1,typ+1):
    text=str(raw_input(" Enter the name of species no. %d : " % i))
    for j in range(num[i-1]):
        name.append(text)
extend=[]
for i in ("x","y","z"):
    ex=int(raw_input(" Enter number for extending in direction %s : " % i))
    extend.append(ex)

atom=[]

for i in range(typ):
    n2=str(num[i]*extend[0]*extend[1]*extend[2])
    num2.append(n2)
print num2
#-----#
outname = 'contcar.xyz'

outfile=open('%s' %outname,'w')
outfile.write(' %d\n' % (total*extend[0]*extend[1]*extend[2]))
outfile.write('%s\n' % head)

```



```

out.write('%d\n' %total)
out.write('%d\n' %absorb)
out.write('%f\n' %radius)
out.close()

os.system("vaspCONTCAR2feff < input")
os.system("sort -n -k 6 tmp.xyz > tmp2.xyz")
os.system("cat tmp2.xyz >> feff.inp")
os.system("echo 'END' >> feff.inp")
os.system("rm -f tmp.xyz tmp2.xyz input CONTCAR.supercell contcar.xyz")

```

```

Program vaspCONTCAR2feff
** Original written by Jiraroj T theinprasert
** Absorption must be in the first position

implicit real*8 (a-h,o-z)
integer pick,iatm(10)
parameter (nmax=999999)
real*8 x(nmax),y(nmax),z(nmax),xx(nmax),yy(nmax),zz(nmax),dis(nmax)
character*50 comment
character*2 typ(nmax),typ2(nmax),text(10)
pi = 4.d0*DATAN(1.d0)

write(*,*) '-----'
write(*,*) 'Please give input total atom !!! not extending !!!'
read(*,*) natom
write(*,*) 'Which atom do want to be an absorber ?'
read(*,*) iba
write(*,*) 'Input the radius to grep the atom'
read(*,*) radius

open(UNIT=8,FILE='contcar.xyz',ACCESS='SEQUENTIAL',
     .FORM='FORMATTED')
read(8,*) tota
read(8,*) comment

do i=1,tota
read(8,*) typ(i),x(i),y(i),z(i)
enddo

CLOSE(UNIT=8)
n = (tota - natom) / 2 + iba
write(*,*) 'Total Cluster atom:',tota
write(*,*) 'Original atom:',natom
write(*,*) 'Moving to number: ',n

num = 1

typ2(num) = typ(n)
xx(num) = x(n)
yy(num) = y(n)
zz(num) = z(n)
dis(num) = 0.000d0
write (*,*) 'Scatterign atoms: ',typ2(1)
write(*,*) '      x          y          z'
write(*,'3(f10.5,3x)') xx(1),yy(1),zz(1)
do i=1,tota

dist = sqrt( (x(i)-x(n))**2 + (y(i)-y(n))**2 + (z(i)-z(n))**2 )
if ( dist.le.radius.and.dist.gt.0.2 ) then
num = num + 1
typ2(num) = typ(i)
xx(num) = x(i)
yy(num) = y(i)
zz(num) = z(i)
dis(num) = dist
endif

enddo

```

```
text(1) = typ(1)
ntyp = 1

do i=1,natom

if (typ(i).eq.text(ntyp)) then
continue
else
ntyp = ntyp + 1
text(ntyp) = typ(i)
endif

enddo
write(*,*) '-----'
write(*,'(a24,2x,i3)') ' Total species of atom : ',ntyp

do i=1,ntyp

if (text(i).eq.'H') then
iatm(i) = 1
else if (text(i).eq.'He') then
iatm(i) = 2
else if (text(i).eq.'Li') then
iatm(i) = 3
else if (text(i).eq.'Be') then
iatm(i) = 4
else if (text(i).eq.'B') then
iatm(i) = 5
else if (text(i).eq.'C') then
iatm(i) = 6
else if (text(i).eq.'N') then
iatm(i) = 7
else if (text(i).eq.'O') then
iatm(i) = 8
else if (text(i).eq.'F') then
iatm(i) = 9
else if (text(i).eq.'Ne') then
iatm(i) = 10
else if (text(i).eq.'Na') then
iatm(i) = 11
else if (text(i).eq.'Mg') then
iatm(i) = 12
else if (text(i).eq.'Al') then
iatm(i) = 13
else if (text(i).eq.'Si') then
iatm(i) = 14
else if (text(i).eq.'P') then
iatm(i) = 15
else if (text(i).eq.'S') then
iatm(i) = 16
else if (text(i).eq.'Cl') then
iatm(i) = 17
else if (text(i).eq.'Ar') then
iatm(i) = 18
else if (text(i).eq.'K') then
iatm(i) = 19
else if (text(i).eq.'Ca') then
iatm(i) = 20
else if (text(i).eq.'Sc') then
iatm(i) = 21
else if (text(i).eq.'Ti') then
iatm(i) = 22
else if (text(i).eq.'V') then
iatm(i) = 23
else if (text(i).eq.'Cr') then
iatm(i) = 24
else if (text(i).eq.'Mn') then
iatm(i) = 25
else if (text(i).eq.'Fe') then
iatm(i) = 26
else if (text(i).eq.'Co') then
iatm(i) = 27
```

```

else if (text(i).eq.'Ni') then
iatm(i) = 28
else if (text(i).eq.'Cu') then
iatm(i) = 29
else if (text(i).eq.'Zn') then
iatm(i) = 30
else if (text(i).eq.'Ga') then
iatm(i) = 31
else if (text(i).eq.'Ge') then
iatm(i) = 32
else if (text(i).eq.'As') then
iatm(i) = 33
else if (text(i).eq.'Se') then
iatm(i) = 34
else if (text(i).eq.'Br') then
iatm(i) = 35
else if (text(i).eq.'Kr') then
iatm(i) = 36
else if (text(i).eq.'Rb') then
iatm(i) = 37
else if (text(i).eq.'Sr') then
iatm(i) = 38
else if (text(i).eq.'Y') then
iatm(i) = 39
else if (text(i).eq.'Zr') then
iatm(i) = 40
else if (text(i).eq.'Nb') then
iatm(i) = 41
else if (text(i).eq.'Mo') then
iatm(i) = 42
else if (text(i).eq.'Tc') then
iatm(i) = 43
else if (text(i).eq.'Ru') then
iatm(i) = 44
else if (text(i).eq.'Rh') then
iatm(i) = 45
else if (text(i).eq.'Pd') then
iatm(i) = 46
else if (text(i).eq.'Ag') then
iatm(i) = 47
else if (text(i).eq.'Cd') then
iatm(i) = 48
else if (text(i).eq.'In') then
iatm(i) = 49
else if (text(i).eq.'Sn') then
iatm(i) = 50
else if (text(i).eq.'Sb') then
iatm(i) = 51
else if (text(i).eq.'Te') then
iatm(i) = 52
else if (text(i).eq.'I') then
iatm(i) = 53
else if (text(i).eq.'Xe') then
iatm(i) = 54
else if (text(i).eq.'Cs') then
iatm(i) = 55
else if (text(i).eq.'Ba') then
iatm(i) = 56
else if (text(i).eq.'La') then
iatm(i) = 57
else if (text(i).eq.'Ce') then
iatm(i) = 58
endif

write(*,'(a11,2x,i3,2x,i3,2x,a2)') ' Species : ',i,iatm(i),text(i)
enddo
write(*,'(a16,2x,a2)') ' Absorber atom : ',typ2(1)

```

```

***** Check *****
open(UNIT=8,FILE="contcar_Grep.xyz",ACCESS='SEQUENTIAL',
.FORM='FORMATTED')

```

```

open(UNIT=9,FILE="feff.inp",ACCESS='SEQUENTIAL',
     .FORM='FORMATTED')
open(UNIT=11,FILE="tmp.xyz",ACCESS='SEQUENTIAL',
     .FORM='FORMATTED')

write(9,'(a)') ' * This feff.inp file generated by MR.
               .Jiraroj T.theinprasert'
write(9,'(a)') ' TITLE    As-doped ZnO'
write(9,'(a)') ' EDGE      K'
write(9,'(a)') ' S02       1.0'
write(9,'(a)') ' CONTROL   1      1      1      1      1      1'
write(9,'(a)') ' PRINT     1      0      0      0      0      0'
write(9,'(a)') ' *         r_scf   [ l_scf  n_scf  ca ]'
write(9,'(a)') ' SCF       5.500   0      30     0.1'
write(9,'(a)') ' *         ixc    [ Vr   Vi   '
write(9,'(a)') ' EXCHANGE  0      0   0.5'
write(9,'(a)') ' *         kmax   [ delta_k  delta_e ]'
write(9,'(a)') ' XANES     6.0     0.07   0.5'
write(9,'(a)') ' *         r_fms   [ l_fms ]'
write(9,'(a)') ' '
write(9,'(a)') ' FMS       8.400    0'
write(9,'(a)') ' RPATH     0.10000'
write(9,'(a)') ' * LDOS      -20   20   0.2'
write(9,'(a)') ' POTENTIALS'
write(9,'(a)') ' *      ipot   z [ label  l_scm  l_fms ]'

do i=1,ntyp
if (typ2(1).eq.text(i)) then
write(9,'(a8,2x,i3,3x,a3,a15)') '          0',iatm(i),text(i),
.'          -1          -1'
endif
enddo

do i=1,ntyp
write(9,'(a7,i1,2x,i3,3x,a3,a15)') '          ',i,iatm(i),text(i),
.'          -1          -1'
enddo
write(9,'(a)') ' '
write(9,'(a)') ' ATOMS'

ipot = 0

write(9,'(3(4x,f15.10),4x,i2,4x,a2,4x,f15.10)') xx(1)-xx(1),yy(1)-
.yy(1),zz(1)-zz(1),ipot,typ2(1),dis(1)
do i=2,num

do j=1,ntyp
if (typ2(i).eq.text(j)) then
ipot = j
endif
enddo

write(11,'(3(4x,f15.10),4x,i2,4x,a2,4x,f15.10)') xx(i)-xx(1),yy(i)-
.yy(1),zz(i)-zz(1),ipot,typ2(i),dis(i)
enddo

write(8,*) num
write(8,*) comment
do i=1,num
write(8,'(a2,3(4x,f15.10)') typ2(i),xx(i)-xx(1),yy(i)-
.yy(1),zz(i)-zz(1)
enddo
CLOSE(UNIT=11)
CLOSE(UNIT=8)
CLOSE(UNIT=9)
*****

end

```

APPENDIX C

FEFF CODES

C.1 Parameters in FEFF Codes

X-ray photo-absorption cross section can be calculated using the full multiple scattering (MS) scheme in the framework of the muffin-tin potential which is implemented in FEFF codes. The exchange-correlation part of the potential is determined based on the local density approximation.

The input file for FEFF codes can be either manually or automatically generated. The latter is obtained using the “*atoms codes*”, which is written by Bruce Ravel. To use *atoms codes*, we have to create an input file, whose name is “*atom.inp*”. This file is composed of some parameters, as shown in Table C.1.

In FEFF codes, there are several parameters that can be adjusted. Therefore, we give only a brief detail of important parameters that are generally used in FEFF codes to simulate the XANES and EXAFS spectra. These parameters in the FEFF codes are called CARD. Some importance CARDS are described below.

- **ATOMS CARD**

This card is used to specify the absorbing atom and the crystal structure for the system under study.

- **EDGE CARD** *label*

Table C.1 An example input file for the *atoms code* used to generate the input file for the FEFF codes.

```

title Perovskite BaTiO3
space P M 3 M
rmax=8.0      a=3.9638      core Ba
atom
Ba   0.0   0.0   0.0
Ti   0.5   0.5   0.5
O    0.0   0.5   0.5

```

This card is used to select the absorption shell, for example *K* means *K*-shell, *L*₁ means *L*₁-shell, etc.

- **EXCHANGE** *ixc* [*V_r* *V_i*]

This card is used to specify the energy dependent exchange correlation potential that is used for the fine structure and the atomic background calculations. Generally, we used *ixc* = 0 (Hedin-Lundquist), *V_r*=0, and *V_i*= experimental broadening.

- **EXAFS** [*xkmax*]

The maximum value of *k* for EXAFS calculation is set by *xkmax*.

- **FMS** *r_fms*

The radius of the full multiple scattering calculations is specified by *r_fms* for the calculations of XANES spectra.

- **SCF** *r_scf* [*l_scf* *n_scf* *ca*]

This card is used to control the self-consistent potential calculations. FEFF uses the Broyden algorithm self-consistency. As a result, the convergence accelerator

factor (*ca*) for the first iteration is needed. The radius of the cluster for full multiple scattering is specified by *r_scf* for self-consistency calculations and *n_scf* is used to give a maximum number of self-consistency potential calculations.

- **XANES** [*xkmax* *xkstep* *estep*]

This card is used for the XANES calculations. The maximum *k* value of XANES spectra in the reciprocal space is specified by *xkmax* with the step size of *xkstep* far from the edge and the energy step of the grid at edge is *estep*.

C.2 Calculations of XANES and EXAFS Spectra

There are some important parameters that need special attentions before doing the calculation of XANES or EXAFS spectra. These parameters are the radius of the self-consistency potential calculation (SCF) and the full multiple scattering (FMS) included in our calculation.

In this section, we showed the test case of the calculations of Cl *K*-edge XANES spectra by using different SCF and FMS radius to calculate XANES spectra (Figure C.1). We can see that our calculation test is converged, if we choose the radius of SCF and FMS more than 4.0 Å and 8.0 Å, respectively. In this calculation, The Hedin-Lundqvist (HL) is used as the exchange potential with imaginary part of 0.5 eV to simulate experimental broadening. The input files used to calculate XANES and EXAFS spectra are shown in Table C.2 and Table C.3.

The x-ray energy can be converted to wave number of the photo electron *k*, which has a dimension of reciprocal space, through the equation

$$k = \sqrt{\frac{2m(E - E_0)}{\hbar^2}}, \quad (\text{C.1})$$

where E_0 is the absorption edge energy and m is the mass of electron. The EXAFS function can be written in term of k , $\chi(k)$.

In order to obtain the information of EXAFS in real-space, we calculate the Fourier transform of $\chi(k)$ by using the equation

$$\tilde{\chi}(R) = \frac{1}{\sqrt{2\pi}} \int_0^{\infty} k^n \chi(k) e^{i2kR} dk. \quad (\text{C.2})$$

The distance, coordination number, and species of the neighbor atoms can be determined by fitting with the EXAFS equation.

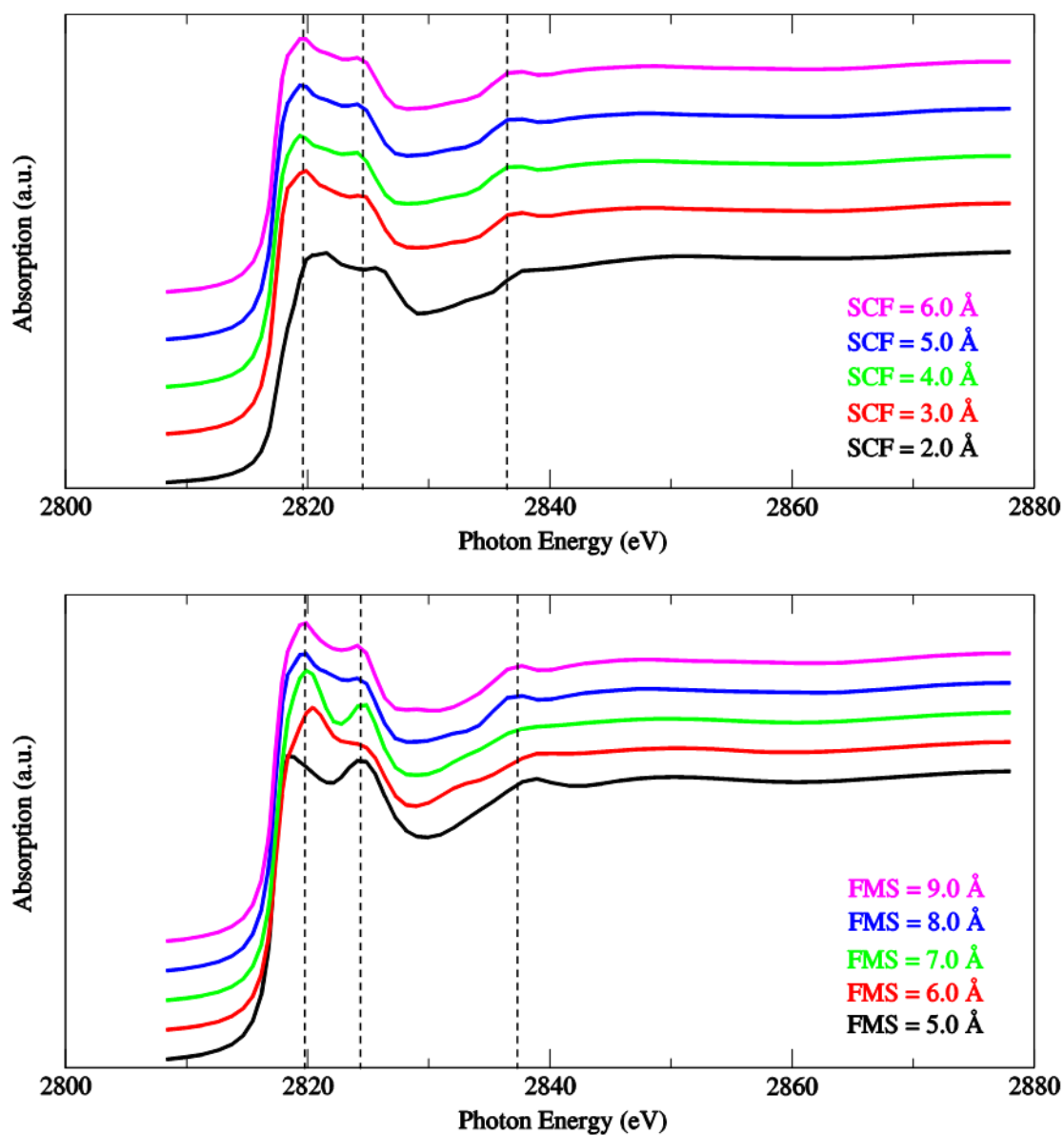


Figure C.1 The calculated XANES spectra of Cl⁻ in aqueous solution with different SCF (top) and FMS (bottom) radius.

Table C.2 An example of the input file for Cl *K*-edge XANES simulation.

```

* This feff.inp file generated by MR.Jiraroj T-Thienprasert
TITLE  Cl or K or Ca in water

EDGE   K
S02    1.0
*      pot  xsph  fms  paths  genfmt  ff2chi
CONTROL 1  1  1  1  1  1
PRINT  1  0  0  0  0  0

*      r_scf  [ l_scf  n_scf  ca ]
SCF     5.6000  0  30  0.1

*      ixc  [ Vr  Vi ]
EXCHANGE 0  0  0.5
*      kmax [ delta_k  delta_e ]
XANES   4.0  0.07  0.5
*      r_fms  [ l_fms ]
FMS     8.000  0
RPATH  0.1000
*
POTENTIALS
*  ipot  z [ label  l_scm  l_fms  stoichiometry ]
    0 17  Cl  -1  -1
    1  8  O   -1  -1
    2  1  H   -1  -1
ATOM
      XXX  XXX  XXX  0  Cl  XXX
      XXX  XXX  XXX  2  H   XXX
      XXX  XXX  XXX  1  O   XXX
      XXX  XXX  XXX  2  H   XXX

```

Table C.3 An example of the input file for Cl *K*-edge EXAFS calculation.

```

* This feff.inp file generated by MR.Jiraroj T-Thienprasert
TITLE Cl or K or Ca in water

EDGE K
S02 1.0
* pot xsph fms paths genfmt ff2chi
CONTROL 1 1 1 1 1 1
PRINT 0 0 0 0 0 0

* r_scf [ l_scf n_scf ca ]
SCF 5.600 0 30 0.1

* ixc [ Vr Vi ]
EXCHANGE 0 0 0.5

EXAFS 20
RPATH 5.0

POTENTIALS
* ipot z [ label l_scm l_fms stoichiometry ]
0 17 Cl -1 -1
1 8 O -1 -1
2 1 H -1 -1

ATOMS
XXX XXX XXX 0 Cl XXX
XXX XXX XXX 2 H XXX
XXX XXX XXX 1 O XXX
XXX XXX XXX 2 H XXX

```

APPENDIX D

PUBLICATIONS AND PRESENTATIONS

D.1 List of Publications

Zhang, L., T-Thienprasert, J., Du, M.-H., Singh, D. J., and Limpijumnong, S. (2009). Comment on “Spectroscopic Signatures of Novel Oxygen-Defect Complexes in Stoichiometrically Controlled CdSe”. **Phys. Rev. Lett.** 102: 209601.

T-Thienprasert, J., Nukeaw, J., Sungthong, A., Prontheeraphat, S., Singkarat, S., Onkaw, D., Rujirawat, S., and Limpijumnong, S. (2008). Local structure of indium oxynitride from x-ray absorption spectroscopy. **Appl. Phys. Lett.** 93: 051903.

D.2 List of Presentations (oral)

T-Thienprasert, J. and Limpijumnong, S. (October 2007). Verification of dynamic hydration-structures of Cl^- and K^+ by synchrotron x-ray absorption near-edge structures. In **the 33rd Congress on Science and Technology of Thailand**. Nakhon Si Thammarat: The Science Society of Thailand.

T-Thienprasert, J. and Limpijumnong, S. (October 2007). Infrared absorption and Raman spectra of TiO_2 by first principles calculations. In **the 33rd Congress on Science and Technology of Thailand**. Nakhon Si Thammarat: The Science Society of Thailand.

T-Thienprasert, J., Nukeaw, J., Sungthong, A., Prontheeraphat, S., Onkaw, D., Rujirawat, S., and Limpijumnong, S. (March 2009). X-ray absorption spectroscopy of

indium nitride, indium oxide, and their alloys. In **Siam Physics Congress 2009**. Phetchburi: Thai Physics Society.

D.3 List of Presentation (poster)

T-Thienprasert, J., Nukeaw, J., A. Sunghong, Van de Walle, C. G., and Limpijumnong, S. (March 2008). Determination of oxygen defect structures in CdTe from their infrared signatures. In **Siam Physics Congress 2008**. Nakhon Ratchasima: Thai Physics Society.

Comment on “Spectroscopic Signatures of Novel Oxygen-Defect Complexes in Stoichiometrically Controlled CdSe”

In a recent Letter [1] Chen *et al.* reported two groups of local vibrational modes (LVMs) observed in CdSe by infrared measurements. The first group consists of two modes, i.e., $\mu_1 = 1991.77 \text{ cm}^{-1}$ and $\mu_2 = 2001.3 \text{ cm}^{-1}$, which they assigned to oxygen on the Cd site (O_{Cd}). The second group consists of three modes, i.e., $\gamma_1 = 1094.11 \text{ cm}^{-1}$, $\gamma_2 = 1107.45 \text{ cm}^{-1}$, and $\gamma_3 = 1126.33 \text{ cm}^{-1}$, which they assigned to oxygen on the Se site (O_{Se}) in the vicinity of a Cd vacancy (V_{Cd}). For comparison the highest phonon frequencies in corundum Al_2O_3 —one of the hardest known oxides—are below 900 cm^{-1} [2]. The assignment of these LVMs to O implies effective bond stiffness ~ 5 times higher than in Al_2O_3 . Diamond with its exceptionally strong bonding and lighter atoms does not show phonons above 1350 cm^{-1} , and even the bond-stretching mode of the double covalently bonded O_2 molecule is below 1600 cm^{-1} . Frequencies above 2000 cm^{-1} are rare in solid-state compounds with the exception of covalently bonded hydrides. Here we explicitly show that these mode assignments are incorrect and suggest that the observed LVMs are related to hydrogen rather than oxygen based on detailed density functional calculations in the local density approximation. We used a plane-wave basis with cutoff energy of 400 eV and a 96-atom wurtzite supercell.

Our calculations show that O_{Cd} is located off center, binding one axial (along the c axis) and one nonaxial Se atom. The calculated LVMs for O_{Cd} are 389, 342, and 197 cm^{-1} , far lower than 2000 cm^{-1} . Furthermore, O_{Cd} is unstable against interchange of O and a neighboring Se. This results in $O_{Se}-Se_{Cd}$ (a complex of substitutional O on Se site and a Se antisite). Swapping the O and the axial Se lowers the energy by 0.96 eV for the neutral charge state of the defect complex. The neutral Se_{Cd} is also off center due to the Jahn-Teller distortion similar to Te_{Cd} in CdTe as discussed previously [3]. The calculated O LVMs in $O_{Se}-Se_{Cd}$ complex are 411, 392, and 209 cm^{-1} .

The calculated LVMs for an isolated O_{Se} are $\sim 360 \text{ cm}^{-1}$, close to the calculated (341 cm^{-1}) and measured (350 cm^{-1}) [4] LVMs for O_{Te} in CdTe. With a V_{Cd} next to O_{Se} , we find that the nonaxial V_{Cd} is more stable than the axial by only 5 meV. The O_{Se} relaxes away from the vacancy and is nearly on the basal plane of three Cd atoms. The calculated LVMs for the $O_{Se}-V_{Cd}$ (nonaxial) are 495, 494, and 201 cm^{-1} . The two higher LVMs are from in-plane vibrations and the lower LVM is from the out-of-plane vibration. These results are close to the calculated O LVMs for $O_{Te}-V_{Cd}$ in CdTe, i.e., 475 cm^{-1} (double degenerate) and 196 cm^{-1} . A modest increase in

the O_{Se} in-plane LVMs due to the nearby V_{Cd} as we find is reasonable since the Cd-O bond is slightly shortened. Chen *et al.* estimate the LVM for O_{Se} to be $350\text{--}450 \text{ cm}^{-1}$, but assign three LVMs near 1100 cm^{-1} to $O_{Se}-V_{Cd}$. This would imply that a nearby V_{Cd} can increase the O_{Se} LVMs by nearly a factor of 3, i.e., increase the Cd-O bond strength by nearly an order of magnitude, which is unlikely.

Covalently bonded H (e.g., Se-H) is a natural candidate for LVMs of $\sim 2000 \text{ cm}^{-1}$. We calculated the H LVMs for H in V_{Cd} . H can bind with either the axial or nonaxial Se atom. The former is more stable by an insignificant 3 meV. Thus, both H structures should exist. The calculated LVMs for the two H structures are 2092 cm^{-1} (nonaxial) and 2101 cm^{-1} (axial), which are in good agreement with the measured LVMs μ_1 and μ_2 . Since H in the Cd vacancy has nearly equal probability to bind with any of the four surrounding Se atoms, its host isotope fine structure should resemble that of a substitutional cation. This may explain the observation in Ref. [1] that the host isotope fine structures for μ_1 and μ_2 are similar to Mg_{Cd} in CdSe.

The three measured LVMs near 1100 cm^{-1} , γ_1 , γ_2 , and γ_3 , are very close to the two LVMs found in CdTe [4]. This suggests that these LVMs may be related to a common impurity in CdSe and CdTe. Although we have not found a satisfactory model for these LVMs, we suspect that they are related to H. The O-H wagging modes possibly explain the two LVMs near 1100 cm^{-1} in CdTe [3]. It will be helpful to have more experimental information on the impurity and defect characterization to unambiguously answer this remaining question.

Work supported by U.S. DOE NA22 and DMSE, and by TRF (BRG5180001 and PHD/0107/2548) from Thailand.

L. Zhang,¹ J. T-Thienprasert,² M.-H. Du,¹ D. J. Singh,¹ and S. Limpijumnong²

¹Oak Ridge National Laboratory
Oak Ridge, Tennessee 37831, USA
²Suranaree University of Technology
and Synchrotron Light Research Institute
Nakhon Ratchasima 30000, Thailand

Received 28 January 2009; published 18 May 2009

DOI: 10.1103/PhysRevLett.102.209601

PACS numbers: 61.72.J-, 63.20.Pw, 78.30.Fs

- [1] G. Chen, J. S. Bhosale, I. Miotkowski, and A. K. Ramdas, *Phys. Rev. Lett.* **101**, 195502 (2008).
- [2] H. Bialas and H. J. Stolz, *Z. Phys. B* **21**, 319 (1975).
- [3] M.-H. Du, H. Takenaka, and D. J. Singh, *Phys. Rev. B* **77**, 094122 (2008).
- [4] G. Chen, I. Miotkowski, S. Rodriguez, and A. K. Ramdas, *Phys. Rev. Lett.* **96**, 035508 (2006).

Local structure of indium oxynitride from x-ray absorption spectroscopy

J. T-Thienprasert,¹ J. Nukeaw,² A. Sungthong,² S. Porntheeraphat,³ S. Singkarat,⁴ D. Onkaw,¹ S. Rujirawat,¹ and S. Limpijumnong^{1(a)}¹School of Physics, Suranaree University of Technology and National Synchrotron Research Center, Nakhon Ratchasima 30000, Thailand²Nanotechnology Research Center of KMITL and Department of Applied Physics, King Mongkut's Institute of Technology Ladkrabang, Bangkok 10520, Thailand³Thai Microelectronics Center, National Electronics and Computer Technology Center, Pathumthani 12120, Thailand⁴Fast Neutron Research Facility, Faculty of Science, Chiang Mai University, Chiang Mai 50200, Thailand

(Received 23 May 2008; accepted 10 July 2008; published online 5 August 2008)

Synchrotron x-ray absorption near edge structures (XANES) measurements of In L_3 edge is used in conjunction with first principles calculations to characterize rf magnetron sputtered indium oxynitride at different O contents. Good agreement between the measured and the independently calculated spectra are obtained. Calculations show that the XANES spectra of this alloy are sensitive to the coordination numbers of the In atoms, i.e., fourfold for indium nitride-like structures and sixfold for indium oxide-like structures, but not to the substitution of nearest neighbor N by O or vice versa. © 2008 American Institute of Physics. [DOI: 10.1063/1.2965802]

Indium oxynitride can be considered as an alloy between indium nitride (InN) and indium oxide (In₂O₃). This is unlike most of the traditional semiconductor alloys in the sense that the crystal structures as well as the anion valencies of the two parent compounds are different. InN is one of the highly studied III-nitride semiconductors (GaN, AlN, and InN) because III-nitride alloys are widely used for optoelectronic applications. Despite real applications and substantial research in III-nitride materials, InN bandgap has been mistaken to be ~1.9 eV for a long time (see the discussion in Refs. 1 and 2). Only recently, the actual InN bandgap of ~0.7 eV has been realized.^{3,4} The apparently large bandgap observed in the past is most likely due to the Moss–Burstein shift caused by substantial unintentional carriers that are typical for InN grown by traditional techniques (de discharge or sputtering).^{15–7} Because InN has a (now–realized) small bandgap of ~0.7 eV and In₂O₃ has a large optical gap of ~3.6 eV,⁸ the band gap of indium oxynitride can potentially be engineered in a very wide range. This, combining with the availability of low temperature growth techniques, such as rf magnetron sputtering,⁹ make indium oxynitride a strong candidate for optical coating applications.

For alloys with low O content, it has been reported that O atoms substitute for N in the wurtzite InN crystal structure.¹⁰ However, in higher O content alloys the crystal structure remains unclear. Previously, an attempt to study indium oxynitride structures by N K-edge x-ray absorption near edge structures (XANES) has been done.¹¹ However, probing local structure of anions in this alloy system is not the most direct way because anions in both InN and In₂O₃ are fourfold coordinated. Unlike anion, the coordination number of In in the two compounds are different, i.e., it is sixfold in In₂O₃ [Fig. 1(a)] and fourfold in InN [Fig. 1(b)]. Therefore, probing the local structure of In atoms should give more direct information on the alloy structures. In this letter, the In L_3 -edge XANES is used to characterize indium oxynitride with varied compositions. The XANES has been

proven to be a powerful tool in resolving the local structures around the absorbing atoms (in this case In atoms).^{12–14}

Indium oxynitride films were grown by rf magnetron sputtering (Edwards Auto 306) at room temperature using a technique called reactive gas timing.^{15,16} The growth process started with the preevacuation of the chamber to the order of 10⁻⁵ Pa. Then N₂ and O₂ gas were flown interchangeably at the flow rate of 10 standard cubic centimeter per minute onto the 99.999% purity In target. The sputtering gas pressures were set at 0.34 and 0.32 Pa for N₂ and O₂, respectively. By controlling N₂ and O₂ gas timing, indium oxynitride samples with varied O contents were obtained. The interval of gas timing cycles used for each sample is shown in Table I and the samples are named according to the gas timing cycles. The rf plasma power was set at 100 W. All samples were grown on polyethylene terephthalate substrate to the thickness of ~1 μm (typical growth time is approximately 1 h). To measure the actual O content in each sample, the [O]:[In] ratios were determined using Auger electron spectroscopy (AES) with capability of sputter depth profiling. The O contents were found to be homogeneous throughout the film thickness. Note that AES measured O in all forms. The optical bandgaps measured by UV-visible spectroscopy were found to increase with O₂ gas timing ratio, as shown in Table I. This is consistent with the work of Yi *et al.*¹¹ that reported the increase in optical bandgap of indium oxynitride with O content. Although the optical bandgap of N30/O0 sample is

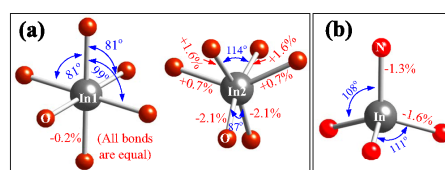


FIG. 1. (Color online) The local structure around In atoms used in the simulations of the In L_3 -edge XANES of (a) In₂O₃ and (b) InN. All bond distances are given as a percentage difference from an average In₂O₃ bond distance ($d_{cak} = 2.170$ Å).

^{a)} Author to whom correspondence should be addressed. Electronic mail: sukitt@sut.ac.th.

TABLE I. The gas timing conditions, optical bandgaps, and [O]:[In] compositions of the samples.

Sample	Gas timing (s)		Optical bandgap (eV)	[O]:[In] composition
	N ₂	O ₂		
N30/O0	30	0	1.5	0.16
N30/O5	30	5	1.6	0.43
N30/O10	30	10	1.6	0.96
N30/O20	30	20	2.4	1.08
N0/O30	0	30	3.4	1.50

larger than that of pure InN and the sample is expected to contain a few percent of unintentionally doped O, this gap widening in low O samples is most likely due to Moss-Burstein effects^{4,5-7} not the changes in the crystal structure. As will be discussed, L_3 -edge XANES of In is sensitive to the change in In coordination number but not to the interchanging between N and O. Therefore, XANES of InN with a few percent of N replaced by O are expected to be almost identical to pure InN because they are structurally the same.

The samples were characterized by In L_3 -edge XANES measurements in the fluorescent mode with a 13-component Ge detector (Canberra) at the x-ray absorption spectroscopy beamline (BL-8) of the Siam Photon Source (electron energy of 1.2 GeV, beam current 120–80 mA), National Synchrotron Research Center, Thailand. Double crystal monochromator Si (111) was used to scan the synchrotron x ray with the photon energy step of 0.25 eV in the range of 3700 to 3850 eV, covering the XANES region of In L_3 edge. The measured spectra are shown in Fig. 2(a).

In order to understand the local microscopic structure, we performed first principles In L_3 -edge XANES simulations of wurtzite InN and bixbyite In₂O₃ crystals. The detailed crystal structures were optimized based on first principles pseudopotential calculations. We used density functional theory with local density approximation and ultrasoft pseudopotentials as implemented in the VASP code.¹⁷ The cutoff energy for the plane wave basis set was set at 400 eV.

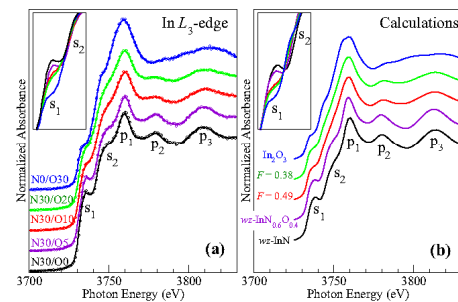


FIG. 2. (Color online) (a) Normalized In L_3 -edge XANES spectra of indium oxynitride samples prepared under different gas timing with increased O₂ timing from bottom curve to top curve. Circles show recorded data points and the curves are the (noise removed) fit to the data. Inset: the plots from the main panel without offset at the energy range near the s_1 shoulders to highlight the changes in the shoulder height. (b) The calculated In L_3 -edge XANES spectra of wurtzite InN, bixbyite In₂O₃, wurtzite InN_{0.6}O_{0.4}, and the simulated separated phase alloys with 38% and 49% fourfold In atoms (see text for detail).

We used Monkhorst–Pack k -point mesh for Brillouin zone integration ($7 \times 7 \times 7$ for InN and $3 \times 3 \times 3$ for In₂O₃). All atoms were allowed to relax until the residue forces were less than 10^{-3} eV/Å. The fully relaxed local structures surrounding In atoms are shown in Figs. 1(a) and 1(b) for In₂O₃ and InN, respectively. All In atoms in wurtzite InN crystal are equivalent. However, there are two species of In atoms in In₂O₃, labeled In1 and In2, with the composition ratio of 1:3. These structural relaxations by first principles calculations is a crucial step to obtain the computationally unstrained structures to be further used in XANES calculations.

To calculate *ab initio* XANES of InN and In₂O₃ based on the relaxed crystal structures above, we used FEFF8.2 codes.^{18,19} The codes utilize a full multiple scattering approach based on *ab initio* overlapping muffin-tin potentials. The muffin-tin potentials were obtained using self-consistent calculations with Hedin–Lundqvist exchange-correlation function. The self-consistent calculations were performed in the sphere radius 4 Å (~40 atoms) around the absorber In atom, which is more than sufficient to allow charge to fluctuate yielding realistic electron relaxations. The full multiple scattering calculations include all possible paths within a larger cluster radius of 7.4 Å (~140 atoms).

The calculated In L_3 -edge spectra of InN and In₂O₃ crystals are shown in Fig. 2(b) (bottom and top curves, respectively). For In₂O₃, because there are two species of non-equivalent In atoms, the spectrum shown is the weight averaged between the spectra from the two species. Note that the spectra obtained from the two species of In in In₂O₃ are very similar. The spectra of fourfold In in InN and sixfold In in In₂O₃ are, however, clearly different, making In L_3 -edge XANES a suitable tool to study the local structure around In atoms. Our test calculations also show that the XANES spectra of the fourfold (sixfold) In atom is not very sensitive to the substitution of a neighboring N by O (O by N).²⁰

The calculated spectra of InN and In₂O₃ are in full agreement with the measured spectra from N30/O0 and N0/O30 samples, respectively. The main features of InN XANES spectrum is composed of two shoulders and three peaks labeled as s_1 , s_2 , p_1 , p_2 , and p_3 . All five features are in a very good agreement with the corresponding features in the N30/O0 sample in both positions and shapes. Similar agreement can be found between the spectrum of N0/O30 sample and the calculated In₂O₃ spectrum. This suggests that structurally In atoms in N30/O0 are mostly fourfold (as those in InN) and in N0/O30 are mostly sixfold (as those in In₂O₃). If we compare the measured spectra of different O contents [from the bottom curve to the top curve of Fig. 2(a)], we can see that the five features are progressively evolved as O content increased. The progressive changes include: (1) the reduction in s_1 peak (for clarity, the same set of spectra without offset is shown in the inset), (2) the broadening and increase in magnitude of p_1 peak, (3) the reduction in p_2 peak, and (4) the significant broadening accompanied by a slight shift to higher energy of peak p_3 . Interestingly, the spectrum of N30/O5 (at 43% O content) is still almost perfectly overlapped with that of N30/O0 with the exception of s_1 shoulder, which is slightly reduced [see inset of Fig. 2(a)]. This indicates that most of In atoms in N30/O5 remain fourfold and O atoms are substituting on the N sites. To test this assumption, we calculated the XANES spectra for InN_{0.6}O_{0.4} alloy in the wurtzite structure [the second curve from bottom in Fig. 2(b)]. The calculated curve is almost overlapped with

that of (calculated) pure InN for the photon energy beyond the s_1 shoulder. Moreover, a small reduction in s_1 shoulder of the N30/O5 spectrum in comparison with that of N30/O0 is nicely reproduced by the $\text{In}_{0.6}\text{O}_{0.4}$ alloy simulation. The reduction in the s_1 shoulder can be attributed to the changes in the lowest conduction band states due to the replacement of N by O atoms. Note that a calculated spectrum based on a combination of fourfold and sixfold In (not shown) does not give such a good agreement. For samples with higher O contents (N30/O10 and N30/O20) the spectra show a mixed signature between that of fourfold and sixfold In atoms. The excess O atoms above the substitutional solubility limit (assumed to be ~40%) of InN can either form a phase separated In_2O_3 -like structure or an inclusion of local In_2O_3 -like structure both of which leads to a formation of sixfold In atoms. In this model, the composition in the sample can be written as $(\text{In}_{0.6}\text{O}_{0.4})_F(\text{InO}_{1.5})_{1-F}$, where F is a fraction of fourfold In atoms out of all In atoms. The value of F can be calculated using a relationship $[\text{O}]:[\text{In}]=0.4F+1.5(1-F)$, where the $[\text{O}]:[\text{In}]$ ratio of each sample was determined from AES and is shown in Table I. This gives the F values of 0.49 and 0.38 for N30/O20 and N30/O10, respectively. The corresponding spectra, which are calculated using weight averaged between $\text{In}_{0.6}\text{O}_{0.4}$ and pure In_2O_3 , are shown in Fig. 2(b). The spectra show the mixed signature of InN and In_2O_3 that are consistent with the measured spectra of N30/O10 and N30/O20. s_1 shoulder also further decreased from pure InN as more O content is added (insets of Fig. 2).

In a detail investigation, the spectra of both N30/O10 and N30/O20 samples appear to be very similar to each other and the s_1 shoulder of N30/O20 is only slightly lower than N30/O10 [see the inset of Fig. 2(a)]. The simulations also show the same trend, i.e., the s_1 shoulder of the spectrum with $F=0.38$ is just slightly lower than that of $F=0.49$ [see the inset of Fig. 2(b)]. However, when observing the decrease in s_1 shoulder in comparison to that of InN, we can see that the simulations ($F=0.38$ and $F=0.49$ spectra) give larger drop in the s_1 shoulder in comparison to those of samples N30/O10 and N30/O20. This suggests that N30/O10 and N30/O20 samples may contain more fourfold In atoms, i.e., higher F ratios, than those used in the simulations. We found that a simulation with $F \sim 2/3$, i.e., $2/3$ of In atoms are fourfold and $1/3$ of In atoms are sixfold, can provide a better agreement in the s_1 feature with the experiment (not shown). We speculate that there exist an intermediate crystal structure that have a fix number of fourfold In atoms and sixfold In atoms, in the unit cell. Although N atoms would prefer to decorate fourfold In atoms whereas O atoms would prefer sixfold In atoms, the interchanging of the anions is possible, leading to a very different optical properties in the two samples. Since the XANES signatures are not very sensitive to these anion interchanging, the spectra of the two samples remain very close. Further work is needed to settle down this issue.

In summary, we have performed In L_3 -edge XANES study of indium oxynitride prepared by rf magnetron sputtering with different oxygen contents. The independent first principles XANES calculations of bulk InN and In_2O_3 give unambiguous agreement with the spectra from the samples prepared by using only N_2 and O_2 gas, respectively. Our results suggest that as much as 40% of oxygen can replace N in fourfold InN structure. The spectra from the samples with

higher O contents show that the alloy contains both fourfold and sixfold indium atoms. This implies that either the samples are phase separated or there exist a preferred intermediate crystal structure containing both fourfold and sixfold In atoms. Our calculations also show that the XANES features are not strongly affected by the substitution of N by O or vice versa.

This work is supported by Commission on Higher Education, Thailand (CHE-RES-RG "Theoretical Physics"), the Thailand Research Fund (BRG5180001 and PHD/0107/2548), and AOARD/AFOSR (FA4869-08-1-4007). Work at KMITL is supported by NANOTEC, Thailand (CoE Network). S.L. thanks MRSEC Program of the NSF (DMR05-20415), NSF IMI (DMR 04-09848), SSLDC, and CNSI for supports and hospitality during his visit at UCSCB, USA. We thank P. Songsiririthgul for useful discussions and W. Klysubun for facilitating x-ray measurements.

- ¹J. Wu, W. Walukiewicz, S. X. Li, R. Armitage, J. C. Ho, E. R. Weber, E. E. Haller, H. Lu, W. J. Schaff, A. Barez, and R. Jakiela, *Appl. Phys. Lett.* **84**, 2805 (2004).
- ²S.-H. Wei, X. Nie, I. G. Batyrev, and S. B. Zhang, *Phys. Rev. B* **67**, 165209 (2003).
- ³V. Yu. Davydov, A. A. Klochikhin, R. P. Seisyan, V. V. Emtsev, S. V. Ivanov, F. Bechstedt, J. Furthmüller, H. Harima, A. V. Mudryi, J. Aderhold, O. Semchinova, and J. Graul, *Phys. Status Solidi B* **229**, r1 (2002).
- ⁴J. Wu, W. Walukiewicz, K. M. Yu, J. W. Ager III, E. E. Haller, H. Lu, W. J. Schaff, Y. Saito, and Y. Nanishi, *Appl. Phys. Lett.* **80**, 3967 (2002).
- ⁵A. G. Bhuiyan, K. Sugita, K. Kasahima, A. Hashimoto, A. Yamamoto, and V. Y. Davydov, *Appl. Phys. Lett.* **83**, 4788 (2003).
- ⁶J. Wu, W. Walukiewicz, W. Shan, K. M. Yu, J. W. Ager, E. E. Haller, H. Lu, and W. J. Schaff, *Phys. Rev. B* **66**, 201403 (2002).
- ⁷V. Yu. Davydov, A. A. Klochikhin, V. V. Emtsev, S. V. Ivanov, V. V. Vekshin, F. Bechstedt, J. Furthmüller, H. Harima, A. V. Mudryi, A. Hashimoto, A. Yamamoto, J. Aderhold, J. Graul, and E. E. Haller, *Phys. Status Solidi B* **230**, r4 (2002).
- ⁸A. Klein, *Appl. Phys. Lett.* **77**, 2009 (2000).
- ⁹Motlan, E. M. Goldys, and T. L. Tansley, *J. Cryst. Growth* **241**, 165 (2002).
- ¹⁰M. Yoshimoto, H. Yamamoto, W. Huang, H. Harima, J. Saraie, A. Chayahara, and Y. Horino, *Appl. Phys. Lett.* **83**, 3480 (2003).
- ¹¹Y. Yi, S. Cho, Y. Roh, M. Noh, C.-N. Whang, K. Jeong, and H.-J. Shin, *Jpn. J. Appl. Phys., Part 1* **44**, 17 (2005).
- ¹²P. Fons, H. Tampo, A. V. Kolobov, M. Ohkubo, S. Niki, J. Tominaga, R. Carboni, F. Boscherini, and S. Friedrich, *Phys. Rev. Lett.* **96**, 045504 (2006).
- ¹³G. Ciatto, F. Boscherini, A. A. Bonapasta, F. Filippone, A. Polimeni, and M. Capizzi, *Phys. Rev. B* **71**, 201301 (2005).
- ¹⁴S. Limpjumnong, S. Rujirawat, A. Boonchun, M. F. Smith, and B. Cherdhirunkorn, *Appl. Phys. Lett.* **90**, 103113 (2007).
- ¹⁵N. Kietipaisalsophon, W. Bunjongpru, and J. Nukeaw, *Int. J. Mod. Phys. B* **16**, 4418 (2002).
- ¹⁶A. Sunthong, S. Porntheeraphat, A. Poyai, and J. Nukeaw, "An extreme change in structural and optical properties of indium oxynitride deposited by reactive gas-timing RF magnetron sputtering," *Appl. Surf. Sci.*
- ¹⁷G. Kresse and J. Furthmüller, *Comput. Mater. Sci.* **6**, 15 (1996).
- ¹⁸A. L. Ankudinov, C. E. Bouldin, J. J. Rehr, J. Sims, and H. Hung, *Phys. Rev. B* **65**, 104107 (2002).
- ¹⁹A. L. Ankudinov, B. Ravel, J. J. Rehr, and S. D. Conradson, *Phys. Rev. B* **58**, 7565 (1998).
- ²⁰We calculated a supercell of InN with one N replaced by an O atom. The calculated XANES of In atom next to this O is almost indistinguishable from that of pure InN. Further test shows that even all four N neighbors are replaced by O atoms, the spectrum is still remarkably similar to the pure InN. Similarly, a replacement of one O by a N in In_2O_3 supercell gives ignorable change in the spectrum compared to pure In_2O_3 . These tests clearly show that although the XANES features are sensitive to the structural arrangements of the neighbors of the In atom (fourfold or sixfold), they are not very sensitive to the interchanging of the anions.

Abstract submitted for the 33rd Congress on Science and Technology of Thailand,
Bangkok (2007)

การตรวจสอบโครงสร้างของคลอไรด์และโพแทสเซียมไอออนที่อยู่ในน้ำโดยเทคนิคการดูดกลืนแสงเอ็กซ์เรย์
จากแหล่งกำเนิดแสงซินโครตรอน

**VERIFICATION OF DYNAMIC HYDRATION-STRUCTURES OF Cl⁻ AND K⁺ BY
SYNCHROTRON X-RAY ABSORPTION NEAR-EDGE STRUCTURES**

จิรโรจน์ ต.เทียนประเสริฐ และ สุทธิ ลิ้มปิ๋จันจงค์

Jiraroj T-Thienprasert and Sukit Limpijumngong

School of Physics, Suranaree University of Technology and National Synchrotron Research
Center, Nakhon Ratchasima 30000, Thailand

บทคัดย่อ: โครงสร้างแบบไดนามิกของคลอไรด์และโพแทสเซียมไอออนในน้ำสามารถคำนวณได้จาก
ระเบียบวิธีการคำนวณของ ab initio QM/MM ซึ่งโครงสร้างเหล่านี้สามารถพิสูจน์ได้โดยการวัดการ
ดูดกลืนแสงเอ็กซ์เรย์แบบใกล้ขอบ (XANES) จากแหล่งกำเนิดแสงซินโครตรอน ดังนั้นเราจึงเลือก
โครงสร้างที่คำนวณได้มา 14 เฟรม โดยที่แต่ละเฟรมมีระยะห่างกัน 1 ps เพื่อนำมาคำนวณหา XANES
สเปกตรัมโดยใช้วิธีการคำนวณแบบเฟอร์ส-ปรินซิเปิล ซึ่งสเปกตรัมที่คำนวณได้ในแต่ละเฟรมมีลักษณะ
แตกต่างกันแต่แสดงให้เห็นว่าลักษณะการเรียงตัวของน้ำที่ต่างกันมีผลกับ XANES สเปกตรัมที่คำนวณได้
เพื่อพิสูจน์โครงสร้างที่ได้จากการคำนวณ จึงทำการวัด K-edge XANES สเปกตรัมของผลึกโพแทสเซียม
คลอไรด์ที่ละลายในน้ำที่ระบบลำแสงที่ 8 ของศูนย์ปฏิบัติการวิจัยเครื่องกำเนิดแสงซินโครตรอน
แห่งชาติ พบว่าค่าเฉลี่ยของ XANES สเปกตรัมที่คำนวณได้กับผลการทดลองมีลักษณะที่เหมือนกันอย่าง
มาก ซึ่งชี้ให้เห็นว่าเทคนิคการวัด XANES สามารถตรวจวัดโครงสร้างของน้ำได้และโครงสร้างที่คำนวณ
ได้มีความถูกต้อง

Abstract: The dynamic hydration-structures of Cl⁻ and K⁺, that were simulated by the
combined ab initio QM/MM approach [1], have been verified by synchrotron x-ray
absorption near-edge structure (XANES) experiments. Fourteen snapshots of the hydration
structures, with 1 ps interval, from the QM/MM dynamic simulations were picked to generate
the theoretical XANES using first principles approach [2]. The spectrum generated from
each frame shows distinct characteristics, indicating that XANES was very sensitive to the
detail of the hydration structures. To verify that the simulated dynamic hydration structures
were correct, the measurements of K and Cl K-edge XANES of aqueous KCl were performed
at beam line No. 8 of Siam photon laboratory, National Synchrotron Research Center. The
average theoretical XANES of Cl⁻ and K⁺ are in good agreement with the corresponding
measurements. The fact that the average theoretical XANES (but not individual spectrum
from each snapshot) agrees well with the measurement, is a strong indication that XANES
technique has a strong sensitivity to probe the hydration structures and the overall simulated
dynamic of hydration structures is realistic.

Keyword: X-ray Absorption Spectroscopy, ab initio, hydration structure

References:

1. A. Tongraar and B.M. Rode, *Phys. Chem. Chem. Phys.* **5**, 357 (2003).
2. S. Limpijumngong, M.F. Smith, and S.B. Zhang, *Appl. Phys. Lett.* **89**, 222113 (2006).

Abstract submitted for the 33rd Congress on Science and Technology of Thailand,
Bangkok (2007)

การคำนวณสเปกตรัมการดูดกลืนแสงอินฟราเรดและสเปกตรัมรามานของผลึกไททาเนียมไดออกไซด์ด้วย
วิธีเฟิร์ส-พริ้นซิเปิล

INFRARED ABSORPTION AND RAMAN SPECTRA OF TiO₂ BY FIRST PRINCIPLES CALCULATIONS

จิราจน์ ต.เทียนประเสริฐ และ สุกิจ ลิมปิจันนงศ์

Jiraroj T-Thienprasert and Sukit Limpijumnong

School of Physics, Suranaree University of Technology and National Synchrotron Research Center, Nakhon Ratchasima 30000, Thailand

บทคัดย่อ: โหมดการสั่นของผลึกไททาเนียมไดออกไซด์ที่มีโครงสร้างแบบอะนาตาสและรูไทล์ได้ถูกคำนวณโดยวิธีเฟิร์สพริ้นซิเปิลบนพื้นฐานของแรงคืนกลับที่คำนวณโดยการคำนวณแบบเฟิร์ส-พริ้นซิเปิล ซึ่งความถี่ที่คำนวณได้ประกอบด้วยโหมดของการดูดกลืนอินฟราเรดและรามาน การคำนวณโพลาไรเซชันของประจุที่สอดคล้องกับโหมดการสั่นต่าง ๆ จะทำให้ทราบถึงการดูดกลืนแสงอินฟราเรดหรือสเปกตรัมรามาน นั่นคือโหมดการสั่นที่ดูดกลืนแสงอินฟราเรดคือโหมดที่มีโพลาไรเซชันมาก และโหมดการสั่นที่วัดได้โดยรามานคือโหมดที่ไม่มีโพลาไรเซชัน

Abstract: Vibrational modes of anatase and rutile titanium dioxide (TiO₂) were calculated using the so-called “frozen phonon” approach based on the restoring forces obtained from first principles density functional theory. The obtained vibrational frequencies consist of both the IR and Raman modes. To distinguish the IR/Raman active modes from the rest, we calculated the charge polarization of each vibrational mode. The IR active modes are the modes with high charge polarization whereas the Raman active modes are the modes with null polarization.

Introduction: Titanium dioxide exists in the three crystal forms: anatase (tetragonal), rutile (tetragonal) and brookite (orthorhombic). While anatase and rutile TiO₂ have been extensively studied and used in many aspects, brookite TiO₂ is scarce and difficult to purify. Here, we choose to study only the anatase and rutile phases. The structure of anatase and rutile are illustrated in figure 1.

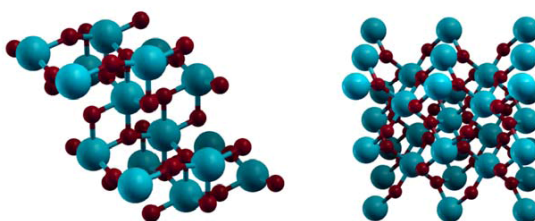


Figure 1 Crystal structures of anatase (left) and rutile (right) TiO₂. Large spheres: Ti, small spheres: O.

Abstract submitted for the 33rd Congress on Science and Technology of Thailand,
Bangkok (2007)

Methodology: First-principles pseudopotential [1, 2] methods based on density functional theory, as implemented in the Vienna ab initio simulation package (VASP) code [3, 4, 5] are used to calculate the total ground-state energies and the forces on all atom of TiO₂ supercells (48 atoms for rutile and anatase TiO₂). Initially, all atoms in the supercell are allowed to relax until the residue forces on all atom are less than 0.0001 eV/Å. Then, the frozen-phonon approach [6] is used to construct the dynamical matrix of which the vibrational modes are resulted after diagonalization. The intensities of the infrared-active modes can be determined from the corresponding oscillator strengths [7]:

$$f(\nu) = \sum_{\alpha} \left| \sum_{i\beta} Z_{\alpha\beta}^*(i) e_{\beta}(s|\nu) \right|^2, \quad (1)$$

where $e_{\beta}(s|\nu)$ is the normalized vibrational eigenvector of the ν th mode, α and β indicate Cartesian polarizations, i labels the atoms in the system, and $Z_{\alpha\beta}^*(i)$ is the effective-charge tensor of the i th atom explicitly calculated from first principles calculations. The high oscillator strength modes are the modes that are IR active and would result in the peaks in the IR absorption spectroscopy. On the other hand, the peaks in the Raman spectra correspond to the modes with zero oscillator strength. The results from our calculation of oscillator strength (Eq. 1) thus allow us to identify the IR absorption and Raman frequencies.

Results, Discussion and Conclusion: The calculated vibrational frequencies of the modes that are IR and Raman active are compared with the experimental results [8, 9]. The calculated results are in reasonably good agreement with the IR and Raman measurements, i.e. averagely within 5 %. As a future plan, we will calculate the vibration modes associated with Ce impurity in various configurations in TiO₂. In conjunction with experimental Raman measurements, we hope to positively identify the site occupation of Ce.

References:

1. D. Vanderbilt; *Soft self-consistent pseudopotentials in a generalized eigenvalue formalism*, Phys. Rev. B **41**, R7892 (1990).
2. G. Kresse and J. Hafner; *Norm-conserving and ultrasoft pseudopotentials for first-row and transition-elements*, J. Phys.: Condens. Matter **6**, 8245 (1994).
3. G. Kresse and J. Hafner; *Ab initio molecular dynamics for liquid metals*, Phys. Rev. B **47**, 558 (1993).
4. G. Kresse and J. Furthmuller; *Efficient iterative schemes for ab initio total-energy calculations using a plane-wave basis set*, Phys. Rev. B **54**, 11169 (1996).
5. W. Kohn and L. Sham; *Self-Consistent Equations including exchange and correlation effects*, Phys. Rev. **140**, A1133 (1965).
6. A. M. Teweldeberhan and S. Fahy; *Calculated pressure dependence of the localized vibrational mode of nitrogen in GaN_xAs_{1-x}*, Phys. Rev. B **72**, 195203 (2005).
7. P. Giannozzi and S. Baroni; *Vibrational and dielectric properties of C₆₀ from density-functional perturbation theory*, J. Chem. Phys. **100**, 8537 (1994).
8. M. Ocana, J. V. Garcia-Ramos, and C. J. Serna; *Low-Temperature Nucleation of Rutile Observed by Raman Spectroscopy during Crystallization of TiO₂*, J. Am. Ceram. Soc. **75**, 2010 (1992).
9. R. J. Gonzalez and R. Zallen; *Infrared reflectivity and lattice fundamentals in anatase TiO₂*, Phys. Rev. B **55**, 7014 (1997).

Abstract submitted for the Siam Physics Congress 2009, Phetchburi (2009)

SPC2009
CHA-AM, PHETCHBURI, THAILAND

Oral Presentation

X-ray absorption spectroscopy of indium nitride, indium oxide, and their alloys

J. T-Thienprasert^{1*}, J. Nukeaw², A. Sungthong², S. Porntheeraphat³, D. Onkaw¹, S. Rujirawat¹, and S. Limpijumnong¹

¹School of Physics, Suranaree University of Technology and Synchrotron Light Research Institute, Nakhon Ratchasima 30000, Thailand

²Nanotechnology Research Center of KMITL and Department of Applied Physics, King Mong's Institute of Technology Ladkrabang, Bangkok 10520, Thailand

³Thai Microelectronics Center, National Electronics and Computer Technology Center, Pathumthani 12120, Thailand

⁴Fast Neutron Research Facility, Faculty of Science, Chiang Mai University, Chiang Mai 50200, Thailand

Abstract

Indium oxynitride films with different O and N fractions are prepared by rf magnetron sputtering. The preparing conditions are ranging from no O₂ gas (intended to prepare pure InN) to no N₂ gas (intended to prepare pure In₂O₃). The samples are characterized by synchrotron x-ray absorption near-edge structure (XANES) measurements of In L₃ edge in conjunction with first-principles calculations. Based on independently calculated XANES spectra, we found that the XANES spectra of this alloy are sensitive to the coordination number of In atoms, i.e., fourfold for indium nitride-like structures and sixfold for indium oxide-like structures, but not to the substitution of nearest neighbor N by O or vice versa. Based on this assumption, the simulated XANES spectra are in good agreement with the measured results and the information on alloys' local structures is revealed.

Keywords:

X-ray absorption near-edge structure, first-principles, indium oxynitride

* Corresponding author. Email: chorawut@hotmail.com

Abstract submitted for the Siam Physics Congress 2008, Nakhon Ratchasima (2008)

SPC2008
NAKHON RATCHASIMA, THAILAND

Determination of oxygen defect structures in CdTe from their infrared signatures

***J. T-Thienprasert,¹ S. B. Zhang,² A. Janotti,³ C.G. Van de Walle,³
and S. Limpijumnong¹***

¹ School of Physics, Suranaree University of Technology, and National Synchrotron Research Center, Nakhon Ratchasima 30000, Thailand.

² Department of Physics, Applied Physics, and Astronomy, Rensselaer Polytechnic Institute, Troy, New York 12180.

³ Materials Department, University of California, Santa Barbara, California 93106-5050.

Abstract

Recently, the localized vibrational modes (LVM) related to oxygen impurities in CdTe have been experimentally observed using ultrahigh resolution Fourier transform infrared (FTIR) spectrometry [G. Chen, et al., Phys. Rev. Lett. 96, 035508 (2006)]. At low temperature a low-frequency LVM was found at 350 cm^{-1} as well as two high frequency LVMs at 1097 and 1108 cm^{-1} ; the latter merge into one at room temperature. Chen et al. proposed that the low frequency mode is associated with an oxygen substitution on the Te site (O_{Te}) and the high frequency modes are associated with a complex of O_{Te} and Cd vacancy ($\text{O}_{\text{Te}}\text{-V}_{\text{Cd}}$). Based on first-principles calculations and a frozen phonon approach, we calculated the LVMs of O_{Te} , $\text{O}_{\text{Te}}\text{-V}_{\text{Cd}}$ and some other configurations of O-related defects. While the calculated O_{Te} LVM of 338 cm^{-1} agrees very well with the measured value (well within the computational error bar), the calculated $\text{O}_{\text{Te}}\text{-V}_{\text{Cd}}$ LVMs of 112 and 472 cm^{-1} are totally inconsistent with the high frequency values as proposed by Chen et al. . This strongly suggests that the observed high frequency modes arise from other defects. Our further calculations suggest that oxygen-related defects in the form of O_2 , such as $(\text{O}_2)_{\text{Te}}$, are more plausible candidates.

Keyword: Localized vibrational mode (LVM), first-principles calculation

CURRICULUM VITAE

Mr. Jiraroj T-Thienprasert was born on May 25, 1980 in Bangkok province. He is a physicist, sportsman, and musician. He was a badminton player while he was studying at high school. Moreover, he can play several musical instruments such as clarinet, acoustic guitar, electric guitar (most favorite), bass, and drum. He received Bachelor (second-class honor) and Master degree of science in physics from Kasetsart University in 2002 and 2005, respectively. After he graduated in Bachelor, he was a lecturer at Kasetsart University. In 2005, he was granted the scholarship from the Thailand Research Fund under the Royal Golden Jubilee Program to pursue a Ph.D. degree in the school of Physics, Suranaree University of Technology under the supervision of Prof. Dr. Sukit Limpijumnong. While he was studying a Ph.D. degree, he built three high performance computer clusters at Synchrotron Light Research Institute, school of Chemistry (Suranaree University of Technology), and department of Physics (Kasetsart University). He interested in condense matter physics using first-principles calculation.